

# Corrosion-induced Hydrogen Embrittlement in High-Strength Al-Alloys

THESIS

Submitted in partial fulfillment of the requirements for the degree of  
Doctor of Philosophy in Mechanical Engineering  
of the Department of Mechanical and Industrial Engineering  
University of Thessaly

By

**Helen Kamoutsi**  
Dipl. Mechanical Engineer,  
University of Thessaly

Supervisors:

Prof. G.N. Haidemenopoulos  
Prof. V. Bontozoglou

Volos, 9 April, 2004

ND = 14.311  
KOE 14.180

Phd Thesis Uth/MIE No. (13)

# Corrosion-induced Hydrogen Embrittlement in High-Strength Al-Alloys



THESIS

Submitted in partial fulfillment of the requirements for the degree of  
Doctor of Philosophy in Mechanical Engineering  
of the Department of Mechanical and Industrial Engineering  
University of Thessaly

By

**Helen Kamoutsi**  
Dipl. Mechanical Engineer,  
University of Thessaly

Supervisors:

Prof. G.N. Haidemenopoulos  
Prof. V. Bontozoglou

Volos, 9 April, 2004

**“Corrosion induced Hydrogen Embrittlement in High  
Strength Al-Alloys”**

# “Corrosion induced Hydrogen Embrittlement in High Strength Al-Alloys”

## Summary

Corrosion presents a major concern to the structural integrity of aging aircraft structures. As the time of an aircraft structure in service increases, there is a growing probability that corrosion will interact with other forms of damage, such as single fatigue cracks or multiple-site damage in the form of widespread cracking at regions of high-stress gradients; it can result in loss of structural integrity and may lead to fatal consequences. Thus, the effect of corrosion on the damage tolerance ability of advanced aluminum alloys calls for a very diligent consideration of the problems associated with the combined effect of corrosion and embrittling mechanisms. The present thesis focuses on the observed corrosion-induced embrittlement of 2024 alloy and tries to answer the key question on whether the observed embrittlement is attributed to hydrogen uptake and trapping in the material. Limited work has also been performed on alloy 6013.

The experimental procedures involved the following actions: (1) accelerated corrosion testing (using the EXCO procedure), (2) detailed microstructural investigation of the evolution of corrosion damage by employing AFM, stereo-microscopy, SEM and metallography, (3) hydrogen measurements by employing an in-house thermal desorption – gas chromatography system, (4) detailed fractographic analysis of tensile specimens.

The major results reached are the following:

Corrosion damage in the alloy starts with pitting and develops to a network of intergranular corrosion leading to exfoliation of material. Pit-to-pit interaction and pit clustering are mechanisms aiding the development of corrosion damage. The depth of attack increases with exposure time. Typical value for depth of attack is  $350\mu\text{m}$  for 24h of exposure time.

Hydrogen is produced during the corrosion process and is being trapped in distinct energy states, which correspond to different microstructural traps. These traps are activated and liberate hydrogen at different temperatures. In alloy 2024, four traps T1 to T4 were identified. Trap T1 is considered to be a reversible trap, which liberates hydrogen continuously at low temperatures. Traps T2, T3 and T4 saturate with exposure time and are considered to be irreversible.

Trapping state T1 corresponds to hydrogen at interstitial sites. The observed material softening at the same temperature range of T1 activation correlates with theories of hydrogen-induced softening stemming from dislocation-hydrogen interactions. Trapping state T4 is the strongest trap and its temperature range corresponds to the dissolution of the strengthening precipitate in alloy 2024.

The hydrogen front advances with the corrosion front, so hydrogen penetrates deep in the material through the intergranular paths generated by the corrosion process. Then hydrogen diffuses further in the material establishing a hydrogen affected zone beneath the corrosion depth of attack.

Removal of the corrosion layer (equal to the depth of attack) leads to complete restoration of yield strength and partial restoration of ductility. Removal of the corrosion layer and heating above the T4 activation range (to activate all traps) leads not only to complete restoration of strength but also to complete restoration of ductility.

Detailed fractographic analysis showed the existence of a quasicleavage transition zone between the intergranular corrosion zone and the ductile corrosion-unaffected material. This quasicleavage zone has been embrittled by hydrogen diffusion and trapping. Removal of hydrogen by heating restores all ductility. These results constitute evidence of hydrogen embrittlement in Al-alloy 2024.

Additional effects studied included the effect of side surface, cladding and anodizing. Results indicated that more hydrogen enters the material from the LS side (side surface) than the LT side (rolling plane), probably due to the higher density of grain boundaries in the LS side. Both forms of corrosion protection, cladding and anodizing reduced considerably hydrogen uptake and trapping.

Regarding the behavior of alloy 6013, preliminary work indicated that the evolution of corrosion damage follows a similar pattern as for alloy 2024. However corrosion in 6013 is more intense and intergranular corrosion and exfoliation appear in shorter exposure times. Hydrogen is also produced during corrosion and is being trapped in the alloy at distinct energy states.

Today's aircraft design and maintenance follows the damage tolerance philosophy. According to this practice among others, flaws or cracks are allowed in the structure once they are tolerated by the material. Tolerance depends on the fracture toughness of the alloy. The cracks grow by fatigue. The life of the structure depends (i) on the prescribed damage tolerance and (ii) on the fatigue crack growth rate. Both of these factors are influenced by corrosion and hydrogen embrittlement. The present thesis sheds light at the degradation of ductility and hence fracture toughness, due to the corrosion-induced hydrogen embrittlement, which reduces the damage tolerance of the structure. These arguments are particularly important for the so-called "aged aircraft", which has exceeded or is near the operational lifetime, but it is still operated by the airlines. These aircrafts have accumulated damage and corrosion. The damage tolerance of the material has decreased due to hydrogen embrittlement, at least locally in critical areas such as rivet holes. These conditions call for a re-determination of residual strength, if the decision is to extend the operational lifetime of such aircrafts.

## «Διάβρωση και Ψαθυροποίηση Υδρογόνου σε κράματα Αλουμινίου Υψηλής Αντοχής»

# Εκτεταμένη Περίληψη

Η διάβρωση αποτελεί ένα σημαντικό πρόβλημα για την δομική ακεραιότητα των ‘γηρασμένων’ αεροπορικών κατασκευών. Με την πάροδο του χρόνου λειτουργίας της κατασκευής, υπάρχει αυξημένη πιθανότητα αλληλεπίδρασης της διάβρωσης με άλλους μηχανισμούς βλάβης, όπως μεμονωμένες ή και πολλαπλές ρωγμές κόπωσης. Η κατάσταση αυτή μπορεί εύκολα να οδηγήσει σε απώλεια της δομικής ακεραιότητας. Η επίδραση της διάβρωσης στην ανοχή μιας κατασκευής στην βλάβη απαιτεί την μελέτη του συνδυασμού διάβρωσης και μηχανισμών ψαθυροποίησης. Η παρούσα εργασία εστιάζει στην παρατηρούμενη ψαθυροποίηση που συνοδεύει την διάβρωση του κράματος 2024 και προσπαθεί να απαντήσει στο ερώτημα κατά πόσο η ψαθυροποίηση αυτή μπορεί να αποδοθεί στην παγίδευση υδρογόνου στο μέταλλο και να κατανοήσει τον μηχανισμό λειτουργίας και αλληλεπίδρασης τους.

Οι πειραματικές διαδικασίες στο κράμα 2024 συμπεριέλαβαν τα εξής:

- (α) δοκιμές επιταχυνόμενης διάβρωσης EXCO (χρησιμοποιείται από τις εταιρίες κατασκευής αεροσκαφών),
- (β) λεπτομερή ανάλυση μικροδομής με τη χρήση στερεοσκοπίου, μεταλλογραφικού μικροσκοπίου, SEM και AFM,
- (γ) μετρήσεις υδρογόνου με την χρήση τεχνικής θερμικής εκρόφησης-αέριας χρωματογραφίας και
- (δ) λεπτομερείς θραυστογραφικές αναλύσεις δοκιμίων εφελκυσμού.

Τα κυριότερα αποτελέσματα της εργασίας είναι τα εξής:

Η διάβρωση EXCO στο κράμα 2024 ξεκινά ως τρηματική διάβρωση (Fig. 4. 8 έως Fig. 4. 10) και εξελίσσεται με την ανάπτυξη ενός δικτύου περικρυσταλλικής διάβρωσης (Fig. 4. 11, Fig. 4. 12), η οποία οδηγεί σε αποφλοιώση του υλικού (Fig. 4. 16 -Fig. 4. 22). Η αλληλεπίδραση και η συσσώρευση τρημάτων υποβοηθούν την εξέλιξη της διαβρωτικής δράσης. Το βάθος προσβολής αυξάνεται με τον χρόνο έκθεσης στο διαβρωτικό μέσον (Fig. 4. 16 -Fig. 4. 22). Τυπική τιμή είναι 350μm μετά από 24h έκθεσης (Fig. 4. 28, Fig. 4. 29).

Το υδρογόνο παράγεται κατά τη διάρκεια της διαβρωτικής δράσης και δεσμεύεται σε συγκεκριμένες ενεργειακές καταστάσεις, οι οποίες αντιστοιχούν σε συγκεκριμένες ‘παγίδες’ της μικροδομής (Fig. 4. 23). Οι παγίδες αυτές ενεργοποιούνται και αποδεσμεύουν υδρογόνο σε διαφορετικές θερμοκρασίες (Fig. 4. 25). Στο 2024 εντοπίστηκαν τέσσερις παγίδες δέσμευσης υδρογόνου (T1 έως T4). Όσο πιο υψηλή είναι η θερμοκρασία αποδέσμευσης τόσο πιο ισχυρή είναι η παγίδα. Οι παγίδες καταχωρούνται σε αντιστρεπτές (T1), οι οποίες απελευθερώνουν υδρογόνο συνεχώς και μη αντιστρεπτές (T3, T2 και T4), οι οποίες απελευθερώνουν υδρογόνο μόνο όταν φτάσουν την θερμοκρασία που τις προσδιορίζει.

Μετρήσεις μικροσκληρότητας που εκτελέστηκαν μετά την υποβολή του υλικού στο ίδιο θερμικό κύκλο, που χρησιμοποιήθηκε για τις μετρήσεις υδρογόνου έδειξαν πως το διαβρωμένο υλικό γίνεται πιο μαλακό, γεγονός το οποίο συμφωνεί με τις θεωρίες για εξασθένηση (softening) από την είσοδο υδρογόνου λόγω αλληλεπίδρασης του με τις γραμμοαταξίες. Η αποβολή υδρογόνου από την παγίδα υψηλής θερμοκρασίας T4 συμπίπτει με την θερμοκρασία διαλυτοποίησης της φάσης ισχυροποίησης, υποδεικνύοντας ότι το υδρογόνο είναι δεσμευμένο στην φάση αυτή.

Το μέτωπο του υδρογόνου κινείται με το μέτωπο της διάβρωσης και το υδρογόνο διεισδύει βαθιά στο υλικό μέσω των περικρυσταλλικών 'διαδρόμων', που δημιουργούνται από την διαβρωτική δράση. Στη συνέχεια το υδρογόνο διαχέεται μέσα στο υλικό σχηματίζοντας μία ζώνη διάχυσης κάτω από το βάθος προσβολής της διάβρωσης.

Η απομάκρυνση του διαβρωμένου στρώματος (ίσου με το βάθος προσβολής) (Fig. 4. 26) οδηγεί σε πλήρη ανάκτηση της αντοχής αλλά σε μερική μόνον ανάκτηση της ολκιμότητας του κράματος (66% του δοκιμίου αναφοράς). Αντίστοιχα, η απομάκρυνση του διαβρωμένου στρώματος και θέρμανση του υλικού πάνω από την κρίσιμη θερμοκρασία ενεργοποίησης της ισχυρότερης παγίδας υδρογόνου (450°C, T<sub>4</sub>), ώστε να ενεργοποιηθεί το σύνολο των παγίδων, οδηγεί όχι μόνο σε ανάκτηση της αντοχής αλλά και σε πλήρη ανάκτηση της ολκιμότητας του κράματος - σχεδόν 99% του δοκιμίου αναφοράς - (Fig. 4. 32).

Η λεπτομερής θραυστογραφική ανάλυση έδειξε την παρουσία ψαθυροποιημένης ζώνης με χαρακτηριστικά *quasicleavage*, κάτω από την περικρυσταλλική επιφάνεια θραύσης της διαβρωμένης περιοχής. Η περιοχή αυτή συμπίπτει με την ζώνη διάχυσης υδρογόνου που αναφέρθηκε παραπάνω (Fig. 4. 33 έως Fig. 4. 36). Η θέρμανση του υλικού προκάλεσε την εκρόφιση του υδρογόνου από την ζώνη αυτή και οδήγησε στην ανάκτηση της ολκιμότητας (Fig. 4. 37 έως Fig. 4. 40). Τα αποτελέσματα αυτά αποτελούν απόδειξη ψαθυροποίησης υδρογόνου στο κράμα 2024.

Επιπρόσθετα αποτελέσματα αφορούν την επίδραση της παράπλευρης επιφάνειας (Fig. 4. 41), του *cladding* (Fig. 4. 45), και της ανοδίσωσης (Fig. 4. 47). Τα αποτελέσματα έδειξαν ότι περισσότερο υδρογόνο εισάγεται από την παράπλευρη επιφάνεια απ' ό,τι από την επιφάνεια έλασης, πιθανόν λόγω της μεγαλύτερης πυκνότητας συνόρων των κόκκων στην παράπλευρη επιφάνεια. Το *cladding* και η ανοδίσωση, εκτός από την διαβρωτική προστασία, επέφεραν και σημαντική μείωση στις ποσότητες υδρογόνου που δεσμεύονται κατά την διάβρωση του κράματος.

Κατά την διάρκεια της παρούσης διατριβής επιπρόσθετα στο κράμα 2024, ξεκίνησε και μια προκαταρκτική μελέτη του κράματος 6013, κυρίως σε σχέση με την συμπεριφορά του στην διάβρωση και την απορρόφηση υδρογόνου. Κύριος στόχος η εξακρίβωση του κατά πόσο το 6013 συμπεριφέρεται κατά την διάβρωση όπως το 2024 π.χ. απορρόφηση και δέσμευση υδρογόνου.

Δοκίμια του κράματος υποβλήθηκαν στην ίδια πειραματική διαδικασία με το 2024 (όπως αυτή περιγράφεται παραπάνω). Σε σύγκριση με το κράμα 2024 το 6013 παρουσίασε παρόμοια συμπεριφορά στην διάβρωση, η οποία ξεκινά με τμηματική διάβρωση και εξελίσσεται με την ανάπτυξη ενός δικτύου περικρυσταλλικής διάβρωσης (Fig. 4. 49 έως Fig. 4. 51), η οποία οδηγεί σε αποφλοίωση του υλικού. Το βάθος διείσδυσης αυξάνεται με τον χρόνο έκθεσης αλλά ο ρυθμός αφαίρεσης υλικού είναι πολύ μεγαλύτερος απ' ό,τι στο κράμα 2024.

Μετρήσεις υδρογόνου έδειξαν ότι και το 6013 δεσμεύει υδρογόνο με την διάβρωση και το απελευθερώνει σε διαφορετικές θερμοκρασίες (η ταυτότητα των οποίων δεν μελετήθηκε). Σε σχέση με 2024 παρουσιάζει μεγαλύτερο ρυθμό συσσώρευσης υδρογόνου ως προς τον χρόνο προσβολής, αλλά για χρόνους μεγαλύτερους των 24 ωρών ο ρυθμός μειώνεται και σταθεροποιείται (Fig. 4. 53). Το βάθος διείσδυσης μετρήθηκε στα 250μm για 4 ώρες διάβρωση.

Η παρούσα εργασία υποδεικνύει ότι η ανοχή στη βλάβη μιας κατασκευής, και κατ' επέκταση η δομική ακεραιότητα, είναι δυνατόν να υποβαθμιστούν σημαντικά λόγω ψαθυροποίησης υδρογόνου, που προκαλείται από την διάβρωση του υλικού. Το θέμα αυτό είναι ιδιαίτερα σημαντικό για τις 'γηρασμένες' κατασκευές, αυτές δηλαδή που ολοκλήρωσαν τον προβλεπόμενο χρόνο λειτουργίας και έχουν συσσωρεύει διάβρωση και μικρορωγμές. Στις περιπτώσεις αυτές πρέπει να λαμβάνεται υπόψη η πιθανή τοπική μείωση της ανοχής στη βλάβη λόγω υδρογόνου (σε περιοχές όπως οι οπές) για τον προσδιορισμό της απομένουσας

αντοχής και διάρκειας ζωής της κατασκευής. Αυτή η κατάσταση παρουσιάζεται στις Fig. 4. 55 και Fig. 4. 56. Η κρίσιμη κατάσταση θα εμφανιστεί εάν η διάδοση της ρωγμής μεταβεί στην επηρεασμένη από το υδρογόνο περιοχή όπου τοπικά η ανοχή σε βλάβη “damage tolerance” έχει μειωθεί. Αυτές οι καταστάσεις απαιτούν έναν επαναπροσδιορισμό της διάρκειας ζωής εάν σκοπός είναι η επέκταση της λειτουργικής απομένουσας αντοχής του αεροσκάφους.



# Table of Contents

Summary.....	3
Εκτεταμένη Περίληψη.....	5
Table of Contents .....	8
List of Tables.....	9
List of Figures.....	10
Acknowledgments .....	14
Ευχαριστίες.....	15
Chapter 1 - Introduction .....	17
Chapter 2 - Bibliographic Review.....	21
2.1 The aircraft aluminium alloys of the 2xxx and 6xxx series .....	21
2.2 The corrosion of high-strength aluminium alloys .....	25
2.3 Hydrogen Damage in Alloys.....	29
Chapter 3 - Experimental procedures.....	37
3.1 Materials Studied.....	37
3.2 Accelerated corrosion testing .....	38
3.3 Microstructural characterization of corrosion .....	38
3.4 Hydrogen measurements .....	41
3.5 Microhardness testing.....	42
Chapter 4 – Corrosion and hydrogen embrittlement.....	44
4.1 Microstructural Characterization of Corrosion .....	44
4.2 Hydrogen penetration in 2024.....	44
4.3 Microhardness measurements .....	44
4.4 Fractography of tensile specimens .....	44
4.5 Additional effects in hydrogen uptake .....	44
4.6 Corrosion and Hydrogen uptake of aluminium alloy 6013.....	44
Chapter 5 – Concluding Discussion .....	44
Chapter 6 – Conclusions.....	44
Chapter 8 – Proposed Future Work.....	44
Chapter 7 – References.....	44
Curriculum Vitae .....	44

# List of Tables

Table 1: Wrought Alloy Designation System and Characteristics.....	21
Table 2: The precipitation sequence of 2xxx and 6xxx alloys [34]. .....	23
Table 3: Classification of hydrogen traps in steels [73]. .....	33
Table 4: Thickness of aluminum alloys (Bare: only natural oxide, Alclad: alloy 1230). .....	37
Table 5: Chemical composition of alloys of aluminum (%wt.). .....	37
Table 6: Thermal treatments of aluminum alloys.....	38
Table 7: Summary of AFM observations on the early stages of EXCO corrosion. ....	44
Table 8: Results of tensile tests [97].....	44
Table 9: Tensile properties as %value of reference specimen [97].....	44

# List of Figures

Fig. 3. 1: Labelling scheme used for directions and planes.....	38
Fig. 3. 2: Gas Chromatography experimental setup.....	43
Fig. 4. 1: Tree-dimensional depiction of alloy 2024-T3 microstructure (LS plane).....	44
Fig. 4. 2: Two-dimensional depiction of the microstructure of alloy 2024-T3 (LS plane) with line scans. ....	44
Fig. 4. 3: AFM topographies of as received aluminum alloy 2024 2.4mm LT plane. (a) Through (c). ....	44
Fig. 4. 4: AFM topographies for the as received aluminum alloy 2024 3mm, LT plane. (a) through (f). ....	44
Fig. 4. 5: Alloy 2024-T3 (LT plane), 15min in the corrosive solution exco (Characteristic rolling ridges). ....	44
Fig. 4. 6: Alloy 2024-T3 (LT plane), 15min in the corrosive solution EXCO.....	44
Fig. 4. 7: Alloy 2024-T3 (LT plane), 15min in the corrosive solution EXCO. Fragmentation and spaling of surface oxide.....	44
Fig. 4. 8: Alloy 2024-T3 (LT plane), 15min in the corrosive solution EXCO. 3D depiction of corrosion, Initiation of pitting (arrow C) corrosion (50x50 $\mu$ m).....	44
Fig. 4. 9: Alloy 2024-T3 (LT plane), 30min in the EXCO solution (a) and (b) different areas (130x130 $\mu$ m), (c) and (d) magnification of previous topographies (30x30 $\mu$ m). ....	44
Fig. 4. 10: Alloy 2024-T3 (LT plane), 1hour in the corrosive solution EXCO (a). Three-dimensional magnification of previous picture (b). (c) and (d) are line scans. ....	44
Fig. 4. 11: Alloy 2024-T3 (LT plane), for 2 hours in the corrosive solution EXCO (a), (b), (c) and (d).....	44
Fig. 4. 12: Alloy 2024-T3 (LT plane), for 4 hours in the corrosive solution EXCO. ....	44
Fig. 4. 13: Stereo photography of Alloy 2024 (LT plane), exposed in EXCO for 2 to 96 hours (details in the text). ....	44
Fig. 4. 14: SEM topographies of Alloy 2024 (LT plane), exposed in EXCO for 2 to 96 hours (details in the text). ....	44
Fig. 4. 15: SEM topographies of Alloy 2024 (LT plane) exhibiting pit-to-pit interactions and pit clustering after exposure in EXCO for the indicated times.....	44
Fig. 4. 16: Alloy 2024, 8 hours EXCO exposure. ....	44
Fig. 4. 17: Alloy 2024, 12 hours EXCO exposure. ....	44
Fig. 4. 18: Alloy 2024, 24 hours EXCO exposure ....	44
Fig. 4. 19: Alloy 2024, study of side surface 36 hours corrosion (x 50).....	44
Fig. 4. 20: Alloy 2024, 48 hours EXCO exposure. Spreading of corrosion beneath surface by intergranular corrosion.....	44
Fig. 4. 21: Alloy 2024, 72 hours EXCO exposure. Spreading of intergranular corrosion and exfoliation. ....	44
Fig. 4. 22: Alloy 2024, 96 hours EXCO exposure. Spreading of corrosion .Beneath the surface by intergranular corrosion leading to exfoliation.....	44
Fig. 4. 23: Desorption of H <sub>2</sub> in specimens of aluminium alloy 2024-T3 for continuous heating up to 600 °C. Thickness of material 1,8 mm. ....	44
Fig. 4. 24: Magnification of Previous Figure in the region up to 1.0 $\mu$ gH <sub>2</sub> /min. ....	44
Fig. 4. 25: Amount of hydrogen desorpted from the four trapping states (T1-T4) as a fuction of corrosion exposure time. ....	44
Fig. 4. 26: H <sub>2</sub> evolution as a function of temperature for specimens with varying removal depth. ....	44

Fig. 4. 27: Total amount of H <sub>2</sub> (μg) for different removal depths. 24h exposure to EXCO solution (2.4 mm). .....	44
Fig. 4. 28: Depth of Attack 2.4mm.....	44
Fig. 4. 29: Depth of Attack 3 mm.....	44
Fig. 4. 30: Hydrogen in Uncorroded Specimen of 3mm (b). .....	44
Fig. 4. 31: Microhardness profile versus temperature for alloy 2024. ....	44
Fig. 4. 32: The results of Table 8 represented as percentages of the respective reference values [97]. .....	44
Fig. 4. 33: Fracture surfaces of condition C (corroded 24h) specimen. Individual photos correspond to different modes of fracture from the specimen surface (on start of corrosion) through the centre of the specimen. ....	44
Fig. 4. 34: Fracture surfaces of condition C (corroded 24h) specimen, bottom surface. Individual photos correspond to different modes of fracture from the specimen surface (on start of corrosion) through the center of the specimen. ....	44
Fig. 4. 35: Fracture surfaces of condition CR (corroded 24h+removal of 350μm) specimen. Magnification of the embrittled region quasicleavage (a), transition to ductile fracture (b, c). ....	44
Fig. 4. 36: Fracture surfaces of condition CR (corroded 24h+removal of 350μm). Embrittled zone (a), the transition to ductile (Fig.15b) and the ductile region in the interior of the specimen (Fig.15c). ....	44
Fig. 4. 37: Fracture surfaces of condition CRH (a) (corroded 24h+removal of 350μm) and RH (b) specimen. Both exhibit ductile mode of fracture. ....	44
Fig. 4. 38: Fracture surfaces of condition CRH (a) and RH (b) surface zone of mixed intergranular/dimple nature. ....	44
Fig. 4. 39: Rounded features (a), grain boundaries (b).....	44
Fig. 4. 40: Fracture surfaces of condition CRH in LT direction intergranular character of the surface zone. ....	44
Fig. 4. 41: Specimen with similar total side area (0.34-0.14gr) but different weight (106 versus 116 mm <sup>2</sup> ) Results of hydrogen desorption versus temperature (a). Specimen with similar weight (0.13-0.14gr) but different total side area (106 versus 58mm <sup>2</sup> ) Results of hydrogen desorption versus temperature (b). ....	44
Fig. 4. 42: The results of hydrogen desorption versus the side surface.....	44
Fig. 4. 43: Comparative diagram with and without resin on the side surface. ....	44
Fig. 4. 44: Metallography of alloy 2024-T3 Bare with thickness of 1,8 mm. (a) Surface of rolling (LT plane). (b) Section vertical to the rolling direction of Fig. 4. 44 (a), (LS plane). ....	44
Fig. 4. 45: H <sub>2</sub> desorption spectra of 2024-T3 Al Clad specimens.....	44
Fig. 4. 46: Metallography of alloy 2024-T3 Al clad (side surface).....	44
Fig. 4. 47: Effect of anodizing in the side surface of specimen that have suffered corrosion for 24 hours. ....	44
Fig. 4. 48: AFM topographies for the as received aluminum alloy 6013, LT plane. (a) through (d). ....	44
Fig. 4. 49: Alloy 6013-T6 (LT plane), for different exposure times in the corrosive solution EXCO. Fragmentation and spaling of surface oxide. ....	44
Fig. 4. 50: Alloy 6013-T6 (LT plane), for different exposure times in the corrosive solution EXCO. Characteristic rolling marks at different exposure times. ....	44
Fig. 4. 51: Alloy 6013-T6 (LT plane), for different exposure times in the corrosive solution EXCO, pitting corrosion. ....	44

- Fig. 4. 52: (a) Hydrogen desorption spectra for specimen of alloy 6013 for exposure to exco 0 to 4 hours (b) Hydrogen desorption spectra for specimen of alloy 6013 for exposure to exco 4 to 18 hours. .... 44
- Fig. 4. 53: Hydrogen desorption spectra for specimen of alloy 6013 for exposure to exco 4 to 120 hours. .... 44
- Fig. 4. 54: H<sub>2</sub> evolution as a function of temperature for specimens with varying removal depth. .... 44
- Fig. 4. 55: Schematic representation of the corrosion layer and the hydrogen affected area beneath it. After removal of the corroded layer, a hydrogen affected zone (free of corrosion) remains and affects the mechanical properties of the material (elongation 66% of reference). Heating releases trapped hydrogen and restores elongation to 99% of reference. .... 44
- Fig. 4. 56: The situation around two adjacent rivet holes. The concentric circles around the hole represent the corroded area around the hole and the hydrogen affected zone. .... 44



*I dedicate my work to my parents*

*Stamatina Kamoutsi*

*and*

*Mantho Kamoutsi*

# Acknowledgments

Acknowledgments of assistance and support for completion of this dissertation seem endless. Writing a thesis is the final part of the PhD-project of one person. The work is, however, always carried out and supported by a large group of people. For this reason thanks a lot to everyone who contributed in any way to this thesis.

I must express gratitude to my supervisors, Professor Gregory N. Haidemenopoulos and Professor Vassili Bontozoglou for their assistance, persistence, and particularly for their patience in finishing this document. Without their sponsorship and knowledge, this dissertation would not be possible.

My deepest appreciation is also extended to Professor Spyros Pantelakis, from the University of Patras for providing the mechanical test results and for the stimulating collaboration through the course of the thesis. Special thanks are deserved by Dr. Alexis Kermanidis and Mr. Paraskeuas Petroyiannis, who readily provided their knowledge and assistance for matters concerning mechanical testing.

I would like to thank the remaining members of the examining committee Professors: G. Papadimitriou (N.T.U.A), B. Papazoglou (N.T.U.A), D. Tsipas (AUTH), P. Tsiakaras (UTH) for the interest they displayed for my work.

I would like to express my deepest gratitude to anyone who supported this thesis financially hence making this work possible. In particular:

- GSRT (General Secretarial for Research and Technology) for financial support through the PENED program.
- Airbus for providing alloys and financial support. Specifically Dr Tempus and Dr Zink for helpful discussion.
- The Department of Mechanical Engineering of the University of Thessaly for Financial Support (Scholarship).
- The National Scholarship Foundation (IKY) for Financial Support (Scholarship).

My current and former colleagues', in the Laboratory of Materials, contributions to this work must be emphasized: Dr. Apostolos Vassilakos, Dr. Antonis Katsamas, Dr. Nikos Hassiotis, Mrs Eleanna Pappa and finally Mrs. Anna Zervaki my very dear friend whose support and advice is indispensable.

I would also like to express my thanks to my friends, who are thought not directly related to my work, they provided fruitful discussions and endless entertainment, in particular Sava Douvartzidis, George Stratakis, Stelios Koukoumialos, Katerina Argyriadi, John Stamos and Roxani Athousaki.

Finally I would like to express my heartfelt thanks to my parents for the financial support all these years but mainly for the love they lavished on me.

# Ευχαριστίες

Οι ευχαριστίες για την οικονομική και πνευματική υποστήριξη κατά την διάρκεια της διδακτορικής διατριβής δεν είναι δυνατόν να συμπεριληφθούν σε λίγες γραμμές. Το γράψιμο της διατριβής αποτελεί το τελευταίο στάδιο του ερευνητικού έργου ενός ατόμου. Η συνολική δουλειά όμως πάντα εκτελείται ή υποβοηθάται από ένα μεγάλο αριθμό ατόμων. Θέλω να ευχαριστήσω όσους με οποιονδήποτε τρόπο έχουν συνεισφέρει στην ολοκλήρωση της διδακτορικής μου διατριβής.

Πρωτίστως πρέπει να εκφράσω την ευγνωμοσύνη μου στους επιβλέποντες καθηγητές μου, τον Καθηγητή Γρηγόρη Χαϊδεμενόπουλο και τον Καθηγητή Βασίλη Μποντόζογλου, για την βοήθεια που μου παρείχαν όλα αυτά τα χρόνια, την επιμονή τους και ιδιαίτερα την απέραντη υπομονή κατά την διάρκεια της ολοκλήρωσης του κειμένου. Χωρίς την υποστήριξη τους και την απλόχερη παροχή των γνώσεων και των συμβουλών τους η παρούσα διατριβή δεν θα είχε ολοκληρωθεί.

Οι βαθύτατες ευχαριστίες εκτείνονται και στον Καθηγητή Σπύρο Παντελάκη από το Πανεπιστήμιο Πατρών για την παροχή των αποτελεσμάτων των μηχανικών δοκιμών και την εγκάρδια συνεργασία μας κατά την διάρκεια της διατριβής. Ιδιαίτερες ευχαριστίες πρέπει να εκφράσω στον Δρ. Αλέξη Κερμανίδη και τον Παρασκευά Πετρογιάννη, για την άψογη συνεργασία μας σε διάφορα ερευνητικά προγράμματα.

Θα ήθελα να ευχαριστήσω τα υπόλοιπα μέλη της επταμελούς εξεταστικής επιτροπής Καθηγητές κ.κ. Γ. Παπαδημητρίου (Ε.Μ.Π.), Β. Παπαζογλου (Ε.Μ.Π.), Δ. Τσιπά (Α.Π.Θ) και Π. Τσιακάρα (Π.Θ.), για το ενδιαφέρον που επέδειξαν για την παρούσα διδακτορική διατριβή.

Θα ήθελα να εκφράσω την ευγνωμοσύνη μου στις εταιρίες και τους οργανισμούς που χρηματοδότησαν την έρευνα, στην οποία στηρίχθηκε αυτή η διατριβή. Πιο συγκεκριμένα:

- Την ΓΓΕΤ (Γενική Γραμματεία Έρευνας και Τεχνολογίας) για την οικονομική υποστήριξη που μου παρείχε μέσω του ερευνητικού προγράμματος ΠΕΝΕΔ.
- Την εταιρία Airbus για την προμήθεια υλικού και οικονομικής στήριξης. Ιδιαίτερα θα ήθελα να ευχαριστήσω τους Dr Tempus and Dr Zink για τις χρήσιμες πληροφορίες που παρείχαν.
- Το τμήμα Μηχανολόγων Μηχανικών Βιομηχανίας του Πανεπιστημίου Θεσσαλίας για την οικονομική υποστήριξη (υποτροφία).
- Το Ίδρυμα Κρατικών Υποτροφιών (ΙΚΥ) για την οικονομική υποστήριξη (υποτροφία).

Θα ήθελα να ευχαριστήσω τωρινούς και παλαιότερους συναδέλφους μου στο Εργαστήριο Υλικών, οι οποίοι συντέλεσαν ενεργά στην ολοκλήρωση της διατριβής: τον Αποστόλη Βασιλάκο, τον Αντώνη Κατσαμά, τον Νίκο Χασιώτη, την γραμματέα μας Ελεάνα Παππά και τέλος την πολύ καλή μου φίλη Άννα Ζερβάκη, για την ηθική υποστήριξη και τα καίρια σχόλια της.



Θέλω επίσης να ευχαριστήσω τους φίλους μου, οι οποίοι παρότι δεν αναμείχθηκαν άμεσα στην δουλειά, μου παρείχαν ατελείωτες ώρες συζητήσεων και διασκέδασης και ανέχθηκαν τις ιδιοτροπίες μου. Πιο συγκεκριμένα τον Σάββα Δουβαρτζίδα, τον Γεώργιο Στρατάκη, τον Στέλιο Κουκούμιαλο, τον Γιάννη Στάμο, την Κατερίνα Αργυριάδη και την Ρωξάνη Αθουσάκη.

Τέλος θέλω να εκφράσω τη βαθειά ευγνωμοσύνη μου στους γονείς μου για την οικονομική υποστήριξη όλα αυτά τα χρόνια αλλά πάνω απ' όλα για την αγάπη τους.

# Chapter 1 - Introduction

## *Description of the problem*

Corrosion presents a major concern to the structural integrity of aging aircraft structures. As the time of an aircraft structure in service increases, there is a growing probability that corrosion will interact with other forms of damage, such as single fatigue cracks or multiple-site damage in the form of widespread cracking at regions of high-stress gradients; it can result in loss of structural integrity and may lead to fatal consequences. Thus, the effect of corrosion on the damage tolerance ability of advanced aluminum alloys calls for a very diligent consideration of the problems associated with the combined effect of corrosion and embrittling mechanisms. There has been, recently, an increasing attention of basic research and development concerning structural integrity taking into account the related corrosion aspects [1-3]. It has been realized that the establishment of damage functions for quantifying the simultaneous accumulation of corrosion and fatigue-induced damage is very complex and difficult. Therefore, despite the advancements in modelling fatigue crack growth [4-7] and multiple-site damage phenomena [1-3], the assessment of structural degradation in aging aircraft is still relying heavily on test data. To face the corrosion-induced structural degradation issue, available data usually refer to accelerated laboratory corrosion tests and, more rarely, to in-nature atmospheric or marine exposure corrosion tests.

With the exception of the atmospheric corrosion test where, according to the relevant specification the tensile properties of corroded specimens are measured as well, these tests are used for evaluating the corrosion susceptibility of the materials by measuring weight loss and characterizing depth and type of corrosion attack. The above methodology toward understanding corrosion susceptibility of a material does not relate corrosion to their effect on the materials mechanical behavior and residual properties. Yet, it is exactly these missing data that are needed to face structural integrity problems of corroded aircraft components. Corrosion-induced mechanical degradation studies have been based mainly on the results of stress corrosion cracking tests [8, 9] or, more rarely on the results of fatigue tests performed in the presence of a corrosive environment [1-3]. Both types of tests provide useful results; they refer, however, to the case where a material is loaded in a corrosive environment but not to situations where a corroded material is subjected to mechanical loads. Present-day considerations of the corrosion-induced structural degradation relate the presence of corrosion with a decrease of the load-bearing capacity of the corroded structural member [2, 10].

This decrease is associated with the presence of corrosion notches that lead to local increase of stress promoting fatigue crack initiation as well; in addition, corrosion-induced reduction of the members' load-bearing thickness which, in the case of the thin alloy skin sheets, may be essential, can lead to appreciable increase of stress gradients [10]. Corrosion-induced material embrittlement is not accounted for. The above consideration of the corrosion-induced structural integrity issue is consistent with the classical understanding of the corrosion attack of aluminum alloys as the result of complex oxidation processes at the materials surface.

The above considerations gain particular importance if the so-called “aging aircraft” issue is considered. The aging aircraft has accumulated corrosion damage over the service life and its residual life depends on possible degradation stemming from corrosion-induced embrittling mechanisms. One characteristic example where failure was attributed to corrosion-induced multi-site damage (MSD) has been the Aloha Airlines accident in 1988, Fig. 1. The Figure insert shows the possible mechanism of damage, i.e. growth and linkage of multiple fatigue cracks, emanating from rivet holes. Recent investigations in the Hellenic Aerospace Industry (HAI) on firefighting planes has shown considerable corrosion damage around rivet holes (Fig. 2).

There are two key questions regarding this issue:

1. Is there a corrosion-induced degradation of ductility, which in turn degrades damage tolerance and the residual life of aerostructures?
2. What is the underlying corrosion-induced embrittling mechanism?

The answer to the first question has been given by the long series of experiments, conducted at the Univ. of Patras [11, 12], on mechanical testing of pre-corroded (in EXCO) alloy 2024. It was shown that (i) degradation of ductility increases with corrosion exposure time and (ii) removal of the corrosion layer restores strength but not ductility. These results indicated the operation of a bulk corrosion-induced embrittlement mechanism. The researchers at the Univ. of Patras pointed that hydrogen embrittlement might be the underlying mechanism. Furthermore in [13], the reduction in tensile ductility was associated with the reduction of fracture toughness of the corroded material and the concept of local fracture toughness was introduced. A fracture toughness model, based on a multiscale concept, has been proposed to calculate the local fracture toughness of a material element ahead of the crack tip [13].

### ***Thesis objectives***

In view of the above considerations, the present thesis tries to answer the second question posted above, i.e. what is the underlying corrosion-induced embrittlement mechanism. Is it hydrogen embrittlement?

The thesis objectives are therefore the following:

1. To establish a link, if any, between corrosion and hydrogen uptake and trapping.
2. To establish a link, if any, between hydrogen trapping and the observed embrittlement.

### ***Thesis methodology***

Research was focused on aircraft aluminum alloy 2024 in the T3 temper. The experimental procedures involved the following actions:

- (1) Accelerated corrosion testing (using the EXCO procedure),
- (2) Detailed microstructural investigation of the evolution of corrosion damage by employing AFM, stereo-microscopy, SEM and metallography,
- (3) Hydrogen measurements by employing an in-house thermal desorption – gas chromatography system,
- (4) Detailed fractographic analysis of tensile specimens. The tension tests were performed at the Univ. of Patras. The results of the tension tests were correlated with the hydrogen measurements, the microstructural evolution of corrosion damage and the fractographic analysis of the tensile specimens in order to reach to the thesis conclusions

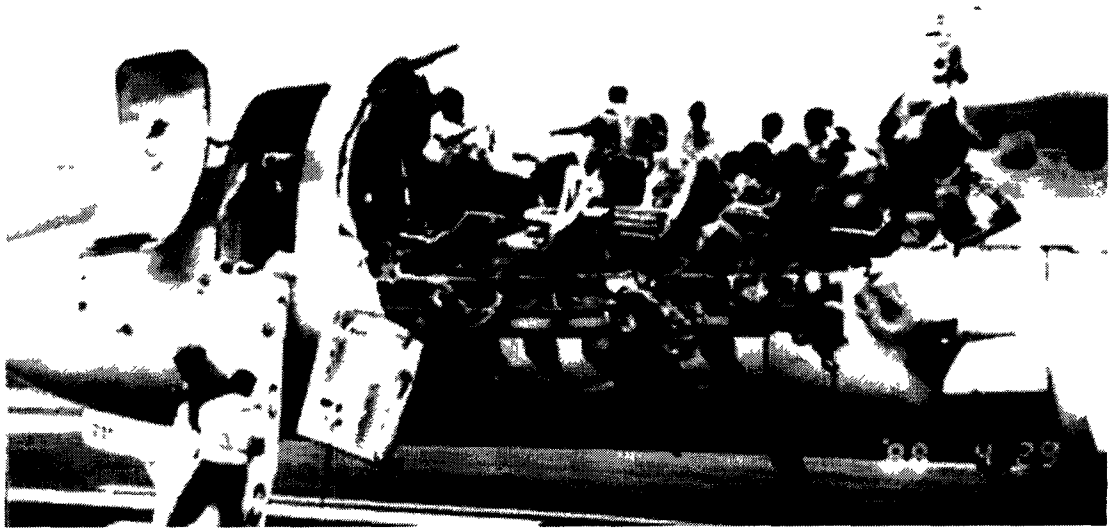
### ***Thesis originality***

The corrosion-induced degradation of mechanical behavior has been considered mainly by stress corrosion cracking or corrosion fatigue tests, where mechanical testing is performed in a corrosive environment. This thesis is targeted to provide understanding of the embrittlement mechanisms that lead to degradation of mechanical behavior and loss of residual strength after corrosion. It is the first experimental work to our knowledge that provides evidence of hydrogen trapping and microstructural evidence of hydrogen embrittlement in high-strength aircraft aluminum alloys.

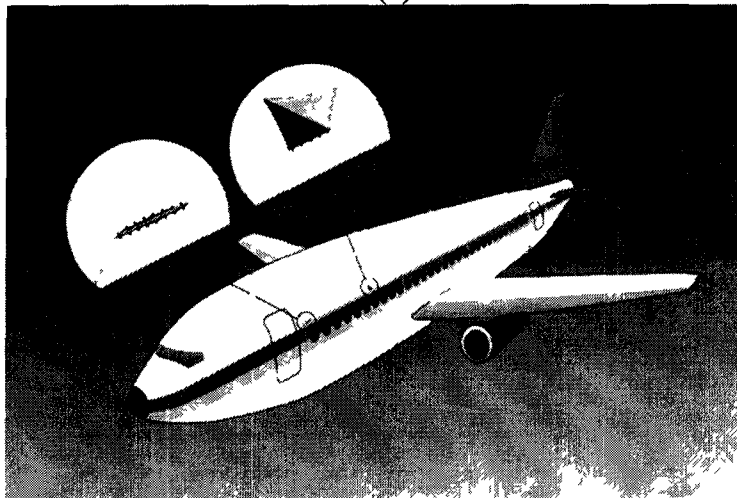
### ***Thesis support***

This thesis has been financially supported in part by the following programs/grants:

- PENED 99ED649 ‘Corrosion and hydrogen embrittlement of aircraft aluminium alloys’, Greek Secretariat of Research and Technology, 2000-2002
- Grant from the Graduate Course Program of the Department of Mechanical and Industrial Engineering of the University of Thessaly, 2003
- Grant from the National Scholarship Foundation (IKY)
- Research grant from Airbus, Germany, 2003-2004



(a)



(b)

Fig. 1: Photo from Aloha Airlines accident. Insert: possible cause of damage was cracking between rivet holes.

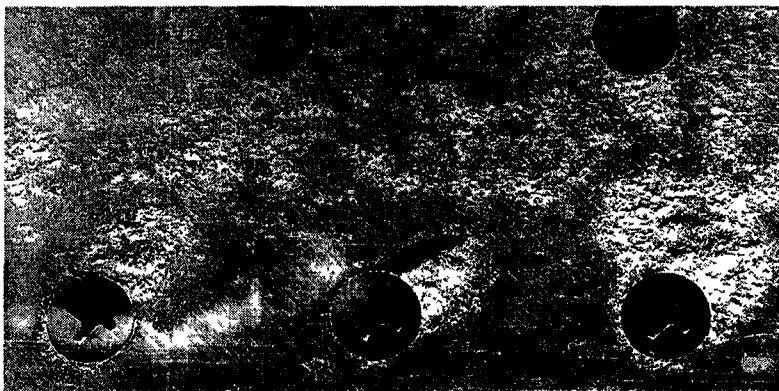


Fig. 2: Corrosion around rivet holes in 2024 alloy in firefighter planes (source Hellenic Aerospace Industry (H.A.I)).

# Chapter 2 - Bibliographic Review

The bibliographic review presented in the following pages, in addition to presenting the state of the art for the subject, aims at a short discussion of the key subjects of this thesis. The review starts with a brief introduction on Al-alloys (age hardening, damage tolerance). It continues with a discussion of corrosion of 2xxx and 6xxx alloys, emphasizing the forms of corrosion (pitting, intergranular corrosion, SCC and exfoliation). Finally there is a critical discussion of hydrogen damage in alloys and hydrogen embrittlement of Al-alloys.

## 2.1 The aircraft aluminium alloys of the 2xxx and 6xxx series

### *Metallurgical characteristics and hardening processes*

The strength of aluminum alloys, rivals that of mild carbon steel, and can approach 700 MPa. Combination of high strength and light weight makes aluminum especially well suited to aircraft industry. Alloy 2024 T3, because of its high strength-to-density ratio and corrosion resistance is used in the aircraft industry for numerous applications such as fuselage, door skin and trailing edge panels.

This alloy belongs in the 2xxx series, of wrought aluminum alloys; they are usually referred to as aircraft alloys. The primary alloying element for this group is copper, which produces high strength but reduced corrosion resistance (Table 1). These alloys were among the first aluminum alloys developed and were originally called duralumin. Alloy 2024 is perhaps the best known and most widely used alloy in the aircraft industry.

Alloys of the 6xxx series are also used in aerospace industry. Alloys in this group contain magnesium and silicon in proportions that form magnesium silicide ( $Mg_2Si$ ). These alloys have a good balance of corrosion resistance and strength. Alloy 6061 is one of the most popular and has a yield strength comparable to mild carbon steel.

Table 1: Wrought Alloy Designation System and Characteristics.

Series Number	Primary Alloying Element	Relative Corrosion Resistance	Relative Strength	Heat Treatment
1xxx	None	Excellent	Fair	Non-heat-treatable
2xxx	Copper	Fair	Excellent	Heat treatable
3xxx	Manganese	Good	Fair	Non-heat-treatable
4xxx	Silicon	Fair	Fair	Non-heat-treatable
5xxx	Magnesium	Good	Good	Non-heat-treatable
6xxx	Magnesium and silicon	Good	Good	Heat-treatable
7xxx	Zinc	Fair	Excellent	Heat-treatable

Some alloys (such as 2024) are protected by a thin coating of pure aluminum or corrosion-resistant aluminum alloy, the resulting product is called al-clad. This cladding is metallurgically bonded to one or both sides of the sheet or plate and may be 1.5-10% of its overall thickness. The cladding alloy is chosen so that it is anodic to the core alloy and protects it from corrosion. Any corrosion that occurs proceeds only to the cladding-core interface and then spreads laterally, making cladding very effective in protecting thin materials.

Heat treatable aluminum alloys like 2024 and 6013 own their remarkable mechanical properties to age hardening. Heat treatment normally involves the following stages:

- (1) Solution treatment at a relatively high temperature within the single-phase region in order to dissolve the alloying elements.
- (2) Rapid cooling or quenching, usually to room temperature, to obtain a supersaturated solid solution (SSSS) of these elements in aluminium.
- (3) Controlled decomposition of the SSSS to form a finely dispersed precipitate, usually by ageing for specified times at one and sometimes two intermediate temperatures.

The complete decomposition of an SSSS is a complex process which may involve several stages. Typically, Guinier-Preston (GP) zones and an intermediate precipitate may form prior to the equilibrium phase and may also coexist with the equilibrium phase. The GP zones are ordered, solute-rich clusters of atoms which may be only one or two atom planes in thickness. They retain the structure of the matrix and are coherent with it, although they produce appreciable elastic strains. Their formation requires movements of atoms over relatively short distances so that they are very finely dispersed in the matrix with densities which may be as high as  $10^{17}$  to  $10^{18}$  cm<sup>-3</sup>. The intermediate precipitate is normally much larger in size than a GP zone and is only partly coherent with the lattice planes of the matrix. It has a definite composition and crystal structure which may differ only slightly from those of the equilibrium precipitate. In some alloys, the intermediate precipitate may be nucleated from, or at, the sites of stable GP zones. In others this phase nucleates heterogeneously at lattice defects such as dislocations. Formation of the final equilibrium precipitate involves complete loss of coherency with the parent lattice. It forms only at relatively high ageing temperatures and, because it is coarsely dispersed, little hardening results. Maximum hardening in commercial alloys occurs with the formation of a critical dispersion of GP zones, or an intermediate precipitate, or both. In some cases the alloys are cold worked (e.g. by stretching 5%) after quenching and before ageing, thus increasing dislocation density and providing more sites at which heterogeneous nucleation of intermediate precipitates may occur. The precipitation sequence of Al-Cu, Al-Cu-Mg [14-26] and Al-Mg-Si alloys [27-33] is illustrated in Table 2 [34].

If precipitate particles are large and widely spaced, they can be readily bypassed by moving dislocations which bow out between them by a mechanism first proposed by Orowan [34]. Loops of dislocations are left around the particles. The yield strength of the alloy is low but the rate of work-hardening is high, and plastic deformation tends to be spread more uniformly throughout the grains. Accompanying the formation of the intermediate precipitate is the development of wider, precipitate-free zones adjacent to grain boundaries. These zones are relatively weak with respect to the age-hardened matrix and may deform preferentially leading to high stress concentrations at triple points which, in turn, may cause premature cracking.

Table 2 The precipitation sequence of 2xxx and 6xxx alloys [34]

Alloy	Precipitates	Remarks
Al-Cu	GP zones as thin plates on $\{100\}$ $\theta'$ (formerly GP zones)	Probably single layers of copper atoms on $\{100\}_\alpha$ Coherent, probably two layers of copper atoms separated by three layers of aluminium atoms May be nucleated at GP zones
	$\theta'$ tetragonal $\text{Al}_2\text{Cu}$ $a = 0.404 \text{ nm}$ $c = 0.580 \text{ nm}$	Semi-coherent plates nucleated at dislocations Form on $\{100\}_\alpha$
	$\theta$ body-centred tetragonal $\text{Al}_2\text{Cu}$ $a = 0.607 \text{ nm}$ $c = 0.487 \text{ nm}$	Incoherent equilibrium phase May nucleate at surface of $\theta$
Al-Cu-Mg	GP (Cu, Mg) zones as rods along $\langle 100 \rangle$	GP zones form very rapidly in most compositions aged at elevated temperatures Sometimes known as GPB zones
	S' orthorhombic $\text{Al}_2\text{CuMg}$ $c = 0.718 \text{ nm}$ $b = 0.925 \text{ nm}$ $a = 0.404 \text{ nm}$	Semi-coherent and nucleated at dislocations Forms as laths in $\{210\}$ , along $\langle 001 \rangle$ ,
	S orthorhombic $\text{Al}_2\text{CuMg}$ $a = 0.400 \text{ nm}$ $b = 0.923 \text{ nm}$ $c = 0.714 \text{ nm}$	Incoherent equilibrium phase, probably transforms from S Note that precipitates from the Al-Cu system can also form in compositions with high Cu Mg ratios
Al-Mg	Spherical GP zones	GP zones solvus below room temperature if $<5\%$ Mg and close to room temperature in compositions between 5 and 10% Mg
	$\beta'$ hexagonal $a = 1.002 \text{ nm}$ $c = 1.636 \text{ nm}$	Probably semi-coherent Nucleated on dislocations $(0001)_\beta // (001)_\alpha, [0110]_\beta // [110]_\alpha$
	face-centred cubic $\text{Mg}_5\text{Al}_3$ (formerly $\text{Mg}_2\text{Al}_3$ ) $a = 2.824 \text{ nm}$	Incoherent, equilibrium phase Forms as plates or laths in grain boundaries and at a surface of $\beta'$ particles in matrix $(111)_\beta // (001)_\alpha, [110]_\beta // [010]_\alpha$
Al-Mg-Si	Clusters of Mg and Si atoms GP zones?	GP zones solvus occurs at temperatures that are normally higher than the ageing temperatures
	B'' monoclinic $a = 1.534 \text{ nm}$ $b = 0.405 \text{ nm}$ $c = 0.683 \text{ nm}$ $p = 106^\circ$	Coherent needles, lie along $\langle 100 \rangle_\alpha$ $(010)_\beta // (001)_\beta // (001)_\alpha, [001]_\beta // [310]_\alpha$
	B' hexagonal $\text{Mg}_2\text{Si}$ $a = 0.705 \text{ nm}$ $c = 0.405 \text{ nm}$	Semi-coherent rods, lie along $\langle 100 \rangle_\alpha$ $(0001)_\beta // (100)_\alpha, (1010)_\beta // [510]_\alpha$ May form from $\beta''$
	B' hexagonal $a = 1.04 \text{ nm}$ $c = 0.405 \text{ nm}$	Semi-coherent laths, lie along $\langle 100 \rangle_\alpha$ $(0001)_B // (001)_\alpha, (1010)_B // [510]_\alpha$ Forms together with $\beta$ , favoured by high Si Mg ratios
	B face-centred cubic $\text{Mg}_2\text{Si}$ $a = 0.639 \text{ nm}$	Platelets on $\{100\}$ May transform directly from, $(100)_\beta // (100)_\alpha, [110]_\beta // [100]_\alpha$



### ***Fatigue Consideration and the damage tolerant design***

The effect of fatigue on aircraft integrity began to be considered as long as 70 years ago. Design methods that consider fatigue as a constraint were introduced. Today, there are 2 conceptual approaches to calculating fatigue-limited structural life: “safe life” and “fail safe”. In the “safe-life” approach to fatigue design, the typical cyclic load spectra, which are imposed on a structural component in service, are first determined. On the basis of this information, the components are analyzed or tested in the laboratory under load conditions which are typical of service spectra and a useful fatigue life is estimated for the component. The estimated fatigue life suitably modified with a factor of safety (or an ignorance factor), then provides a prediction of “safe-life” for the component. At the end of the expected safe operation life, the component is automatically retired from service, even if no failure has occurred during service (and the component has considerable residual fatigue life). Safe life design was introduced in the 1930s and 1940s and relies strongly on detailed knowledge of service experience and requires rigorous product testing. By selecting a large margin of safety, a safe operating life can be guaranteed, although such a conservative approach may not be desirable from the view points of economy and performance.

“Fail safe” design was introduced in the 1950s and assures that catastrophic failure is not probable as the result of a failure of a single structural element. The “fail-safe” concept is based on the argument that, even if an individual member of a large structure fails, there should be sufficient structural integrity in the remaining parts to enable the structure to operate safely until the crack is detected. To achieve this result, “fail-safe” designs incorporate redundant crack pathways in the design. The fail-safe approach mandates periodic inspections along with the requirement that the crack detection techniques be capable of identifying flaws to enable prompt repairs or replacements.

Finally, damage tolerance was introduced in the late 1960s and early 1970s, and couples crack growth analysis with periodic inspections to detect cracks and remove cracked load bearing members from service in situations where these would have a high probability of failure prior to the next scheduled inspection [35]. Damage tolerance became recognized as an important issue in 1954 when three Comet jet airplanes, manufactured with 7075-type aluminum, crashed [35]. The cause of the crashes was attributed to premature fatigue failure of the pressurized fuselage associated with stress concentrations at windows and hatches. Today, fracture toughness and fatigue crack growth have been incorporated as a primary design criterion in many products in the same manner as strength was used several decades ago.

The basic premise here is that all engineering components are inherently flawed. The size of a pre-existing flaw is generally determined from non-destructive flaw detection techniques. If no flaw is found in the component, proof tests are conducted whereby a structure is subjected to a simulation test *a priori* at a stress level slightly higher than the service stress. If no cracks are detected by the non-destructive test method and if catastrophic failure does not occur during the proof test, the larger (undetected) initial crack size is estimated from the resolution of the flaw detection technique. The useful fatigue life is then defined as the number of fatigue cycles or time to propagate the dominant crack from this initial size to some critical dimension. The choice of the critical size for the fatigue crack may be based on the fracture toughness of the material, the limit load for the particular structural part, the allowable strain or the permissible change in the compliance of the component. The prediction of crack propagation life using the defect-tolerant approach involves empirical crack growth laws based on fracture mechanics. This intrinsically conservative approach to fatigue has been widely used in fatigue-critical applications where catastrophic failures will result in the loss of human lives; examples include the aerospace and nuclear industries.

Beginning in the '80s, jet powered flight had become "the standard" and other considerations for aircraft such as fuel costs, the revenue opportunities associated with increasing range and payload, and reducing landing weight fees again returned the technical focus to weight reduction but without sacrificing life. Then, in the '90s, the realization of the benefits of extending the life of the aging aircraft fleet resulted in a technical focus on improved damage tolerance and improved corrosion resistance. The currently used airframe design methods have evolved over many years and the practices employed today incorporate both the benefit of this past experience and availability of better analytical methods. Static strength has been an important first order consideration since the beginning of flight and aircrafts are usually designed to withstand a maximum operating load plus a safety factor, which is typically 1.5. In modern aircraft, static strength is necessary but not sufficient, largely because of the prolonged service lives expected of the aircraft.

### ***Corrosion and Residual life***

The advantage of the damage tolerant design philosophy is obviously the ability to treat cracked objects in a direct and appropriate fashion. The previous methods only allow for the immediate removal of cracked structure. Use of the stress-intensity values and appropriate data (properties) allows the number of cycles of crack growth over a range of crack sizes to be estimated and fracture to be predicted. The clear tie of crack size, orientation, and geometry to non-destructive evaluation (NDE) is also a plus. Disadvantages are: possibly computationally intensive stress-intensity factor determinations, greater complexity in development and modelling of property data, and the necessity to perform numerical integration to determine crack growth. In addition, the predicted lives are considerably influenced by the initial crack size used in the calculation, requiring quantitative development of probability of detection for each type of NDE technique employed. Related to the initial crack size consideration is the inability of this approach to model effectively that the component was actually suitable for modelling as a continuum, which eliminates the so-called "initiation" portion of the part life. It becomes obvious that complete knowledge of preexisting cracks and their propagating paths must be available.

A major factor introducing cracks in materials is corrosion that produces cracking of metals as a result of exposure to the aggressive environment. This cracking may take the form of relatively slow, stable crack extension or, as is often the case, unpredictable catastrophic fracture. Investigations involving information on the residual mechanical properties of a structural material following exposure to corrosive environment were conducted by Pantelakis et al. [11, 12], and the effect of corrosion and hydrogen embrittlement on the mechanical behavior of aluminum aircraft alloys was investigated. The work was based on extended, new experimental data of the aircraft aluminum alloys 2024, 6013, 2091, and 8090. Evaluation of corrosion resistance was performed based on the tensile behavior following several types of corrosion tests. The results were interpreted in terms of current concern about the effect of corrosion on structural integrity analysis of aged aircrafts. Results on the fatigue behavior of corroded 2024 alloy specimens were presented as well. Finally, the obtained results were discussed under the viewpoint of hydrogen embrittlement.

## **2.2 The corrosion of high-strength aluminium alloys**

It has become clear that a profound understanding and efficient control of corrosion phenomena is essential, for the reliable extension of aircraft service life.

Aluminum, as indicated by its position in the electromotive force series, is a thermodynamically reactive metal; among structural metals, only beryllium and magnesium are more reactive. Aluminum owes its excellent corrosion resistance to the protective oxide

film that is bonded strongly to its surface and that, if damaged, reforms immediately in most environments. The conditions for thermodynamic stability of the oxide film are expressed by the Pourbaix (electrochemical potential versus pH) diagram. Aluminum is passive (protected by its oxide film) in the pH range of about 4 to 8.5. The limits of this range, however, vary somewhat with temperature, with the specific form of oxide film present, and with the presence of substances that can form soluble complexes or insoluble salts with aluminum. Beyond the limits of its passive range, aluminum corrodes in aqueous solutions because its oxides are soluble in many acids and bases, yielding  $\text{Al}^{3+}$  ions in the former and  $\text{AlO}_2^-$  (aluminate) ions in the latter.

Corrosion of aluminum in the passive range is localized, usually manifested by random formation of pits. For aluminum, pitting corrosion is most commonly produced by halide ions, of which chloride ( $\text{Cl}^-$ ) is the most frequently encountered in service. Pitting of aluminum in halide solutions open to the air occurs because, in the presence of oxygen, the metal is readily polarized to its pitting potential. Generally, aluminum does not develop pitting in aerated solutions of most nonhalide salts because its pitting potential in these solutions is considerably more noble (cathodic) than in halide solutions, and it is not polarized to these potentials in normal service.

Because of the electrochemical nature of corrosion processes, relationships among solution potentials of different aluminum alloys, as well as between potentials of aluminum alloys and those of other metals, are of considerable importance. Furthermore, the solution-potential relationships among the microstructural constituents of a particular alloy significantly affect its corrosion behavior. Compositions of solid solutions and additional phases, as well as amounts and spatial distributions of the additional phases, may affect both the type and extent of corrosion.

### ***2xxx wrought alloys***

2xxx wrought alloys, in which copper is the major alloying element, are less corrosion-resistant than alloys of other series that contain much lower amounts of copper. Electrochemical effects on corrosion can be stronger in these alloys than in alloys of many other types because of two factors: greater change in electrode potential with variations in the amount of copper in solid solution; and, under some conditions, the presence of nonuniformities in solid-solution concentration. However, the fact that general corrosion resistance decreases with increasing copper content is not primarily attributable to these solid-solution or second-phase solution-potential relationships, but rather to galvanic cells created by formation of minute copper particles or films deposited on the alloy surface as a result of corrosion. As corrosion progresses, copper ions, which initially go into solution, replate onto the alloy to form metallic copper cathodes. The reduction of copper ions and the increased efficiency of  $\text{O}_2$  and  $\text{H}^+$  reduction reactions in the presence of copper increase the corrosion rate.

It is generally acceptable that pitting constitutes the precursor for every other type of corrosion; the creation of pits is virtually the first stage of corrosion. Pits first appear in regions where surface abnormalities with respect to the matrix are present. For example on grain boundaries, where during the precipitation of intermetallic second phase particles, a neighbouring area poor in compound elements is created. If the boundary precipitates are anodic with respect to the matrix and the precipitate free zone, then these particles are selectively dissolved. In the opposite case the neighbouring area poor in compound elements is attacked [36]. On grain boundaries of an alloy belonging to the 2xxx series, for example, they selectively create anodic regions that make the material sensitive to corrosion.

Other researchers have shown that the anodic nature of grain boundaries can be attributed to the segregation in these regions, with regard to the grain interior. Guillaumin et

al. observed on grain boundaries of 2024 acicular precipitates  $\text{Al}_2\text{CuMg}$  as well as particles of S phase [37]. Generally galvanic cells are created between regions rich in Cu (S phase) and neighbouring regions poor in compound elements. From studies in different corrosive environments it was concluded that  $\text{Cl}^-$  ion is the most aggressive [38]. As a result of the severe presence of  $\text{Cl}^-$  ions, the marine environment is highly corrosive [39].

### ***6xxx Wrought Alloys***

Moderately high strength and very good resistance to corrosion make the heat-treatable wrought alloys of the 6xxx series (aluminum-magnesium-silicon) highly suitable in various structural, buildings, marine, machinery, and process-equipment applications. The  $\text{Mg}_2\text{Si}$  phase, which is the basis for precipitation hardening, is unique in that it is an ionic compound and is not only anodic to aluminum but is also reactive in acidic solutions. However, either in solid solution or as sub microscopic precipitate,  $\text{Mg}_2\text{Si}$  has a negligible effect on electrode potential. Because these alloys are normally used in the heat-treated condition, no detrimental effects result from the major alloying elements or from the supplementary chromium, manganese, or zirconium added to control grain structure. Copper additions, which augment strength in many of these alloys, are limited to small amounts to minimize effects on corrosion resistance. In general, the level of resistance decreases somewhat with increasing copper content. When the magnesium and silicon contents in a 6xxx alloy are balanced (in proportion to form only  $\text{Mg}_2\text{Si}$ ), corrosion by intergranular penetration is slight in most commercial environments. If the alloy contains silicon beyond that needed to form  $\text{Mg}_2\text{Si}$  or contains a high level of cathodic impurities, susceptibility to intergranular corrosion increases.

### ***Intergranular Corrosion***

Another form of corrosion is intergranular (intercrystalline) corrosion, which is selective attack of grain boundaries or closely adjacent regions without appreciable attack of the grains themselves. Intergranular corrosion is a generic term that includes several variations associated with different metallic structures and thermomechanical treatments. Intergranular corrosion is caused by potential differences between the grain-boundary region and the adjacent grain bodies. The location of the anodic path varies with the different alloy systems: In 2xxx series alloys, it is a narrow band on either side of the boundary that is depleted in copper. The 6xxx series alloys generally resist this type of corrosion, although slight intergranular attack has been observed in aggressive environments. Because intergranular corrosion is involved in SCC of aluminum alloys, it is often presumed to be more deleterious than pitting or general corrosion. However, in alloys that are not susceptible to SCC (e.g., the 6xxx series alloys) intergranular corrosion is usually no more severe than pitting corrosion and tends to decrease with time. For equal depth of corrosion, its effect on strength is also no greater than that of pitting corrosion, although fatigue cracks may be more likely to initiate at areas of intergranular corrosion than at random pits.

### ***Stress corrosion cracking and Corrosion fatigue***

Stress-corrosion cracking (SCC) is a term used to describe service failures in engineering materials that occur by slow environmentally induced crack propagation. The observed crack propagation is the result of the combined and synergistic interaction of mechanical stress and corrosion reactions. This is a simple definition of a complex subject, and like most simplifications, it fails to identify the boundaries of the subject. Environments that cause SCC are usually aqueous and can be condensed layers of moisture or bulk solutions. Typically, SCC of an alloy is the result of the presence of a specific chemical

species in the environment. Thus, chloride ions cause cracking in stainless steels and aluminum alloys [40, 41].

Only aluminum alloys that contain appreciable amounts of soluble alloying elements, primarily copper, magnesium, silicon, and zinc, are susceptible to SCC. For most commercial alloys, tempers have been developed that provide a high degree of immunity to SCC in most environments.

Stress-corrosion cracking in aluminum alloys is characteristically intergranular. According to the electrochemical theory, this requires a condition along grain boundaries that makes them anodic to the rest of the microstructure so that corrosion propagates selectively along them. Such a condition is produced by localized decomposition of solid solution, with a high degree of continuity of decomposition products along the grain boundaries. The most anodic regions may be either the boundaries themselves (most commonly, the precipitate formed in them) or regions adjoining the boundaries that have been depleted of solute.

In 2xxx alloys, the solute-depleted regions are the most anodic. The most anodic grain-boundary regions in other alloys have not been identified with certainty. Strong evidence for the presence of anodic regions and for the electrochemical nature of their corrosion in aqueous solutions is provided by the fact that SCC can be greatly retarded, if not eliminated, by cathodic protection. For alloys requiring microstructural control to avoid susceptibility, resistance is obtained by using treatments that produce precipitate throughout the microstructure, because precipitate always forms along boundaries, and its formation then usually cannot be prevented [42-46].

According to electrochemical theory, susceptibility to intergranular corrosion is a prerequisite for susceptibility to SCC, and treatment of aluminum alloys to improve resistance to SCC also improves their resistance to intergranular corrosion. For most alloys, however, optimum levels of resistance to these two types of failure require different treatments and resistance to intergranular corrosion is no a reliable indication of resistance to SCC.

Corrosion fatigue occurs in metals as a result of the combined action of a cyclic stress and a corrosive environment. Corrosion fatigue is dependent on the interactions among loading, environmental, and metallurgical factors. For a given material, the fatigue strength (or fatigue life at a given maximum stress value) generally decreases in the presence of an aggressive environment. The effect varies widely, depending primarily on the particular metal-environment combination. The environment may affect the probability of fatigue crack initiation, the fatigue crack growth rate, or both.

### ***Exfoliation corrosion***

In certain tempers, wrought products of aluminum alloys are subject to corrosion by exfoliation, which is sometimes described as lamellar, layer, or stratified corrosion. In this type of corrosion, attack proceeds along selective subsurface paths parallel to the surface. Layers of uncorroded metal between the selective paths are split apart and pushed above the original surface by the voluminous corrosion product formed along the paths of attack. Because it can be detected readily at an early stage and is restricted in depth, exfoliation does not cause unexpected structural failure, as does SCC.

Exfoliation occurs predominantly in products with markedly directional structures, in which highly elongated grains form platelets that are thin relative to their length and width. Susceptibility to this type of corrosion may result from the presence of aligned intergranular or subgrain boundary precipitates or from aligned strata that differ slightly in composition. The intensity of exfoliation increases in slightly acidic environments or when the aluminum is coupled to a cathodic dissimilar metal. Exfoliation is not accelerated by stress and does not lead to SCC. Alloys most susceptible to exfoliation are the heat-treatable 2xxx and 7xxx alloys and certain cold-worked 5xxx alloys. Exfoliation is primarily caused by unfavorable

distribution of precipitate. The processing to eliminate this form of attack promotes either more uniform precipitation within grains or a more advanced stage of precipitation. Thus, increases in precipitation heat-treating time or temperature are as effective in reducing susceptibility to exfoliation as they are in reducing susceptibility to SCC.

The occurrence of exfoliation in susceptible materials is remarkably influenced by environmental conditions. For example, forged truck wheels made of an aluminum-copper alloy (2024-T4) give corrosion-free service for many years in the warm climates of the southern and western United States, but exfoliate severely in only one or two years in the northern states, where de-icing salts are used on the highways during the winter months. Exfoliation corrosion initiates between bimetallic couples and progresses along grain boundaries as an intergranular crack. This intergranular crack widens into a crack plane and enlarges into multiple crack planes. Corrosive oxides press outward against the adjacent metal, thus producing a pattern of delamination [47, 48].

### ***Accelerated corrosion tests***

Accelerated laboratory tests do not precisely predict long-term corrosion behavior. However, they are frequently used when answers are needed quickly in the development of new materials. For this reason, accelerated tests are used to screen candidate alloys before conducting atmospheric exposures or other field tests. They are also sometimes used for quality control tests. Several new laboratory tests for exfoliation corrosion have been standardized in recent years under the jurisdiction of American Society for Testing and Materials (ASTM) Committee G- 1 on the corrosion of metals.

ASTM standard G 34 provides an accelerated exfoliation corrosion test for 2xxx and 7xxx alloys through the continuous immersion of test materials in an aqueous solution containing 4 M NaCl, 0.5 M potassium nitrate (KNO<sub>3</sub>), and 0.1 M HNO<sub>3</sub> at 25 °C. Susceptibility to exfoliation is determined by visual examination, using performance ratings established by reference standard photographs [49]. This method, known as the EXCO test, is primarily used in research and development and quality control of such mill products as sheet and plate. However, it should not be considered the optimal method for quality acceptance. Rather, this method provides a useful prediction of the exfoliation behavior of these alloys in various types of outdoor service, especially in marine and industrial environments. The test solution is very corrosive and is meant to represent the more severe type of environmental exposure.

It remains to be determined whether correlations can be established between EXCO test ratings and practical service conditions for given alloy. Outdoor exposure tests are being conducted for this purpose. For example, it has been reported that samples of 7xxx alloys rated EA (superficial exfoliation) or P (pitting) in 48 h EXCO test did not develop more than superficial exfoliation (EA rating) during six to nine-year exposures to seacoast atmospheres, while materials rated as EC or E (severe and very severe exfoliation, respectively) developed severe exfoliation within or one to seven years at the seacoast. It is anticipated that additional comparison will become available as the outdoor tests are extended.

## **2. 3 Hydrogen Damage in Alloys**

### ***General classification of hydrogen damage***

Hydrogen damage is a form of environmentally assisted failure that results most often from the combined action of hydrogen penetration and residual or applied tensile stress. Hydrogen damage to specific alloys or groups of alloys manifests itself in many ways, such as cracking, blistering, hydride formation and loss in tensile ductility. For many years, these

failures have been collectively termed hydrogen embrittlement and have been confused with other forms of environmentally induced failure; this term persists even though it is improperly used to describe a multitude of failure modes involving hydrogen, several of which do not demonstrate the classical features of embrittlement (that is reduced load carrying capability or fracture below the yield strength).

The specific types of hydrogen damage have been categorized in order to enhance the understanding of the factors that affect this behavior in alloys and to provide a basis for development and analysis of theories regarding different hydrogen damage mechanisms.

*Blistering* occurs predominantly in low-strength alloys when atomic hydrogen diffuses to internal defects, such as laminations or nonmetallic inclusions, and then precipitates as molecular hydrogen ( $H_2$ ). The pressure of molecular hydrogen can attain such high values that localized plastic deformation of the alloy occurs, forming a blister that often ruptures. Blisters are frequently found in low-strength steels that have been exposed to aggressive corrosive environments (such as  $H_2S$ ) or cleaned by pickling [50]. Shatter cracks, flakes, and fish eyes are features common to hydrogen damage in forgings, weldments, and castings. They are attributed to hydrogen pickup during melting operations when the melt has a higher solubility for hydrogen than the solid alloy. During cooling from the melt, hydrogen diffuses to and precipitates in voids and discontinuities, producing the features that result from the decreased solubility of hydrogen in the solid metal [51].

*Hydrogen environment embrittlement* occurs during the plastic deformation of alloys in contact with hydrogen bearing gases or a corrosion reaction and is therefore strain rate dependent. The degradation of the mechanical properties of ferritic steels, nickel-base alloys, titanium alloys, and metastable austenitic stainless steels is greatest when the strain rate is low and the hydrogen pressure and purity are high.

*Hydrogen stress cracking* often referred to as hydrogen-induced cracking or static fatigue is characterized by the brittle fracture of a normally ductile alloy under sustained load in the presence of hydrogen. Most often, fracture occurs at sustained loads below the yield strength of the material. Hydrogen stress cracking is associated with absorption of hydrogen and a delayed time to failure (incubation time) during which hydrogen diffuses into regions of high triaxial stress. The catastrophic cracking of steels in hydrogen sulfide ( $H_2S$ ) environments referred to as sulfide stress cracking is a special case of hydrogen stress cracking [50].

*Hydrogen attack* is a high-temperature form of hydrogen damage that occurs in carbon and low-alloy steels exposed to high pressure hydrogen at high temperatures for extended time. Hydrogen enters the steel and reacts with carbon either in solution or as carbides to form methane gas, which may result in the formation of cracks and fissures or may simply decarburize the steel resulting in a loss in strength of the alloy. This form of damage is temperature dependent, with a threshold temperature of approximately 200 °C [52, 53].

*Loss in tensile ductility* was one of the earliest recognized forms of hydrogen damage. Significant decreases in elongation and reduction in area are observed for steels, stainless steels, nickel-base alloys, aluminum alloys, and titanium alloys exposed to hydrogen. This mode of failure is most often observed in lower-strength alloys, and the extent of loss in tensile ductility is a function of hydrogen content of the material. Loss in tensile ductility behavior is strain rate sensitive and becomes more pronounced as the strain rate decreases [54].

*Degradation in flow properties* in hydrogen environments has been found at ambient temperatures for iron and steel and at elevated temperature for several alloy systems. The steady-state creep rate under constant load has been observed to increase in the presence of hydrogen for some nickel-base alloys.

*Hydride formation* produces embrittlement in magnesium, tantalum, niobium, vanadium, uranium, thorium, zirconium, titanium, and their alloys, as well as many other less common metals and alloys. The degradation of mechanical properties and the cracking of these metals and their alloys are attributable to the precipitation of metal hydride phases. Hydrogen pickup often results from welding, heat treating, charging from a corrosion process, or during melting of the alloy. Hydride formation is enhanced for some metal-hydrogen systems by the application of stress—the so-called stress-induced hydride formation. Alloy systems that form hydrides are generally ductile at high (>300 K) and low (< 100 K) temperatures at which they fracture by ductile rupture. This temperature dependence is comparable to that observed for the hydrogen embrittlement of ferrous and nickel alloys. Some of these alloys are also susceptible to failure in hydrogen by mechanisms other than hydriding. Some evidence exists that nickel and aluminum alloys may also form a highly unstable hydride that could contribute to hydrogen damage of these alloys; however, this possibility has not been confirmed.

### ***Mechanisms of Hydrogen Embrittlement***

As may be appreciated from the numerous classes of hydrogen damage, there are many explanations or theories for these various forms of degradation. The preeminent theories for hydrogen damage are based on pressure, surface adsorption, decohesion, enhanced plastic flow, hydrogen attack, and hydride formation. Although many other theories have been presented, most are variations on these basic models.

The *pressure theory* of hydrogen damage, or more specifically, hydrogen embrittlement, is one of the oldest models for hydrogen damage. This theory attributes hydrogen embrittlement to the diffusion of atomic hydrogen into the metal and its eventual accumulation at voids or other internal surfaces in the alloy. As the concentration of hydrogen increases at these microstructural discontinuities, a high internal pressure is created that enhances void growth or initiates cracking. This model, although apparently reasonable for blistering and possibly appropriate for some aspects of loss in tensile ductility, does not explain many of the factors observed for classes of failure such as hydrogen stress cracking. However, it is a well-recognized phenomenon that charging hydrogen into steel or nickel alloys at high fugacity, either with high pressure hydrogen gas or under extreme electrochemical charging, can create a significant density of voids and irreversible damage to the alloy consistent with a pressure-dependent model [55].

The *surface adsorption theory* suggests that hydrogen adsorbs on the free surfaces created adjacent to the crack tip, decreasing the surface free energy and thus the work of fracture. Reduction in the work of fracture would thus enhance crack propagation at stress levels below those typically experienced for a particular alloy in a benign environment. There are many arguments against this model. The principal criticism is that it greatly underestimates the work of fracture and does not account for the discontinuous crack growth that has been observed for hydrogen cracking.

*Decohesion* describes the effect of hydrogen on the cohesive force between atoms of the alloy matrix. Sufficiently high hydrogen concentrations that accumulate ahead of a crack tip are assumed to lower the maximum cohesive force between metal atoms such that the local maximum tensile stress perpendicular to the plane of the crack then becomes equivalent to or greater than the lattice cohesive force and fracture results.

*Enhanced plastic flow* is associated with hydrogen-dislocation interactions and is primarily based on fractographic observations. This approach proposes that atomic hydrogen enhances dislocation motion, generally screw dislocations, and the creation of dislocations at surfaces and/or crack tips leading to softening of the material on a localized scale [56, 57]. Although this behavior has been observed in certain steels, hardening by hydrogen has also



been found. Careful high-resolution electron microscopy of what appears to be brittle cleavage or intergranular fracture surfaces has revealed evidence of crack tip plasticity in support of this mechanism.

*Hydride formation* is the degradation of Group Vb metals (niobium vanadium, and tantalum) and zirconium, titanium [58] and magnesium in hydrogen environments by the formation of a brittle metal hydride at the crack tip. When sufficient hydrogen is available in the alloy, a metal hydride precipitates. Cracking of the hydride occurs, followed by crack arrest in the more ductile matrix or continued crack growth between hydrides by ductile rupture. Because hydride formation is enhanced by the application of stress, the stress field ahead of the crack tip may induce precipitation of additional hydrides that cleave. Thus, in some alloys, brittle crack propagation occurs by repeated precipitation of hydrides ahead of the crack tip, cleavage of these hydrides, and precipitation of new hydrides and so on until fracture is complete.

*Hydrogen Trapping.* Although numerous models exist, none adequately explains the behavior exhibited by alloys in different hydrogen bearing systems. Until a universal theory is developed, one must rely on the phenomenological behavior between the more prominent alloy systems to understand hydrogen damage. One of the principal factors that determines the hydrogen damage susceptibility of various alloys is a phenomenon referred to as trapping. Diffusion studies of iron and steels have shown an initial retardation in diffusion rate or lag time for hydrogen diffusion through these alloys before a steady-state diffusivity compatible with that expected theoretically is achieved [59, 60]. This lag time is generally considered to be related to the filling of traps by hydrogen. In fact, the apparent diffusivity of hydrogen in steels shows a precipitous decrease with increasing concentration of particles (traps). Hydrogen trapping may be considered the binding of hydrogen atoms to impurities, structural defects, or microstructural constituents in the alloy. Binding may be attributed to local electric fields and stress fields, temperature gradients, chemical potential gradients, or physical trapping. These hydrogen traps may be mobile (dislocations, stacking faults) or stationary (grain boundaries, carbide particles, individual solute atoms) [61, 62]. They may also be reversible or irreversible traps. Short-duration trapping of hydrogen in which the occupancy time is limited is referred to as reversible. A long residency time for hydrogen characterized by a high binding energy is termed irreversible trapping [63, 64]. Table 3 presents a classification of hydrogen traps in steels. The concept and investigation of trapping have been developed primarily for steels; however, it may not be restricted to this system [65]. Face-centered cubic alloys show a similar trapping behaviour, although at a somewhat reduced efficiency for trapping compared to steels [66].

Many factors affect the behavior of ferrous alloys in hydrogen-bearing environments. Hydrogen concentration, temperature heat treatment/microstructure, stress level (applied and yield stress), solution composition, and environment are the primary factors involved in determining susceptibility to hydrogen embrittlement. The longer the baking time, the lower the residual hydrogen in the steel matrix. In general, increasing the concentration of hydrogen in an alloy will reduce time to failure and the stress level at which failure will occur [67-72].

Table 3. Classification of hydrogen traps in steels [73]

Trap class	Example of trap		Interaction energy, eV	Character if known	Influence diameter, D <sub>i</sub>
	Elements at the left of Iron	Elements with a negative $\epsilon'_H$			
Point	Mn Cr V	Ni	(0 083)	Most probably reversible	A few interatomic spacings
		Mn	(0 09)		
		Cr	(0 10)		
		V	(0 16)		
	Ti	Ce	(0 16)	Reversible	
		Nb	(0 16)		
		(vacancy)	(0 27)		
Sc	O	(0 71)	Getting more irreversible		
Ca	Ta	(0 98)			
K	Ia Nd	(0 98) (1 34)			
Linear	Dislocations		0 31 0 25 (average values)	Reversible Reversible	3 nm for an edge dislocation
	Intersection of three grain boundaries			Depends on coherency	
Planar or bimimensional	Particle/matrix interfaces TiC(incoherent) Fe <sub>3</sub> C MnS		0 98 0 8-0 98	Irreversible , gets more reversible as the particle is more coherent	Diameter of the particle or a little more as coherency increases
	Grain boundaries		0 27  Average Value 0 55-0 61 (high angle)	Reversible  Reversible or Irreversible	
	Twins			Reversible	
	Internal Surfaces				
Volume	Voids		>0 22		Dimension of the defect
	Cracks				
	Particles			Depends on the exothermicity of the dissolution of H by the particles	

Hydrogen concentration in the alloy is a function of the fugacity or the approximate concentration of hydrogen at the surface exposed to the environment. Therefore, hydrogen embrittlement will be controlled by the hydrogen gas pressure or pH of the environment as well as constituents within the environment that may accelerate or inhibit the entry of hydrogen into the alloy. Elements such as sulfur, phosphorus, antimony, tin, and arsenic and their compounds have been found to inhibit the hydrogen recombination reaction in aqueous solutions, thus increasing the charging of atomic hydrogen into the alloy. In contrast, small

amounts of oxygen in gaseous hydrogen environments have demonstrated an inhibitive effect on crack growth of high-strength steels subject to hydrogen cracking.

Temperature also plays an important role in the hydrogen embrittlement of ferrous alloys. Embrittlement is most severe near room temperature and becomes less severe or nonexistent at higher or lower temperatures. At lower temperatures, the diffusivity of hydrogen is too sluggish to fill sufficient traps, but at high temperatures, hydrogen mobility is enhanced and trapping is diminished. Embrittlement is also strongly strain rate dependent. At high strain rates, fracture may proceed without the assistance of hydrogen because the mobility of hydrogen is not sufficient to maintain a hydrogen atmosphere around moving dislocations.

Fracture of low-strength steels in hydrogen environments may be characterized by ductile dimple-rupture, tearing, cleavage, quasi-cleavage, and, less frequently under certain conditions, intergranular cracking.

High-strength steels are prone to fracture either in an intergranular fashion or by quasi-cleavage, depending on the stress intensity [74]. These steels commonly display an incubation time before fracture initiates under sustained loading, usually in association with regions of high-stress triaxiality. Because triaxial stresses are created at notch roots or under plane strain, fracture initiates internally in the steel. Intergranular fracture is promoted by the presence of impurity elements at prior austenite or ferrite grain boundaries. Elements such as phosphorus, sulfur, tin, antimony and arsenic have been found to enhance the intergranular fracture of high-strength steels in hydrogen, and as expected, temper-embrittled steels are even more susceptible to hydrogen stress cracking than steels that are not embrittled.

Nickel and its alloys are susceptible to hydrogen damage in both aqueous and gaseous hydrogen environments. The same factors that affect hydrogen embrittlement susceptibility in ferrous alloys are also prevalent in nickel alloys, although to a lesser degree. In general, fcc metals, because of their greater ease of slip and reduced solute diffusivities as compared to bcc materials, are less susceptible to hydrogen damage. As with ferrous alloys, hydrogen in nickel and its alloys may introduce intergranular, transgranular or quasi-cleavage cracking, and although the macroscopic features appear to be brittle, on a microscopic scale there is a high degree of local plasticity, suggesting that hydrogen enhances flow at the crack tip.

### ***Hydrogen damage in Al alloys***

Only recently has it been determined that hydrogen embrittles aluminum. For many years all environmental cracking of aluminum and its alloys was represented as SCC. However, testing in specific hydrogen environments has revealed the susceptibility of aluminum to hydrogen damage. Hydrogen damage in aluminum alloys may take the form of intergranular [75] or transgranular cracking or blistering. Blistering is most often associated with the melting or heat treatment of aluminum, where reaction with water vapor produces hydrogen. Blistering due to hydrogen is frequently associated with grain-boundary precipitates or the formation of small voids. Blister formation in aluminum is different from that in ferrous alloys in that it is more common to form a multitude of near-surface voids that coalesce to produce a large blister.

In a manner similar to the mechanism in iron-based alloys, hydrogen diffuses into the aluminum lattice and collects at internal defects. This occurs most frequently during annealing or solution treating in air furnaces prior to age hardening [76].

Dry hydrogen gas is not detrimental to aluminum alloys; however, with the addition of water vapor, subcritical crack growth increases dramatically. The threshold stress intensity for cracking of aluminum also decreases significantly in the presence of humid hydrogen gas at ambient temperature [77].

Crack growth in aluminum in hydrogen is also a function of hydrogen permeability, as in the iron- and nickel-base alloys. Hydrogen permeation and the crack growth rate are a function of potential, increasing with more negative potentials, as expected for hydrogen embrittlement behavior. Similarly, the ductility of aluminum alloys in hydrogen is temperature depended displaying minimum in reduction in area below 0°C, this is similar to other fcc alloys. Most of the work on hydrogen embrittlement of aluminum has been on the 7xxx alloys; therefore, the full extent of hydrogen damage in aluminum alloys has not been determined and the mechanisms have not been established. Some evidence for a metastable aluminum hydride has been found that would explain the brittle intergranular fracture of aluminum-zinc-magnesium alloys in water vapor. However, the instability of the hydride is such that it has been difficult to evaluate. Another explanation for the intergranular fracture of these alloys is that there is preferential decohesion of grain boundaries containing segregated magnesium. Overaging of these alloys increases their resistance to hydrogen embrittlement in much the same way as for highly tempered martensitic steels. Regarding corrosion-induced material embrittlement, Pantelakis et al. [11, 78] claimed that hydrogen embrittlement could be responsible for the dramatic degradation of toughness and ductility of 2091 and 8090 Al-Li alloys as well as conventional 2024 alloy in several types of accelerated corrosion tests [13]. In other alloy systems there is mounting evidence connecting embrittlement and stress corrosion cracking to hydrogen penetration. Speidel [8] reviews recent results, mainly for Al-Mg-Zn alloys. Studies by Scamans et al. [79] of Al embrittlement in humid air, point to the major role of hydrogen. In particular, the intergranular crack path and the reversibility of the phenomenon (recovery of ductility after degassing) support a hydrogen, rather than an anodic dissolution, mechanism. Also, Scamans and Tuck [80] measured H<sub>2</sub> permeability and stress corrosion resistance of the Al-Mg-Zn alloy, as functions of quench- rate and aging treatment, and found similar trends. However, the stress-corrosion-resistant Al-Mg-Si alloy does not allow hydrogen permeation through its matrix, though the volume of hydrogen produced by surface reaction with the water in humid air is even higher than that of the Al-Ni-Zn alloy [80]. It has been suggested [8] that hydrogen plays a major role in stress corrosion cracking of aluminum alloys exposed to aqueous solutions as well. An indication in favor of this argument is provided by measurement, in Al-Mg-Zn alloys, of hydrogen permeation and stress corrosion crack growth rates [81]. These parameters are found to vary similarly as functions of the electrode potential. Despite the lack of a universally accepted hydrogen embrittlement mechanism, a generally recognized common feature is that some critical concentration of hydrogen must buildup at potential crack sites, for failure to initiate. Thus, the distribution of hydrogen inside the metal and its pattern of migration are of paramount importance in understanding the phenomena and designing alloys with improved behavior.

It has been shown [82, 83] that lattice defects (vacancies, dislocations, grain boundaries) and precipitates provide a variety of trapping sites for diffusing hydrogen. Hydrogen traps have mechanistically been classified by Pressouyre [63] as reversible and irreversible, depending on the steepness of the energy barrier needed to be overcome by hydrogen to escape from the trap. For example, during a degassing experiment reversible traps will release hydrogen continuously, while irreversible ones will do so only after a critical temperature has been reached. This is the temperature at which the probability of a single jump out of the steep trap becomes nonnegligible. Reversible and irreversible traps may play different roles during an actual experiment [64]. In particular, irreversible traps will always act as sinks for hydrogen, whereas reversible traps may act as sinks or sources depending on initial hydrogen charging of the lattice. A uniform distribution of irreversible traps is believed to provide a beneficial effect in alloy behavior under embrittling conditions, by arresting diffusing hydrogen and thus delaying its buildup at the crack sites [61, 84]. When crack nucleation and growth is along the grain boundaries, boundary chemistry may be

playing an important role. Various studies on Al-Mg-Zn alloys have indicated that alloying elements (and in particular Mg) are segregated on the grain boundary. Tuck [85] proposed that Mg hydride forms at grain boundaries and is responsible for material embrittlement. In an effort to explain the connection between Mg-H interaction and material embrittlement, Song et al. [86] recently showed that stress corrosion and fatigue crack growth rates increase with the concentration of solid solution Mg on grain boundaries. The same authors theoretically calculated a decrease in the intergranular fracture work with both Mg and H segregation. Other aluminium alloys that have been studied for hydrogen induced failure are 8090 [87, 88] and 7050 [86].

Useful insight in the nature and intensity of hydrogen traps can be offered by studying the temperature needed to break these bonds. Thus, thermal analysis techniques have been used for a variety of alloys [65, 85]. In particular, thermal desorption has been successfully used to study hydrogen partitioning in pure cast aluminum and in Al-Cu and Al-Mg<sub>2</sub>Si alloys [83] and hydrogen diffusion in Al-Li alloys. Among other findings, these studies show that, for aluminum alloys, the energy of chemisorption is lower than the energy for lattice diffusion. Thus, the layer of passive oxide-formed on the surface of aluminum alloys-does not mask the bulk trapping states, and the results of thermal analysis are meaningful. Accelerated corrosion tests were recently used by Haidemenopoulos et al. [89] to characterize corrosion and hydrogen absorption in the less studied but widely used Al-Cu alloy 2024. In [90] hydrogen evolution from the corroded specimen of Al alloy 2024 was systematically measured as a function of temperature. The exfoliation test [49] was used as an accelerated corrosion method, and different exposure times were tested. The existence of multiple trapping states was verified and the quantity and evolution pattern of hydrogen is discussed.

# Chapter 3 - Experimental procedures

## 3.1 Materials Studied

As discussed earlier, the main focus of this research was aluminum alloys belonging to the 2xxx alloy series, more accurately, 2024 alloy. The material was obtained in plate form, that had not been anodised and its only surface protection emanated from the thin protective oxide, which is created when the material is exposed to atmospheric air. Material was obtained from several suppliers and with varying thickness (1.8, 2.4 and 3.0mm), as displayed in Table 4. More details about the material are presented in Table 4. The material was identified as being in the T351 condition. Aluminum alloy 2024 Al-clad was also used in some of the experiments in order to have comparable results. Alloy 2024 Al-clad is covered on both sides with a very thin layer of 1230 alloy. This process is called cladding and provides cathodic protection to the material.

The chemical composition of these materials is displayed below in Table 5 and below in Table 6 the thermal treatments of the alloys are presented.

Table 4: Thickness of aluminum alloys (Bare: only natural oxide, Alclad: alloy 1230).

Material	Thickness	Supplier
<b>2024 Bare</b>	1,6 mm	Airbus
<b>2024 Al-clad</b>	1,8 mm	Airbus
<b>2024 Bare</b>	2,4 mm	EAB
<b>2024 Bare</b>	3,0 mm	Airbus
<b>6013 Bare</b>	1,6 mm	Airbus

Table 5: Chemical composition of alloys of aluminum (%wt.).

Sample	Si	Fe	Cu	Mn	Mg	Cr	Zn	Ti
<b>2024</b>	0,50%	0,50%	4,35%	0,64%	1,5%	0,10%	0,25%	0,15%
<b>6013</b>	0,25%	0,50%	0,9%	0,35%	0,95%	-	-	0,10%
<b>1230</b>	0,30%	0,4%	0,1%	0,05%	0,05%	-	0,10%	0,03%

Table 6: Thermal treatments of aluminum alloys.

Material	Temperature Dissolution	Quenching	Cold rolling	Temperature precipitation	Thermal treatment
2024 Bare	495 °C	0°C	Yes	25°C (2 days)	T3
2024 Al-clad	495 °C	0°C	Yes	25°C (2 days)	T3
2024 Bare	495 °C	0°C	Yes	25°C (2 days)	T3
6013 Bare	570°C	0°C	-	190 °C (4 days)	T6

The labeling scheme used to identify the orientations and planes of the alloys is shown in Fig. 3. 1.

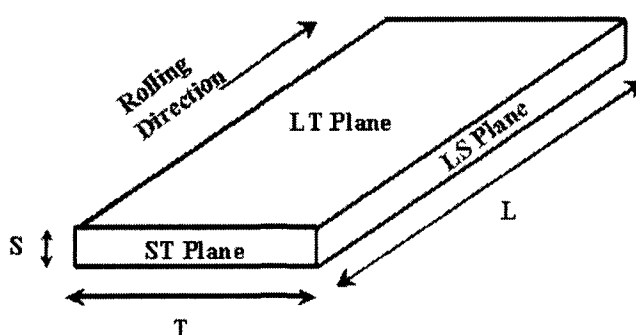


Fig. 3. 1: Labelling scheme used for directions and planes.

## 3.2 Accelerated corrosion testing

Accelerated corrosion testing that provides a useful simulation of the exfoliation behavior of these alloys in various types of outdoor service, especially in marine and industrial environments, was employed. The accelerated corrosion test (EXCO) is described in ASTM specification G34-90 [49]. It includes exposure at 22°C, for 24 hours in a solution containing 234g NaCl, 50g KNO<sub>3</sub> and 6,3ml concentrated HNO<sub>3</sub> (70%wt) diluted to 1 L of distilled water. The quantity of solution used is proportional to the specimen external surface area, with the minimum amount required being 10 ml for every cm<sup>2</sup> of specimen surface and the maximum 30ml.

Exposure took place in a thermostatic air-bath, with the temperature kept constant at 22±0.5°C. Specimen cleaning, after removal from the corrosive solution involved soaking in concentrated HNO<sub>3</sub> (70%wt) for 5 minutes, rinsing in distilled water, then in acetone and thoroughly drying in a purge of warm air. The entire cleaning process did not exceed 10 minutes.

## 3.3 Microstructural characterization of corrosion

### *Preparation of specimens-Metallography*

All specimens were prepared using classical metallographic techniques. The non-corroded specimens were cut from the plate of the corresponding material with the use of a microtom (Struers Accutom). Their size was roughly 0,5 x 1cm<sup>2</sup>. The specimens used for the

corrosion study were cut from various regions of the plate. Regions were selected from the centre and the edges of the plate so as to have a better statistical depiction of the corroded surface. Then the specimens were placed in epoxy resin for easy handling. The surface planes under observation were the rolling surface and the side surface (LT and LS plane in Fig. 3. 1). The specimens for metallographic observation were placed in simple epoxy resin (Acryfix) that stabilizes in atmospheric temperature (20-25<sup>0</sup>C) in roughly 10 minutes, while the corroded specimens were placed in a resin that stabilizes under vacuum (vacuum impregnation). The resin fills the pores, voids and surface abnormalities of the specimen. This process is essential for the maintenance of pits and microcracks during the next steps of preparation.

Next the specimens were initially grinded on SiC abrasive wheels. The sizes of grains were 180, 320, 800 and 1000 grid. Polishing of the specimens followed on special disks with diamond paste of 3 $\mu$ m and 1 $\mu$ m grain size respectively. The last stage of preparation was polishing with Al<sub>2</sub>O<sub>3</sub> particles of 0,5 $\mu$ m diameter for about two hours. Finally the surface was chemically etched with Keller's reagent. This reagent has a chemical composition of: 2,5 ml HNO<sub>3</sub>, 1,5 ml HCl, 1,0 ml HF and 95,0 ml H<sub>2</sub>O. The time of exposure in Keller's was a few minutes. Finally the specimens were washed with distilled water and alcohol and dried in a purge of warm air [91].

### ***Atomic Force Microscopy (AFM) of Corroded Specimens***

Use of AFM (Atomic Force Microscopy) constitutes the most modern methodology for the study of surfaces of all types of materials (metals, ceramics, and complex materials). It provides the possibility of studying surfaces with dimensions up to 1mm x 1mm, with magnifications of their topographic configuration up to x300.000. The acquisition of three-dimensional images of the examined surfaces is possible with the help of a computer.

The AFM senses repulsive contact forces between a fixed flexible microcantilever and the surface of the sample. The Z motion of a silicon nitride tip is monitored in height mode by mounting the sample on an X-Y-Z piezoelectric tube scanner. The tip of the sensor is placed on an isolated cantilever, which has a low spring constant (~0.1-1 N/m) and diverts as a reaction to the forces exercised between the tip of the cantilever and the specimen. The AFM microscope uses the technique of beam laser reflection for the control of force. As AFM allows the depiction of conductible and not conductible surfaces directly in laboratory atmosphere, the preparation of surfaces is a relatively easy work. For the revelation of very small particles however sometimes the chemical attack and the polishing of surfaces is essential, so the surface that will be prepared is level enough so that it reduces the particles (the medium roughness of the surface should be smaller than the length or the width of particles). The roughness can be determined easily from the AFM depictions. AFM topographies were acquired with a Topometrix Explorer Atomic Force Microscope, equipped with a hardware-linearized 100 $\mu$ m, x, y-scanner (z-range 10 $\mu$ m) or an x, y-scanner 2 $\mu$ m (z-range 0,8 $\mu$ m). Pyramidal tips made of silicon nitride (Topometrix, 1520-00) and silicon (Topometrix, 1660-00) was used in the non-contact mode. Different areas of every specimen were scanned (10 to 15 images per specimen were acquired). The images were captured and section analysis data for each image was obtained. These data provided essential information on the surface morphology, i.e. on changes of the surface roughness, accurate measurement of the area and depth of corrosion pits. Changes on the surface of the materials were quantified and recorded according the exposure time to the exfoliation test. Curves of surface data (depth, density and area of pits) were plotted as to the exposure time. Three-dimensional representation of pits and microcracks was possible.

Corrosion was investigated with AFM in order to characterize the early stages of corrosion and cracking. Specimens 50mm wide and 80mm long were cut at right angles to the



rolling direction and were exposed to the exfoliation test, according to the ASTM G34-90 specification. The exfoliation experiments were conducted with specimens exposed to the corrosive solution from 15 min up to 4 hours. After the corrosion process specimens were cleaned and surface topography recorded. For AFM investigations a  $1\text{cm}^2$  large piece was cut from the same position in the centre of the sample and glued on the sample holder. In order to obtain statistically relevant information accounting also for large scale inhomogeneities in the initial surface morphology and in the etching behaviour, the macroscopic location on the 2024 sample chosen for imaging was systematically varied. Typically, on each sample 10-20 AFM images of different sizes were recorded at 2 or 3 different locations, separated by lateral distances of several hundred micrometers.

After polishing follows the chemical attack with Keller's reagent as it has already been described in Chapter 3. AFM is a very environmentally sensitive technique. Certain problems arose during specimen imaging following chemical attack. First of all chemical attack with Keller's reagent is in all respect a corrosion process, which leads to massive corrosion products deposited on specimen surface. These products form a very thin film that makes it impossible for the AFM tip to approach the surface. This layer should be removed so the following steps were taken. The specimen was repolished, attacked for a second time with Keller's [91] and polished in the last stage with  $0,05\mu\text{m}$   $\text{Al}_2\text{O}_3$  in water. Finally the specimen was rinsed with Nital 1% (1%  $\text{HNO}_3$  in alcohol) and dried.

### ***Scanning Electron Microscopy (SEM)***

Fractographic analysis was performed to tensile specimens provided by tests performed in the University of Patras<sup>1</sup>. Fractographies were acquired with a Jeol Scanning Electron Microscope in the secondary electron mode with an accelerating voltage of 25 KV. The scope of this work was to investigate fracture surface appearance in order to determine the crack initiation site as well as the mode of fracture. As both corroded and uncorroded specimens with different tempers were examined the difference in mode of fracture was correlated with corrosion, microstructure and heat treatment.

The outcome of the fractographic analysis was also combined with the hydrogen content measurements and the degradation of the mechanical properties (especially ductility) and provided evidence of possible hydrogen embrittlement.

Following exposure in the corrosive environment described above, the corroded tensile specimens were subjected to tensile testing. The test series performed included: (i) tensile tests on uncorroded specimens to derive the reference tensile behavior of the material, (ii) tensile tests on specimens subjected to accelerated corrosion tests, (iii) tensile tests on specimens exposed to the corrosive environment for different exposure times to determine the gradual tensile property degradation during corrosion exposure in accelerated laboratory tests as well as in atmospheric(natural) environment, and (iv) tensile tests on specimens subjected to corrosion exposure and then to removal of the corrosion- affected surface layer by machining in order to investigate whether the corrosion-induced tensile property degradation is volumetric. The tensile tests were performed according to ASTM E8m-94a [92] specification. For the tests a 200 KN Zwick universal testing machine and a servohydraulic MTS 250 KN machine were used. The deformation rate was 10 mn-ilmin. The tensile tests were conducted in the University of Partas.

After the tensile tests were conducted the failed specimen were cut and the fracture surface placed in the SEM microscope mention above for examination. The study of the mode of fracture correlated with the corrosion results and the hydrogen measurements will lead to a spherical understanding of hydrogen embrittlement.

---

<sup>1</sup> Tensile and fatigue tests were performed in the University of Patras by Professor Pantelakis and his team.

The preparation of specimens for observation with SEM is divided in two different approaches:

- (a) observation of the corroded surface immediately after corrosion
- (b) observation of the fracture surface of tensile specimens

In the first case immediately after corrosion the specimens were immersed in concentrated nitric acid (70%) for 5 minutes, in order to remove the corrosion products deposited during electrochemical action. Finally they were dried in a purge of warm air. After the surface cleaning from the products of corrosion, the specimens are cut in the suitable size ( $2 \times 2 \text{ cm}^2$ ) in Struers' Accutom, using very low cutting speed. For the observation in SEM it is essential that the conductivity of specimens during observation is ensured, therefore the specimens were affixed on the special specimen holder with graphite paste. Then they are placed in the vacuum chamber of the microscope for the observation.

In the second case after cutting to the appropriate size, fracture samples were placed in a ultrasonic bath of alcohol and water and then dried.

### 3.4 Hydrogen measurements

A main part of this thesis consists of the determination of hydrogen concentration and its trapping states in the material after corrosion. The determination of these states was conducted by using a thermal desorption technique.

The scope of this process was to measure the amount of hydrogen eluting from specimens previously subjected to various periods of exfoliation corrosion exposure as a function of temperature. Strips of the materials, 2.0mm wide and 25 mm long, were cut at right angles to the rolling direction and were exposed to exfoliation corrosion. The large surface to volume ratio of the specimen was chosen with a view to decreasing the hydrogen evolution time and increasing the sensitivity of the measurements. The exfoliation accelerated corrosion test is described in ASTM specification G34-90 as is mentioned above in 3.2. Hydrogen evolved from the corroded specimen with controlled heating in an inert atmosphere and was measured using a gas chromatograph.

For the determination of hydrogen quantity trapped in the material's microstructure an in-house experimental setup was used. This setup consists of a furnace with a system of automatic temperature control, a supply of inert gas (high-purity nitrogen) and a gas chromatograph equipped with a valve for sampling gases as is shown in Fig. 3. 2. The sample was placed in a 10 mm diameter quartz tube and held in place by an inert porous diaphragm, permeable to the gas (quartz wool). The tube was inserted in the furnace and subjected throughout the experiment to a flow of  $Q=20\text{ml/min}$  high purity nitrogen. This flow was then driven to a gas chromatograph equipped with a TCD detector. Calibration runs were performed using standard  $\text{H}_2 - \text{N}_2$  mixtures, of volume concentration 1000 and 10000 ppm. Blind experiments were conducted with an empty tube heated up to  $600^\circ\text{C}$  and no hydrogen was detected. The temperature of furnace was increased at a rate of approximately  $5^\circ\text{C/min}$  and the nitrogen current swept along everything that was emitted by the sample and carried it in the gas chromatograph. The sampling was performed manually through the gas-sampling valve about every 2 minutes.

Primary data consist of curves of the intensity,  $I$ , of TCD detector signal (in  $\mu\text{V}$ ) versus time, combined with the temperature history of the specimen. Detector intensity is converted to hydrogen mass flow rate,  $m$ , by the expression

$$m = \alpha I Q$$

where  $\alpha$  has units of  $\text{g of H}_2 / (\text{ml } \mu\text{V})$ . It is the calibration constant of the detector expressing the mass concentration of hydrogen per  $\mu\text{V}$  indication of the detector. During the present PhD work, a small deterioration of the accuracy of the detector was witness, which was taken into account in the data.

The results reported in the next section are presented as hydrogen mass flow rate (in  $\mu\text{g}/\text{min}$ ) versus specimen temperature. If the heating rate is sufficiently low, each trapping site produces an independent peak. The temperature of the onset of peak growth is characteristic of the energy needed to release hydrogen from the respective trapping site. Thus, low temperature peaks are related to weakly bonded hydrogen and high temperature peaks to strongly bonded hydrogen. Calculation of the total hydrogen quantity in each trapping site is performed by integrating the area under the respective peak.

### 3.5 Microhardness testing

Microhardness testing versus temperature simulating the thermal desorption spectrum of hydrogen trapping was performed. Specimens of dimensions  $5 \times 10 \text{mm}^2$  were cut out of 2024 plate. The small size of the specimen was necessary for the uniform transport of heat into the sample during thermal treatment. Two sets of specimens were fabricated. The first set was corroded in the Exco solution (exfoliation corrosion test), for 24 hours, cleaned according to the ASTM specification mentioned above and placed in the furnace, which was used, for the thermal desorption experiments. The furnace was heated with a rate of  $5^\circ\text{C}/\text{min}$  up to  $550^\circ\text{C}$ . Every  $50^\circ\text{C}$  a specimen was removed from the furnace and quenched in iced water. This heat treatment can be described as escalating solution treatment for the temperatures 50, 100, 150, 200, 250, 300, 350, 400, 450, 500 and  $550^\circ\text{C}$ . After cleaning and grinding of the corroded material, the specimen's microhardness was measured (10 counts per specimen).

The second set of specimens was not corroded. After cutting the specimen were cleaned and submitted to the same thermal treatment as the first set. Then they were cleaned slightly polished and their microhardness measured.

The outcome of this experimental investigation was microhardness profiles as a function of heat treatment temperature. The curves were compared with the corresponding thermal desorption spectrum. Changes in the microhardness profile of the material depict changes in the alloys microstructure, which were caused by the admission of hydrogen into the material. These results are used in conjunction with the thermal desorption curves described above to correlate hydrogen content with changes in microstructural properties.

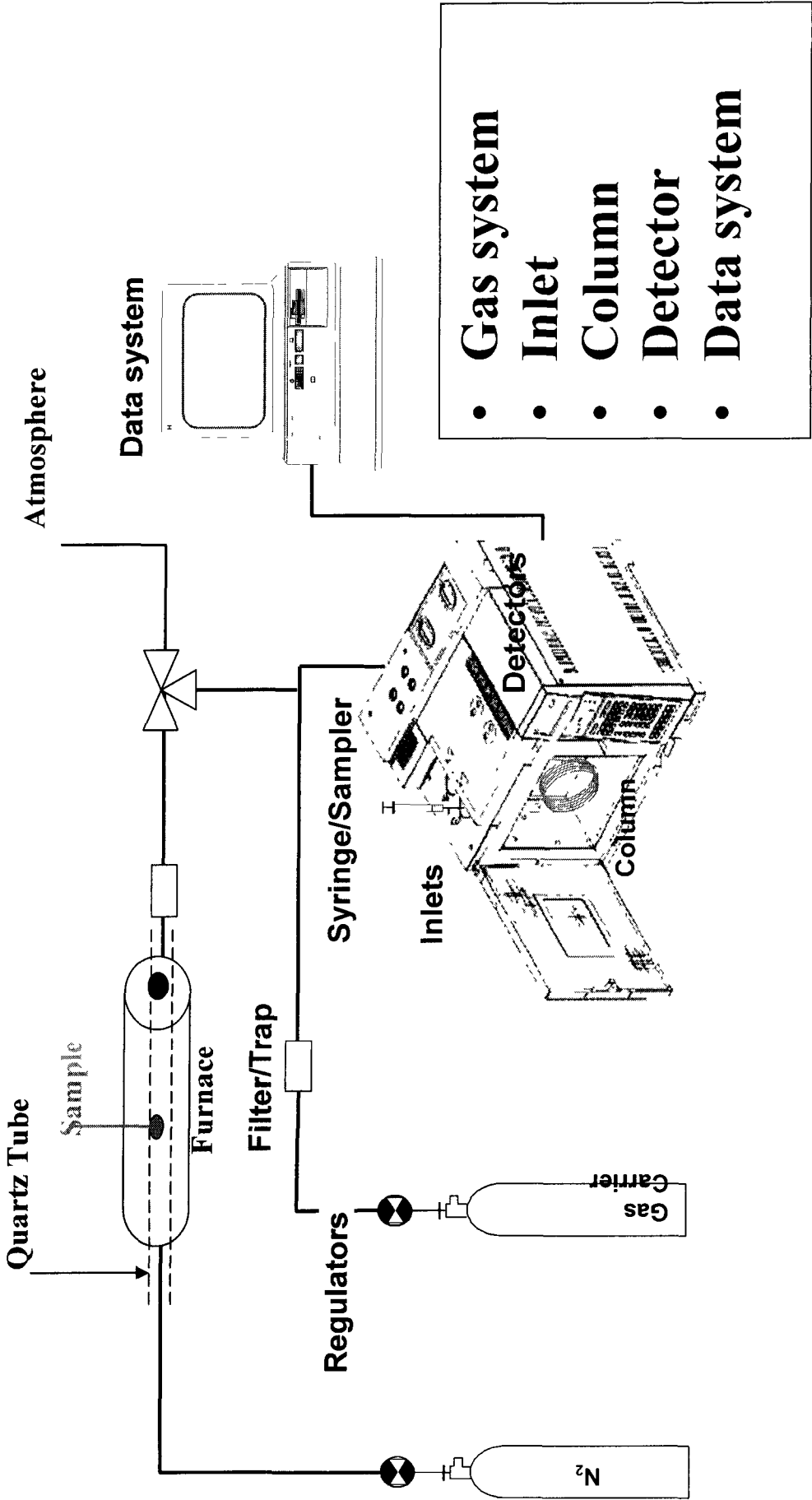


Fig. 3. 2: Gas Chromatography experimental setup.

# Chapter 4 – Corrosion and hydrogen embrittlement

## 4.1 Microstructural Characterization of Corrosion

### *Objective*

The objectives of the microstructural characterization are the following:

- To assess the corrosion damage in terms of pitting, intergranular corrosion, exfoliation and depth of attack
- To determine possible pathways of hydrogen entry in the material during corrosion as well as to investigate potential microstructural sites for hydrogen trapping

As explained in the preceding chapter several optical and electro-optical characterization techniques were used in order to assess the corrosion damage at varying microstructural levels. Surface damage, particularly in the early stages of corrosion, were examined by AFM, while at longer exposure times SEM investigations were employed. Intergranular corrosion, exfoliation attack and hydrogen pathways were assessed with metallographic sectioning. Potential sites for hydrogen trapping were investigated by means of TEM in uncorroded material.

### *Evolution of corrosion damage*

The as-received material is exposed in the EXCO solution, cleaned and examined in the AFM or SEM according to the techniques described in the previous chapter.

It is important to start with the very early stages of corrosion damage in order to determine whether corrosion starts as pitting or uniform corrosion. Atomic Force Microscopy proved to be very helpful due to the high magnification, high resolution and 3D topographic imaging capability, which enabled a more quantitative assessment of corrosion damage.

### *Uncorroded material*

A representative 3D surface topography of uncorroded but metallographically prepared (ground, polished and etched) 2024-T3 is shown in Fig. 4. 1, which depicts the LS plane of the plate in a 100x100 $\mu\text{m}$  scan. The grain structure is made evident by the selective attack of grains (due to different orientation) from the Keller's reagent used for etching. Voids are also present at the grain boundaries or inside the grains. They are formed probably due to the removal of inclusions or second-phase particles during specimen preparation. In order to characterize these voids, a line profiling technique was used. Fig. 4. 2 depicts a 2D image of the surface and the position of two line scans. These scans are presented in Fig. 4. 2a and Fig. 4. 2b respectively. The line scans are obtained by moving the AFM tip selectively over the prescribed path while measurements in the z-direction are possible. The line scan in Fig. 4. 2a is over two voids in the grain interior. The voids have lateral dimensions 8x4 $\mu\text{m}$  and depth of the order of 1 $\mu\text{m}$  (800nm), while they possess a level

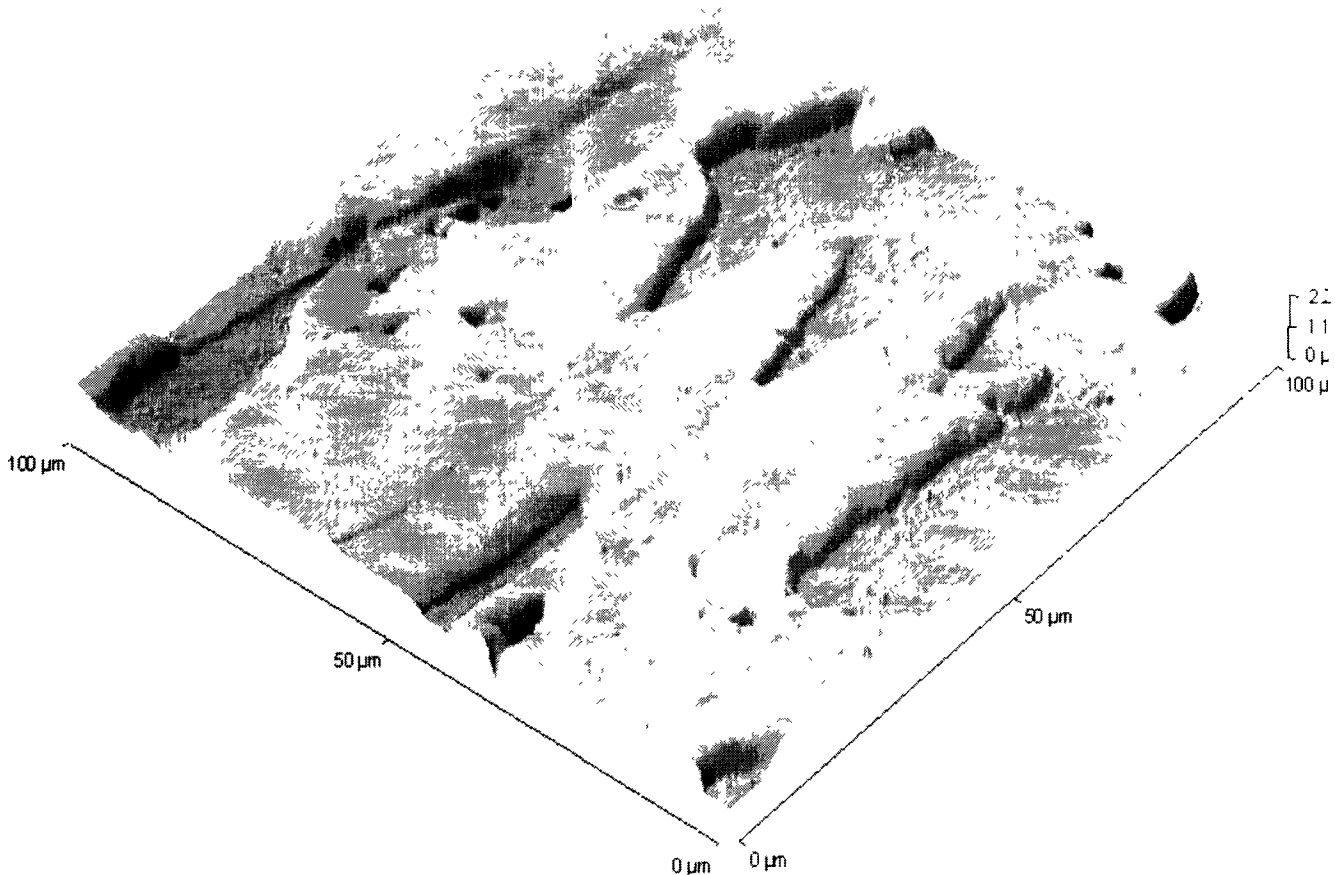


Fig. 4. 1: Tree-dimentional depiction of alloy 2024-T3microstructure (LS plane).

bottom topography. The voids at the grain boundaries (Fig. 4. 2b) are more equiaxed possessing a rhomboidal shape of roughly  $4\mu\text{m}$  lateral dimension with a depth of the order of  $2\mu\text{m}$  ( $1800\text{nm}$ ). Obviously the voids at the grain boundaries belong to particles of different shape and probably composition from those present in the grain interior. These particles would play an important role in the corrosion process as they would act as anodic or cathodic sites, depending on their composition. A representative 3D surface topography of the LT plane (rolling plane) just prior to accelerated corrosion exposure is shown in Fig. 4. 3 for the  $2.4\text{mm}$  thickness material and in Fig. 4. 4 for the  $3\text{mm}$  thickness material. The specimens are in the as-received condition and have been cleaned by acetone. Linear depressions parallel to the rolling direction are present. These depressions can reach a width of  $26\text{-}30\mu\text{m}$  and a depth of  $0.5$  to  $2\mu\text{m}$ . In the interior of the depressions the surface exhibits a ridge-like morphology with an average ridge height of  $100\text{nm}$ . The surface between the depressions is more or less flat. It is believed that the depressions have formed due to the rolling operation. In the  $3\text{mm}$  material (Fig. 4. 4) there is evidence of pitting along the depressions, while corrosion products have been deposited close to the corrosion pits. This leads to an indication that the as-received  $3\text{mm}$  2024-T3 alloy might have been exposed for a long time outdoors, before shipment, and therefore experienced some degree of atmospheric corrosion.

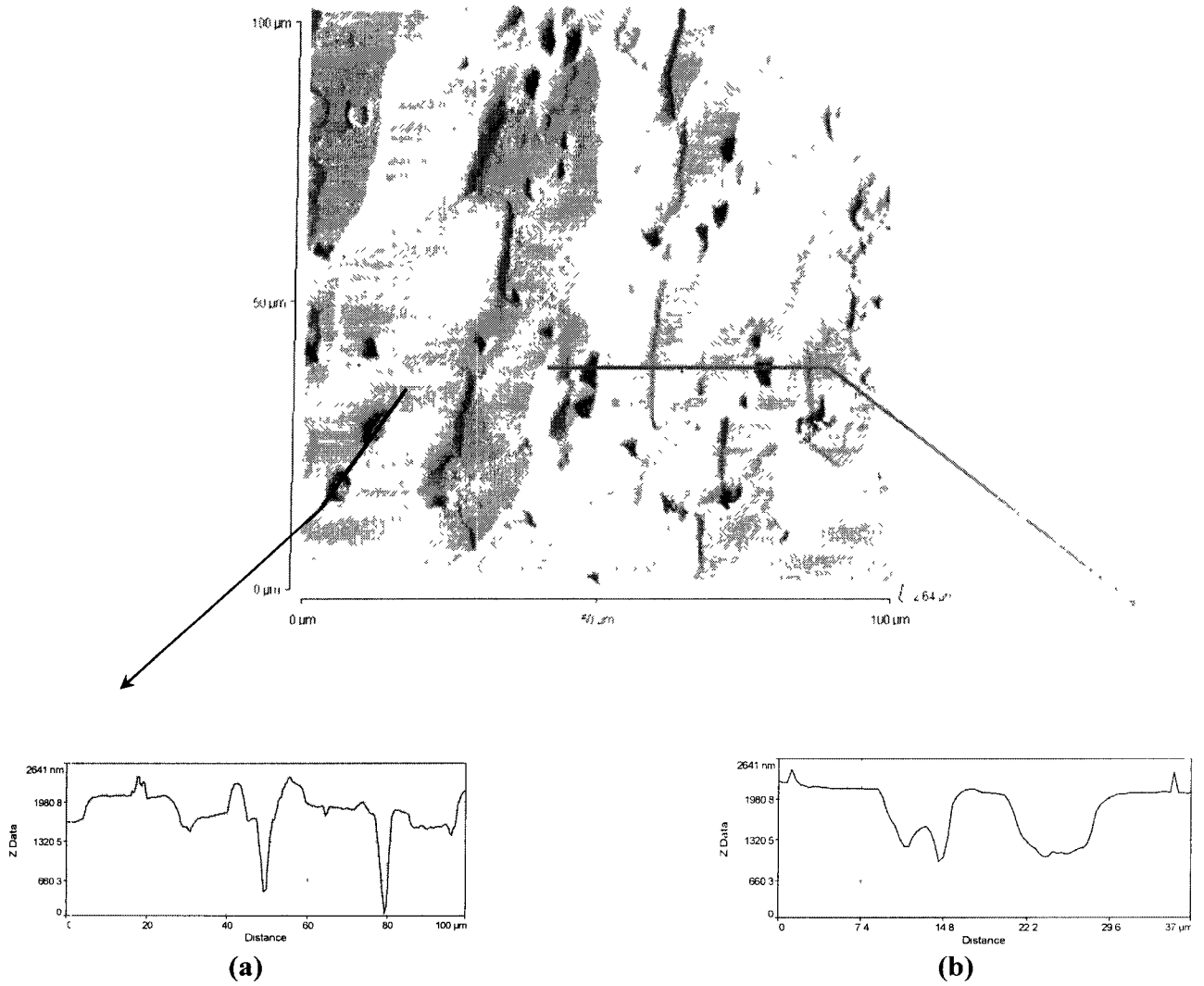


Fig. 4. 2: Two-dimensional depiction of the microstructure of alloy 2024-T3 (LS plane) with line scans.

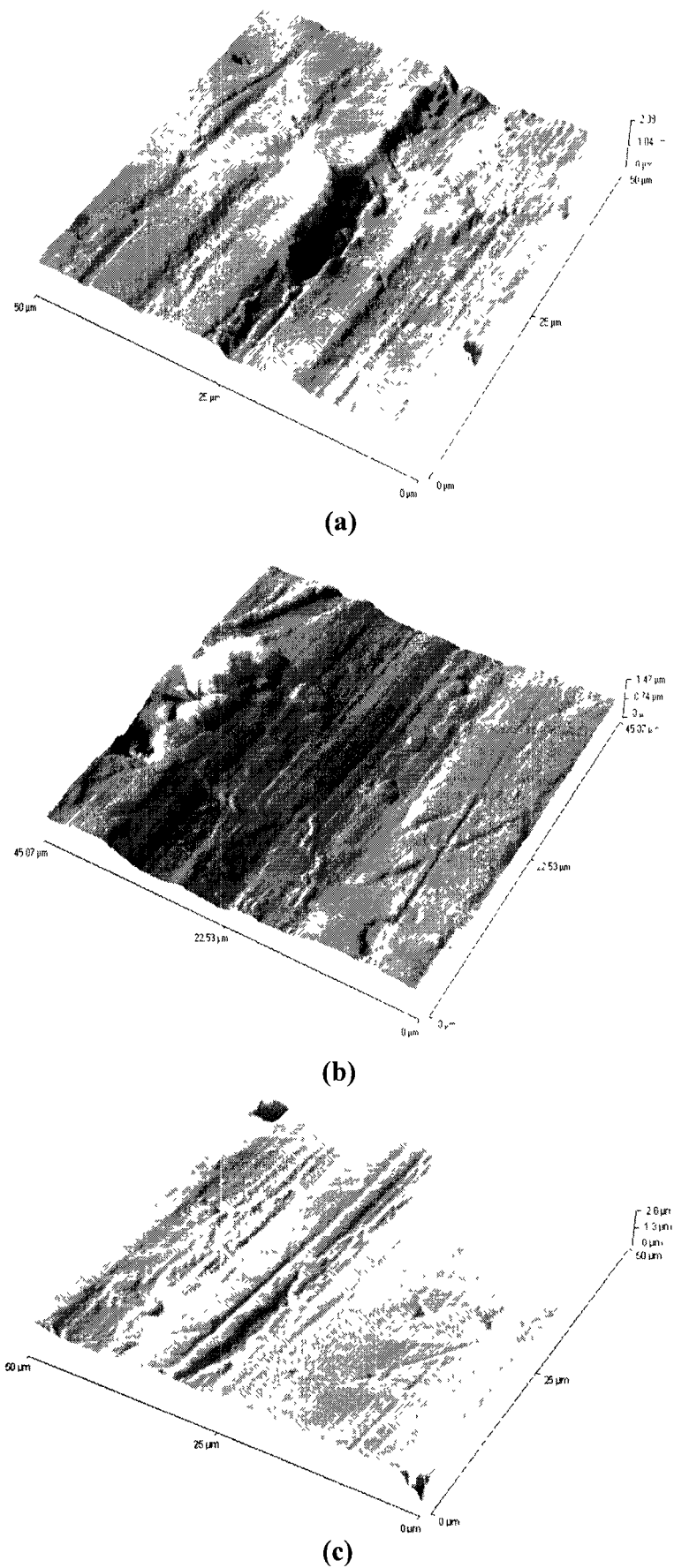


Fig. 4. 3: AFM topographies of as received aluminum alloy 2024 2.4mm LT plane. (a) Through (c).



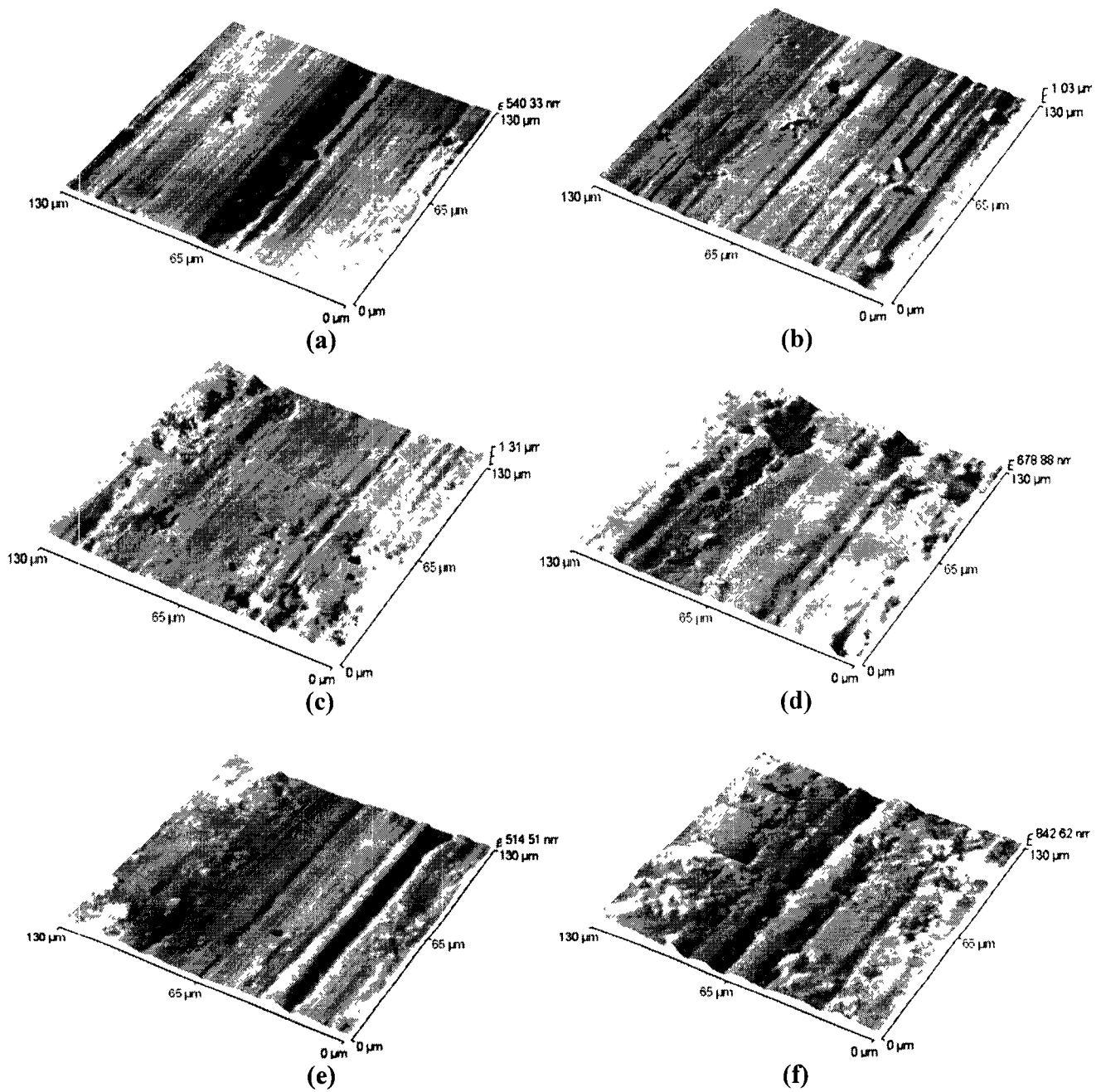


Fig. 4. 4: AFM topographies for the as received aluminum alloy 2024 3mm, LT plane. (a) through (f).

### ***15min EXCO***

The surface after 15 min of EXCO exposure seems quite flat. The surface roughness is low with Ra and RMS being 102 and 126 nm respectively. A characteristic topography is shown in Fig. 4. 5 which depicts the rolling marks in an otherwise flat surface. However certain areas of the surface show the development of a network of surface cracks (Fig. 4. 6b,c). Closer examination revealed that this crack pattern is due to the spalling of the oxide film, which forms on the surface of the alloy. In most cases there are corrosion products close to the surface cracks (Fig. 4. 7a) and in other cases fragmentation of the oxide film has taken place and flakes have been removed (Fig. 4. 7b). The cracks are V-shaped and have a depth of 300nm (Fig. 4. 8 arrow A) The corrosion products form lips along the cracks with a maximum height of 100nm relative to the adjacent flat surface (Fig. 4. 8 arrow B). Examination also revealed the beginning of pitting corrosion (Fig. 4. 8 arrow C). These pits have a depth of 600nm and form mainly at surface crack intersections and triple junctions. So it seems that the corrosion activity starts early, even after only 15min exposure time. It causes cracking and spalling of the surface oxide and initiates the pitting process.

### ***30min EXCO***

After 30 min exposure the rolling marks are still quite clear (Fig. 4. 9b), however the surface roughness has increased to Ra=131 and RMS=179nm (Fig. 4. 9d). Pitting is more pronounced and seems to form on the rolling marks (Fig. 4. 9a) or on other surface defects. Pit density has increased and pit depth ranges from 500 to 800nm (Fig. 4. 9c). Corrosion products, in the form of hills, are deposited throughout the surface.

### ***1hour EXCO***

After 1 hour exposure the rolling marks have almost worn away (Fig. 4. 10) Roughness has increased further to Ra=183 and RMS=250nm. Pitting density has increased and the pits grow deeper. The average pit depth varies from 1 to 2.6 $\mu$ m. A new feature is the grouping of pits, i.e pits that grow close to each other coalesce and form a larger corrosion area. Deposition of corrosion products on the surface has ceased.

### ***2hours EXCO***

After 2 hour exposure, no rolling marks exist on the surface and the roughness has stabilized to Ra=148 and RMS=195nm. New corrosion pits initiate all over the surface. Pit depth has ceased to increase. However pits that formed at earlier times grow in diameter and lose their steepness, while the clustering of pits is enhanced (Fig. 4. 11). A new feature is corrosion along lines that connect pits (Fig. 4. 11c). This is a form of pit-to-pit interaction and leads to the initiation of intergranular corrosion. This argument will be further discussed with the aid of metallographic sections later in this chapter.

### ***4hours EXCO***

After 4 hours exposure the roughness increases again to Ra=207 and RMS=272nm. Pit depth varies from 1 to 3 $\mu$ m. Pit clustering and pit-to-pit interaction (Fig. 4. 12) are again visible, signaling the onset of intergranular corrosion.

The observations from the AFM, regarding the early stages (15min-4h) of corrosion are summarized in Table 7.

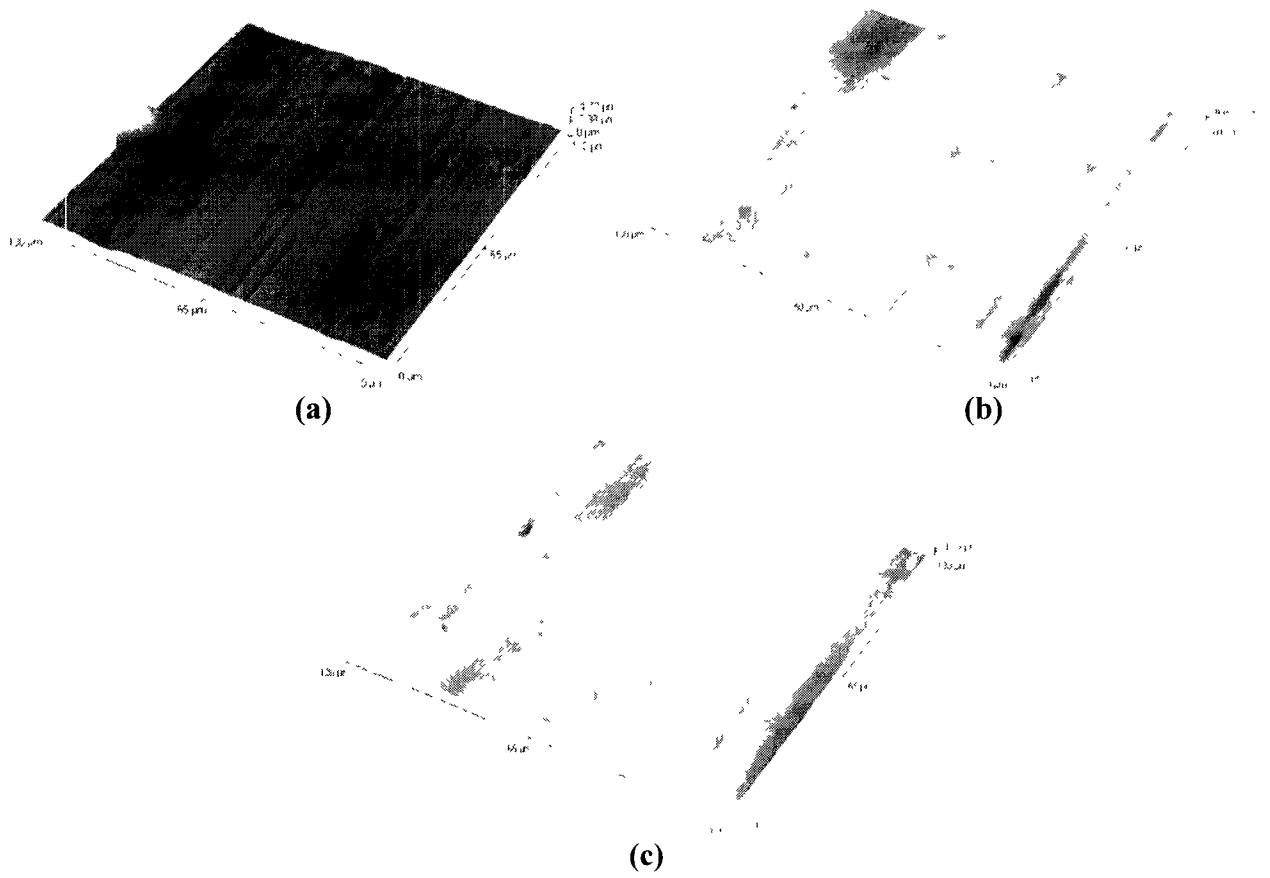


Fig. 4. 5: Alloy 2024-T3 (LT plane), 15min in the corrosive solution exco (Characteristic rolling ridges).

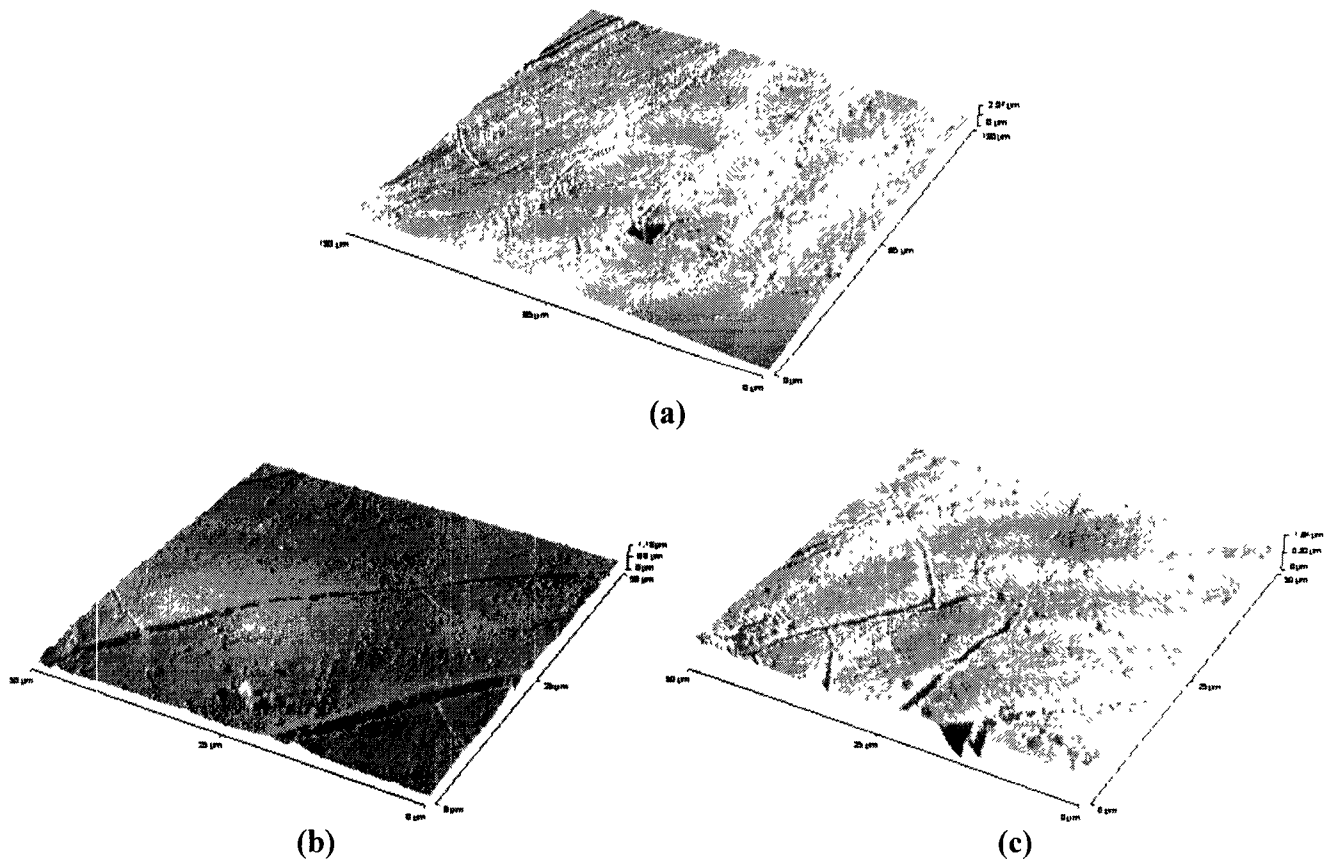


Fig. 4. 6: Alloy 2024-T3 (LT plane), 15min in the corrosive solution EXCO

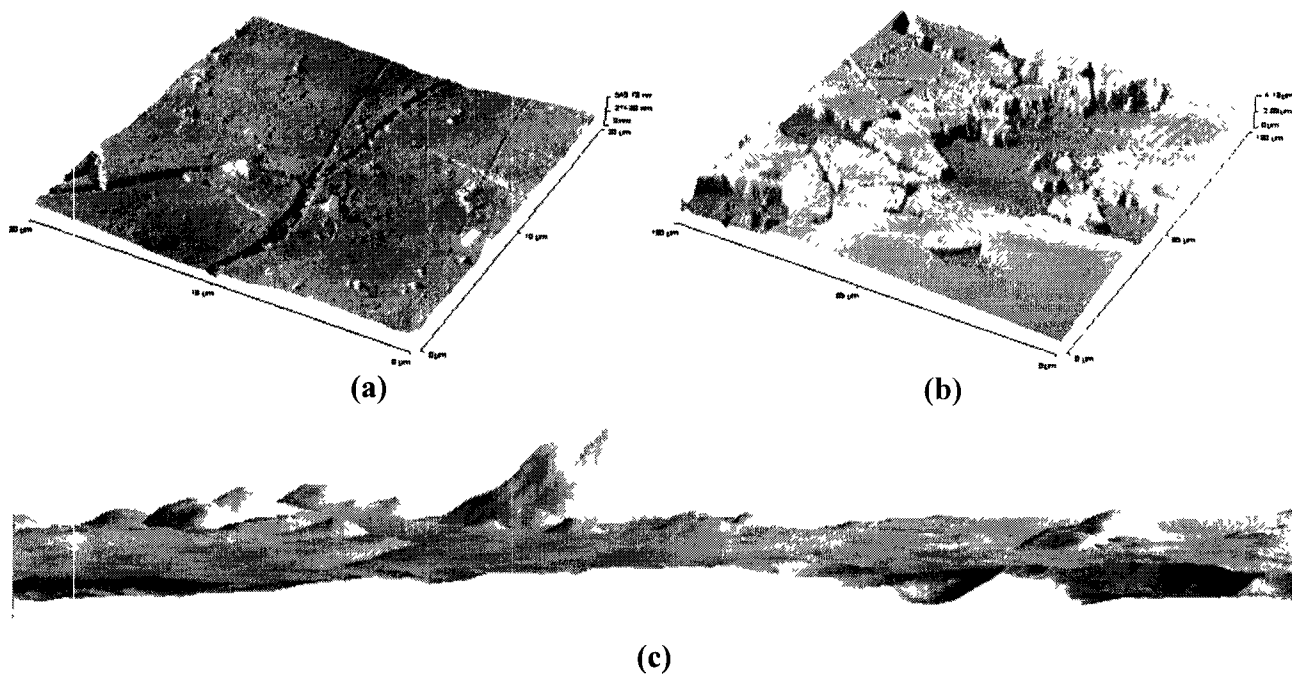


Fig. 4. 7: Alloy 2024-T3 (LT plane), 15min in the corrosive solution EXCO. Fragmentation and spaling of surface oxide.

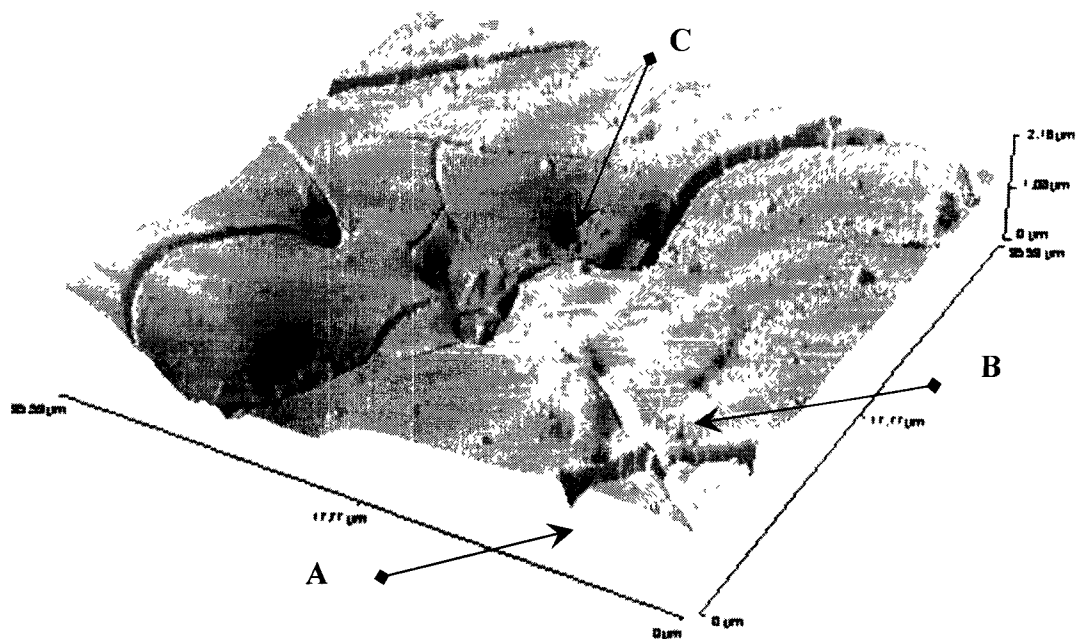


Fig. 4. 8: Alloy 2024-T3 (LT plane), 15min in the corrosive solution EXCO. 3D depiction of corrosion, Initiation of pitting (arrow C) corrosion (50x50μm).

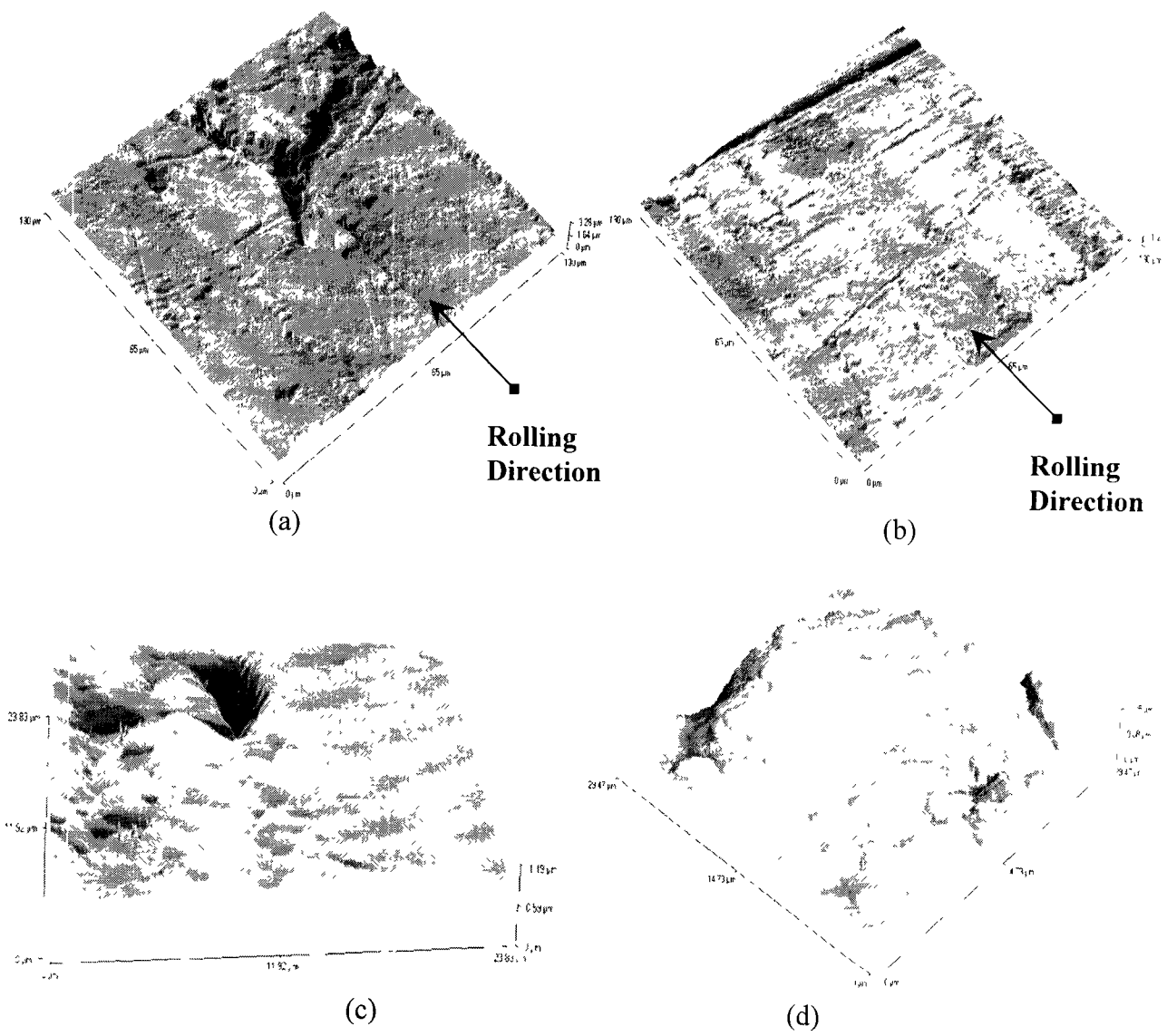


Fig. 4 9: Alloy 2024-T3 (LT plane), 30min in the EXCO solution (a) and (b) different areas (130x130μm), (c) and (d) magnification of previous topographies (30x30μm).

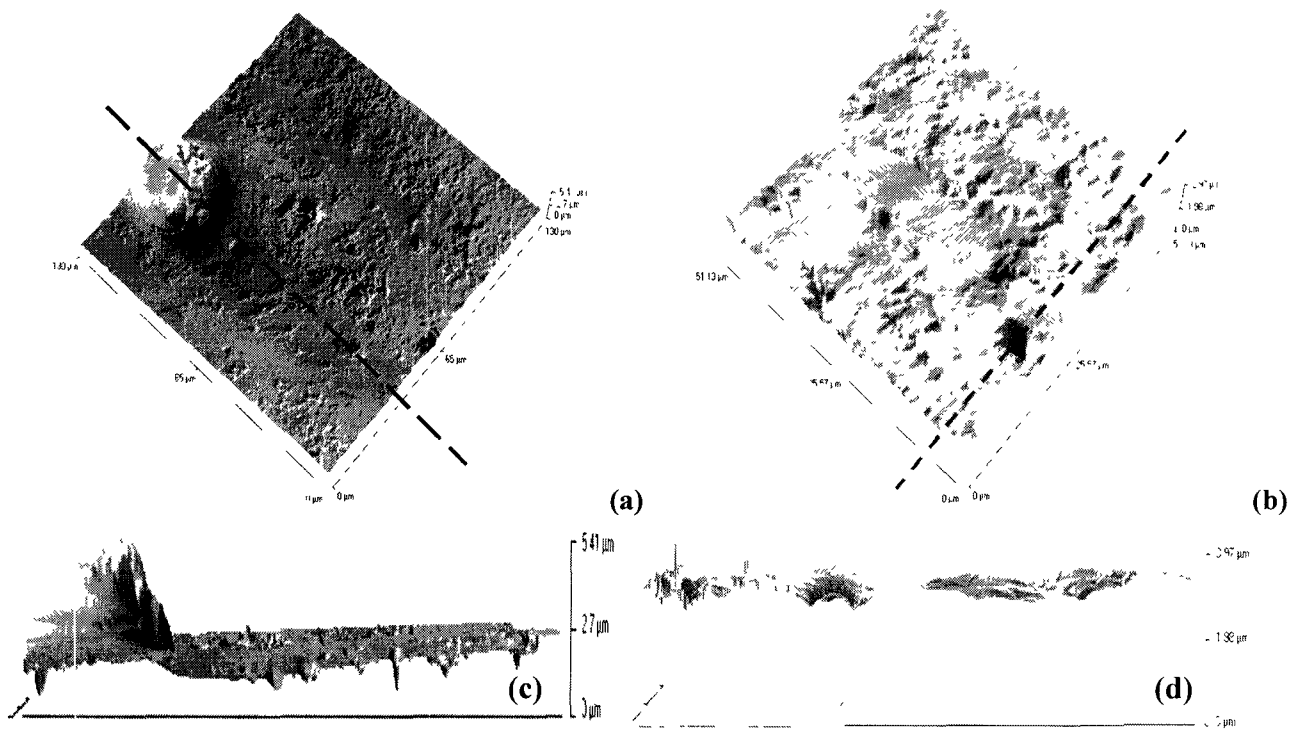


Fig. 4. 10: Alloy 2024-T3 (LT plane), 1hour in the corrosive solution EXCO (a). Three-dimensional magnification of previous picture (b). (c) and (d) are line scans.

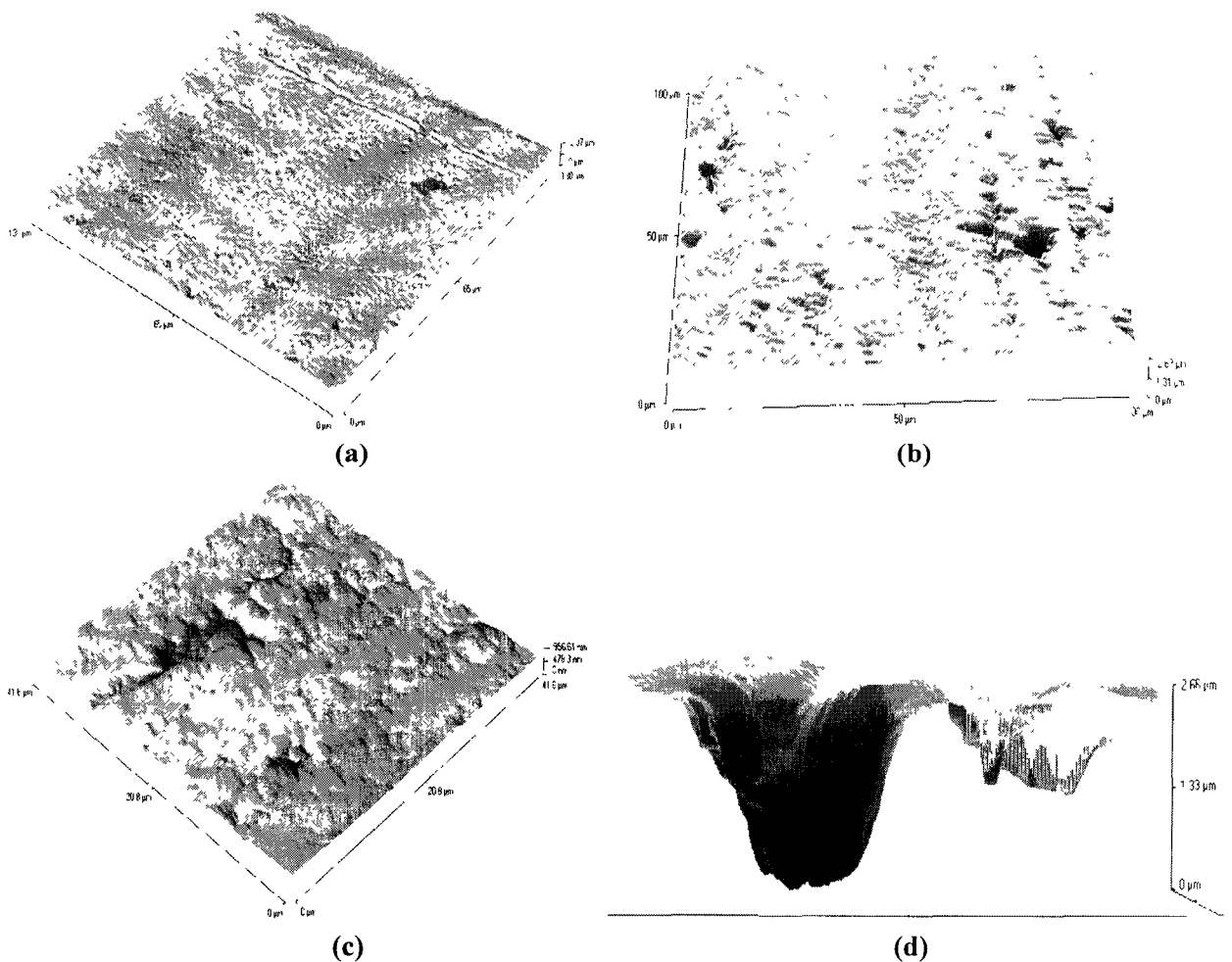


Fig. 4. 11: Alloy 2024-T3 (LT plane), for 2 hours in the corrosive solution EXCO (a), (b), (c) and (d).

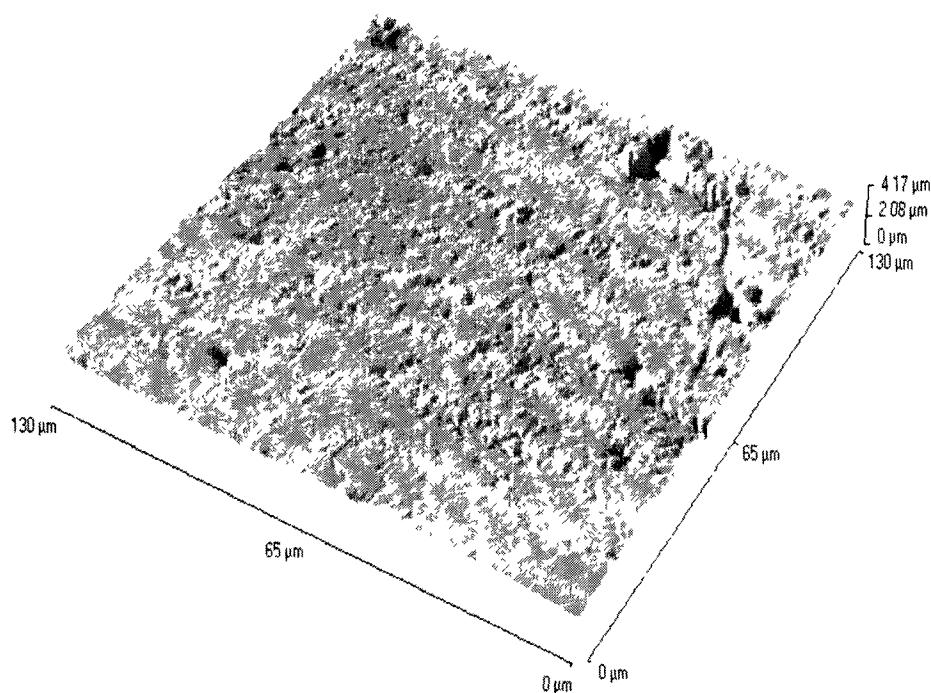


Fig. 4. 12: Alloy 2024-T3 (LT plane), for 4 hours in the corrosive solution EXCO.

AFM was used to assess corrosion damage in the early stages (up to 4 hours) of attack. Beyond that time stereoscopic analysis and SEM were employed. The evolution of corrosion damage with exposure time as observed with the stereo-microscope is depicted in Fig. 4. 13. For 2 and 4h of exposure time the damage observed with the AFM is not resolved with the stereo microscope. Surface damage becomes evident from 8h and beyond. The dark areas in the photos are pit clusters. These clusters grow in size with exposure time and above 48h of exposure cause exfoliation.

Areas of isolated pitting were examined with the SEM. The evolution of pitting with exposure time is shown in Fig. 4. 14 from 8 to 96h exposure time. It is evident that pitting density increases with exposure time. In addition to the general increase of pitting density, other interactions take place as well. Pit-to-pit interaction is evident from 8h of exposure and becomes more intense at higher exposure times (Fig. 4. 15). At high exposure times pit coalescence and secondary pitting within the primary pits develops (for example see Fig. 4. 15 for 36h exposure time).

Table 7: Summary of AFM observations on the early stages of EXCO corrosion.

Exposure time	Pit depth ( $\mu\text{m}$ )	Roughness (nm)		Comments
		Ra	RMS	
Uncorroded				Rolling marks with ridge morphology. Evidence of corrosion in the 3mm material.
15min	0.6-0.8	59	75	Oxide cracking and spalling. Initiation of pitting.
30min	0.5-0.8	131	179	Pit density increases. Pits become deeper and steeper.
1hour	1.0-2.6	183	250	Pits become deeper. Pit clustering.
2hours	1.0-2.6	148	195	Pit broadening. Enhancement of pit clustering. Initiation of pit-to-pit interaction leading to IC corrosion.
4hours	1.0-3.0	207	272	Roughness increase. Pit clustering and enhancement of pit-to-pit interaction.

Metallographic sections were also prepared and examined in order to determine the depth of attack with exposure time. Fig. 4. 16a depicts the corrosion damage for 8h of exposure time. Pitting on the LT (rolling) plane reaches a depth of 0.3mm, however corrosion is more intense in the mid-plane of the LS plane (side surface) as shown in Fig. 4. 16 b. At 12 h of exposure time, corrosion spreads on the LT plane without further penetration in depth (Fig. 4. 17). However this spreading is moving beneath the surface of the material and causes exfoliation of surface layers. The exfoliation process becomes more intense with the increase in exposure time. Fig. 4. 18 shows the corrosion attack after 24h of exposure, where significant material removal has taken place (Fig. 4. 18ab). The subsurface spreading of corrosion damage proceeds with intergranular corrosion as shown in Fig. 4. 18c. Similar corrosion damage development is observed at higher exposure times as shown in Fig. 19, 20, 21 and 22 for 36, 48, 72 and 96h exposure respectively.

The above observations from the AFM, SEM, Stereo-microscope and Metallographic sections lead to conclusions regarding the evolution of corrosion damage with exposure time. Corrosion starts in the form of isolated pits. In the first 4h of exposure pits deepen and grow laterally. Pit density increases and pit-to-pit interaction starts. Pits interact via intergranular corrosion (see for example Fig. 4. 12). This leads to pit coalescence and pit cluster formation. Pit clusters grow laterally beneath the material surface via intergranular corrosion, leading to exfoliation of surface layers of the material. This type of damage evolution, more specifically the intergranular network supporting pit growth is also responsible for the transport of corrosion solution deep in the material, so that the corrosion reaction takes place in a certain depth producing hydrogen. This is one of the main mechanisms of hydrogen transport in relatively high depths, which cannot otherwise be explained solely by diffusion from the material surface. However once hydrogen is produced, e.g. at the bottom of a corrosion pit (for example see Fig. 4. 17c) it diffuses to the adjacent unaffected material and establishes a hydrogen diffusion zone below the corrosion zone

The depth-of-attack is defined as the maximum depth the corrosion front has reached within a certain exposure time. For 24h exposure the depth-of-attack is about 350 $\mu$ m as shown in Fig. 4. 28 and Fig. 4. 29.



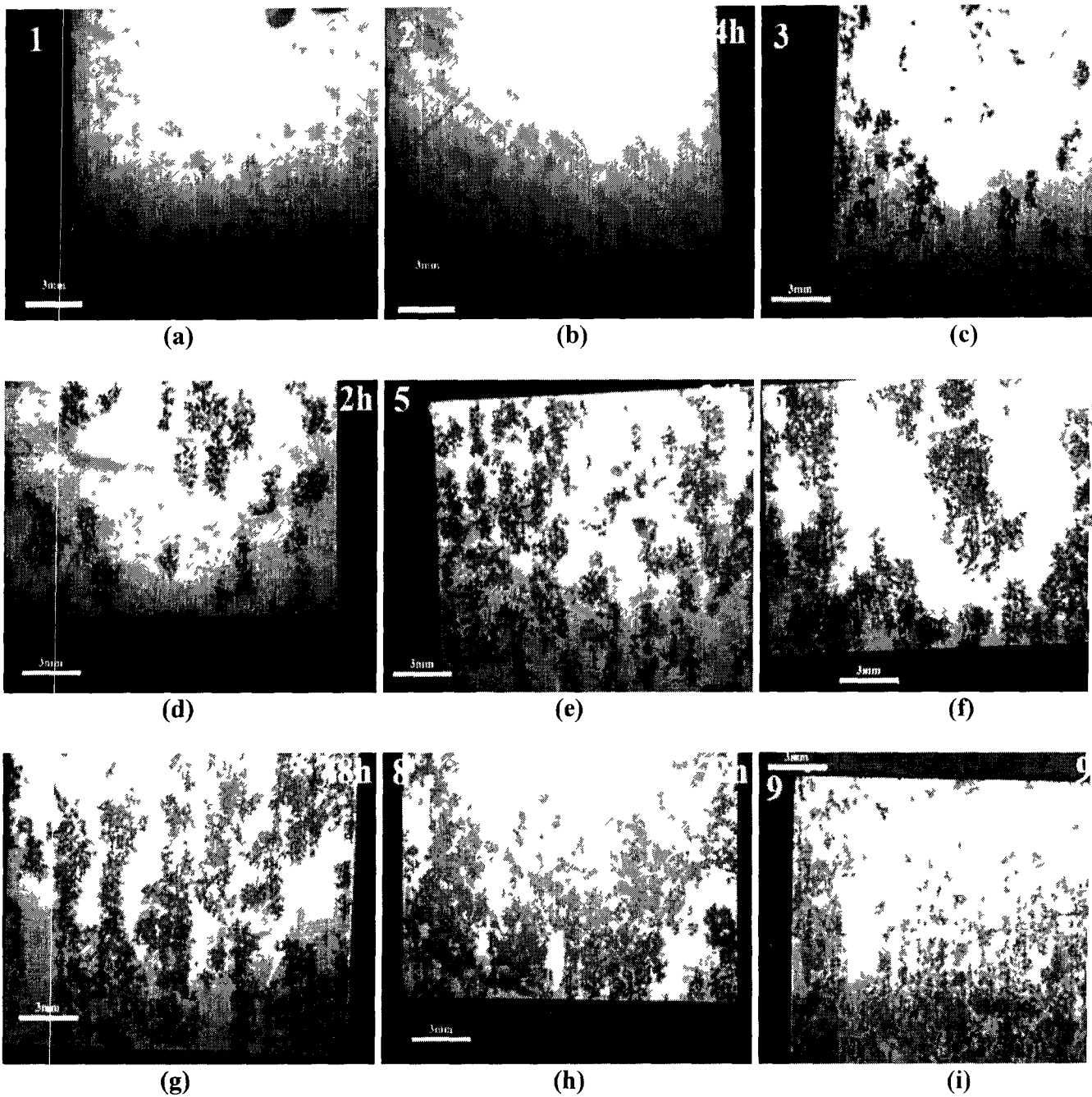


Fig 4 13 Stereo photography of Alloy 2024 (LT plane), exposed in EXCO for 2 to 96 hours (details in the text,

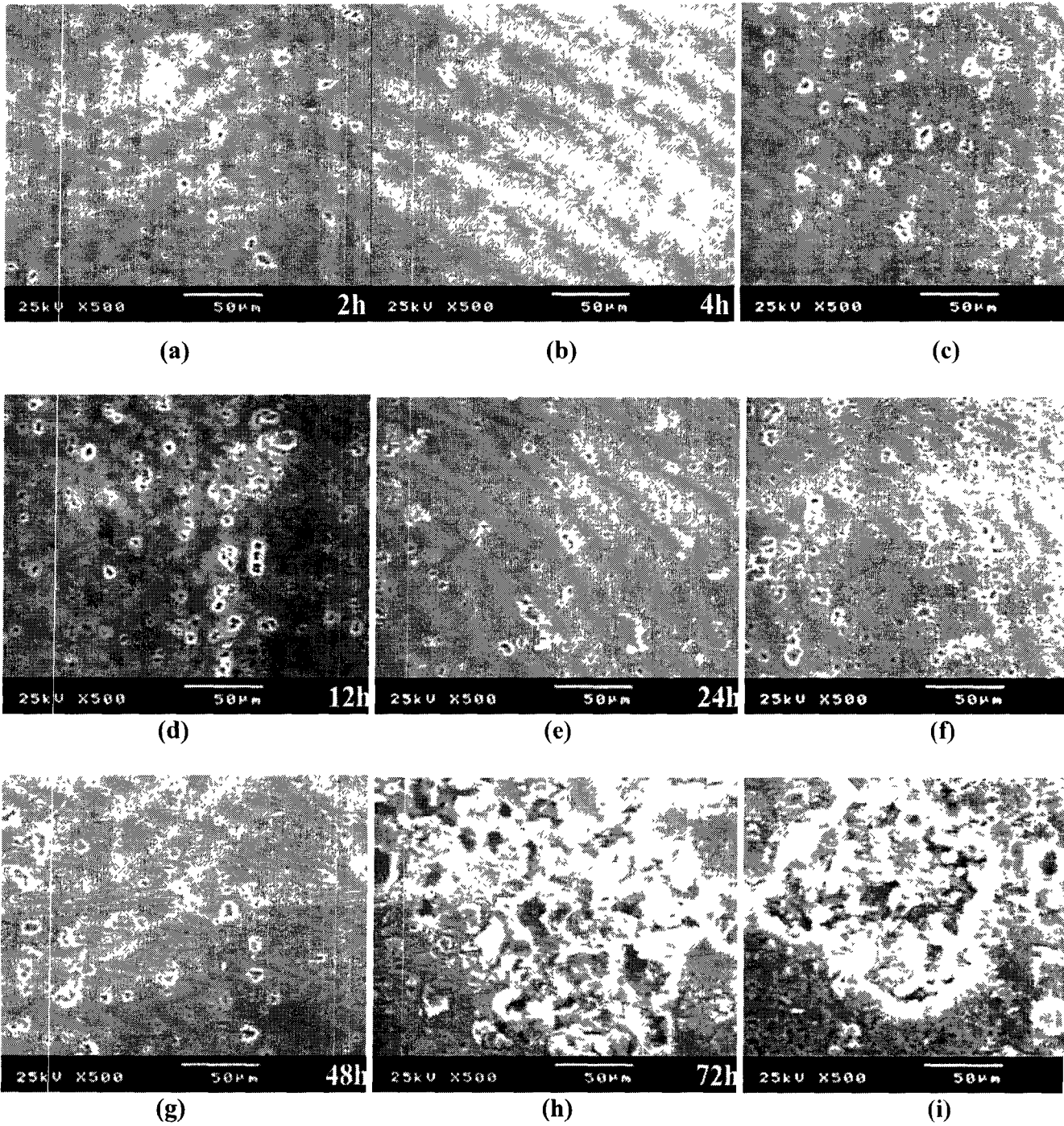


Fig. 4. 14: SEM topographies of Alloy 2024 (LT plane), exposed in EXCO for 2 to 96 hours (details in the text).

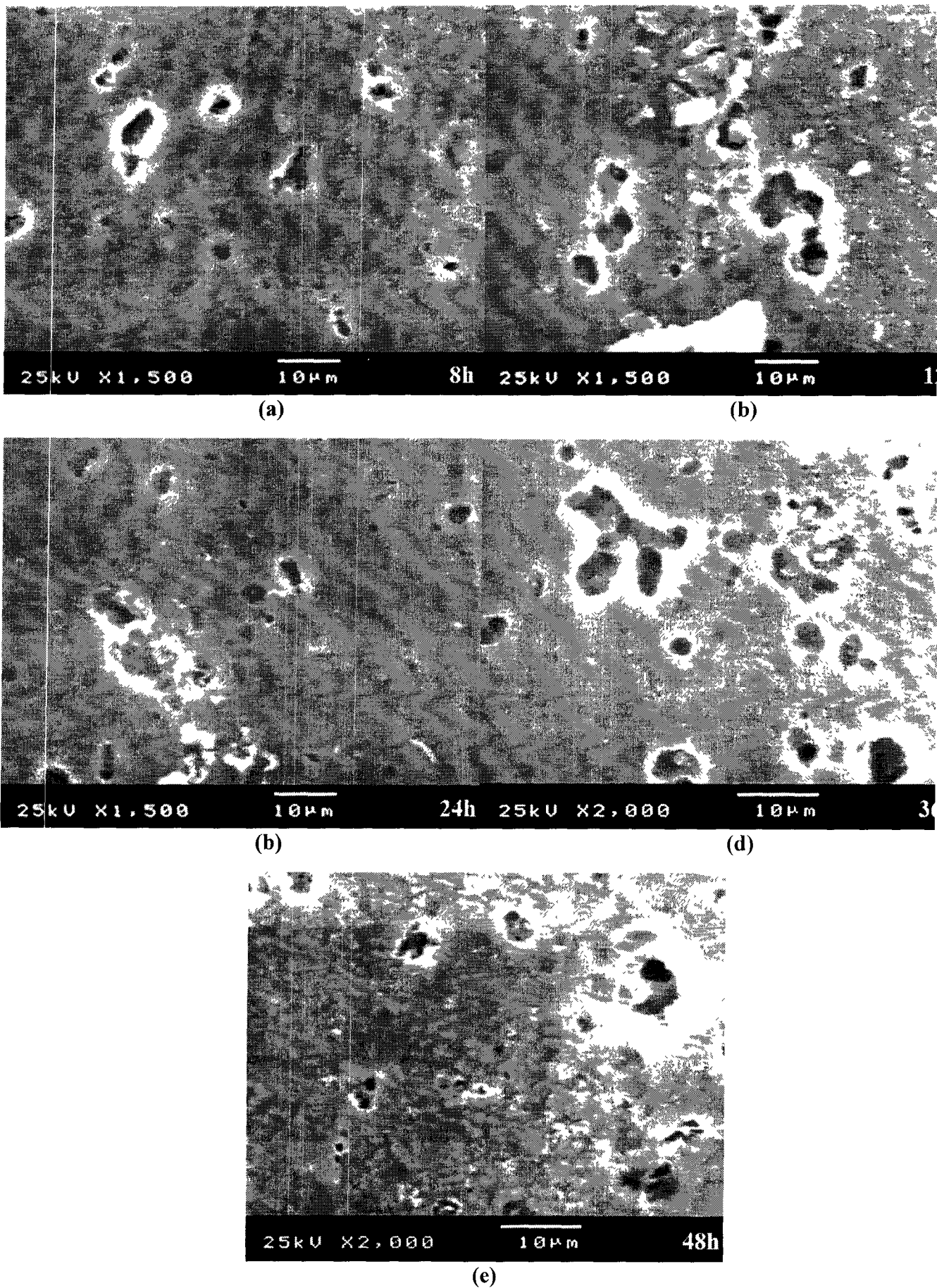
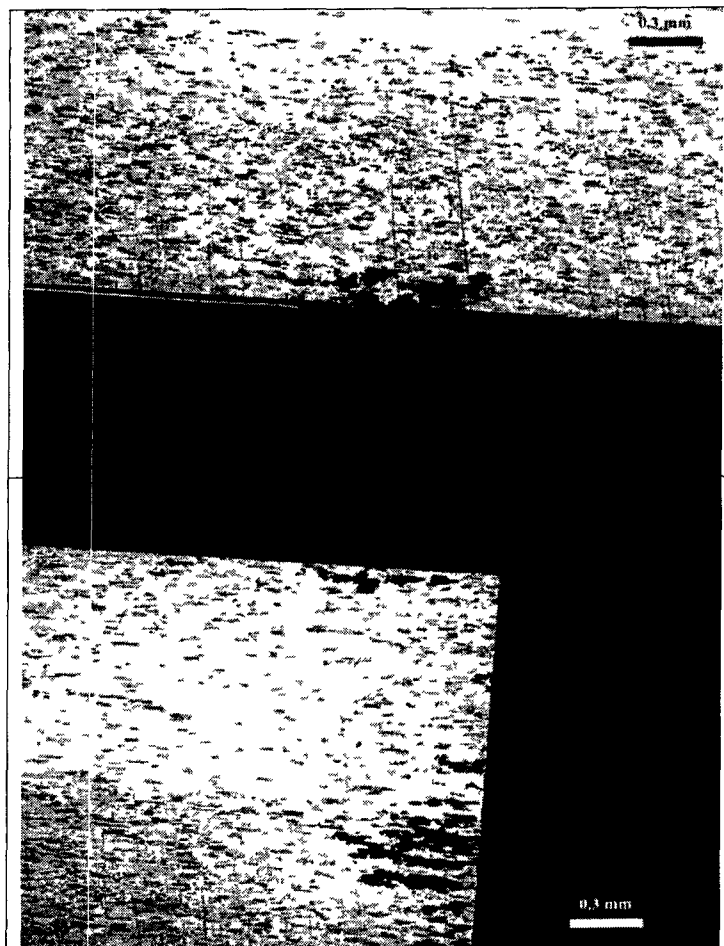


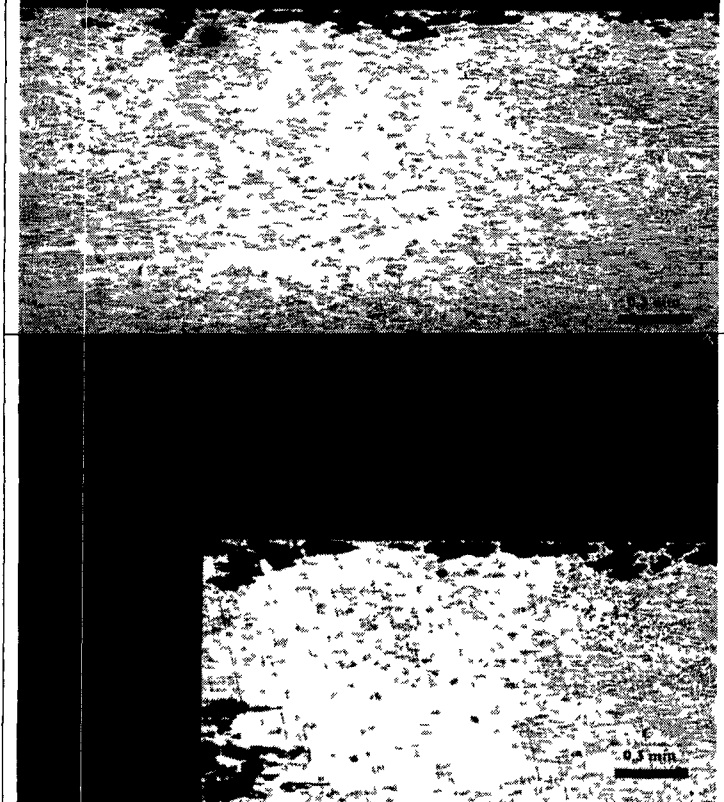
Fig. 4. 15: SEM topographies of Alloy 2024 (LT plane) exhibiting pit-to-pit interactions and pit clustering after exposure in EXCO for the indicated times.



(a)

(b)

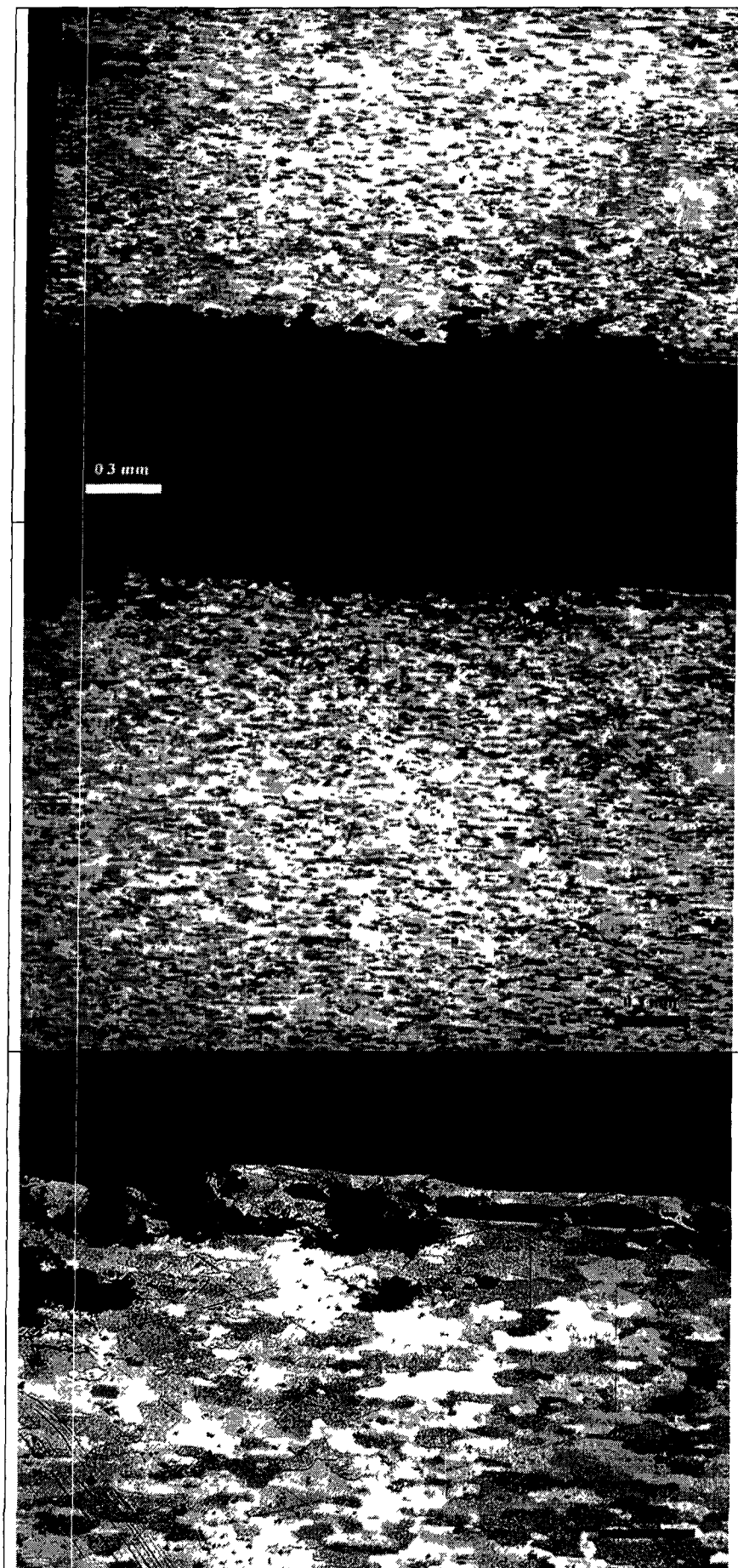
Fig 4. 16 Alloy 2024, 8 hours EXCO exposure



(a)

(b)

Fig 4. 17 Alloy 2024, 12 hours EXCO exposure



(a)

(b)

(c)

Fig 4 18 Alloy 2024, 24 hours EXCO exposure

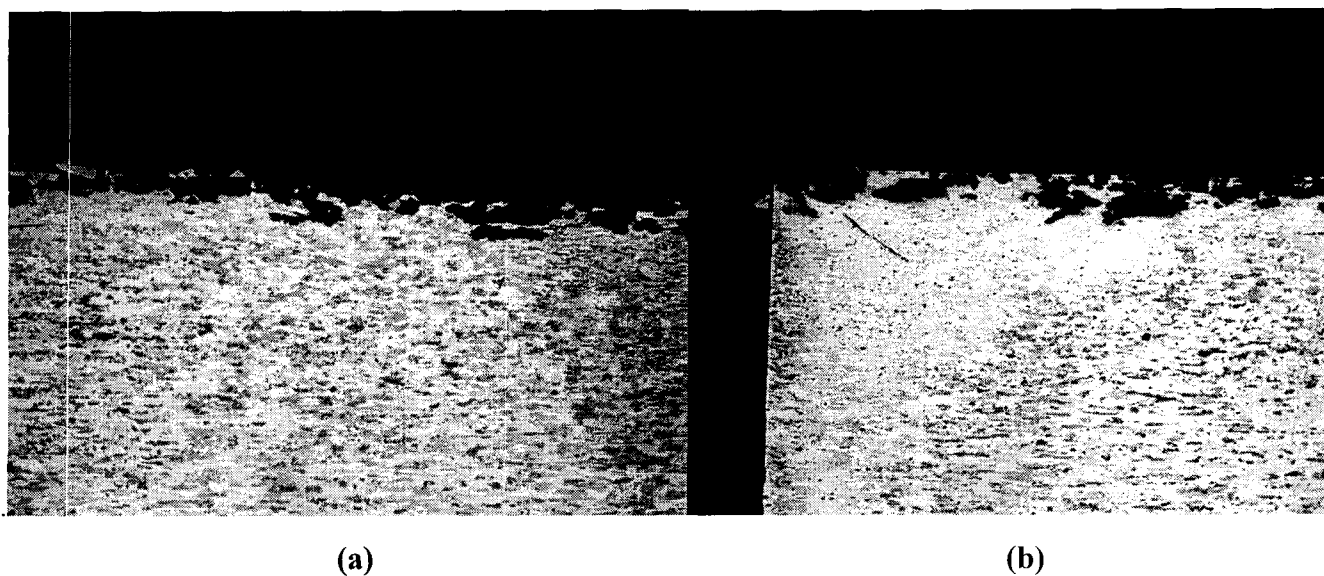


Fig. 4. 19: Alloy 2024, study of side surface 36 hours corrosion (x 50).

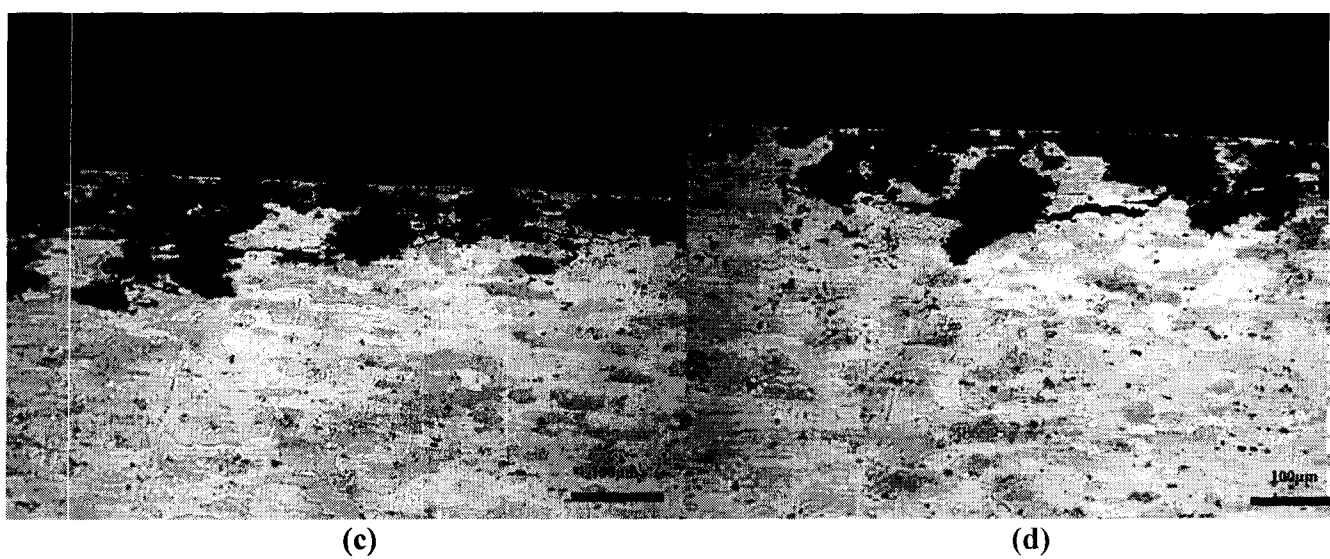
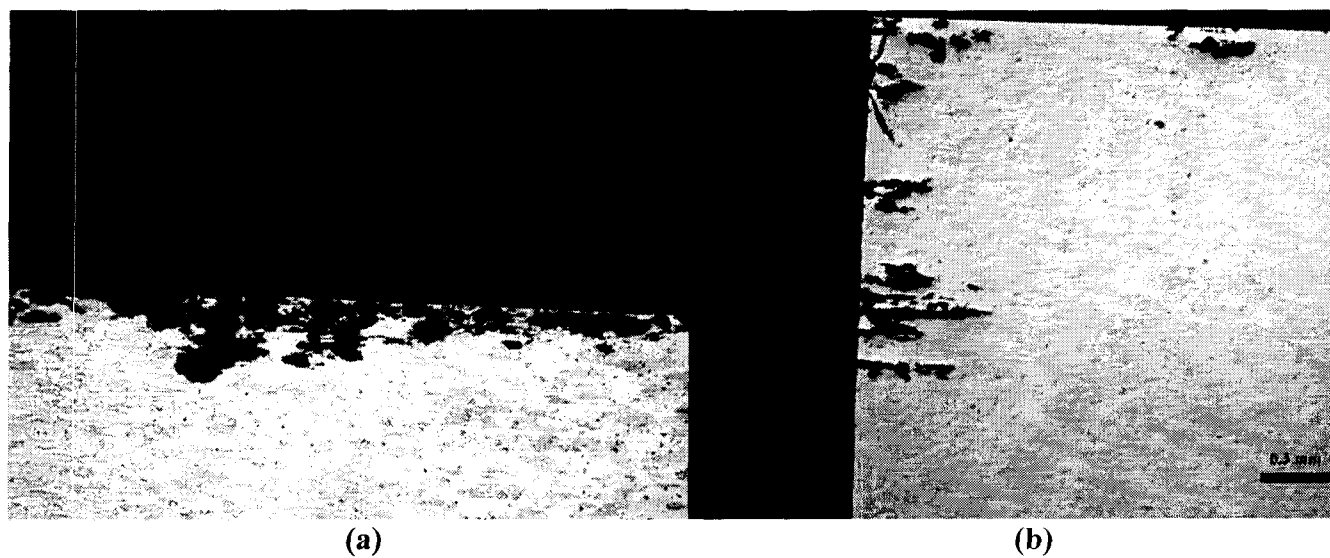


Fig. 4. 20: Alloy 2024, 48 hours EXCO exposure. Spreading of corrosion beneath surface by intergranular corrosion.

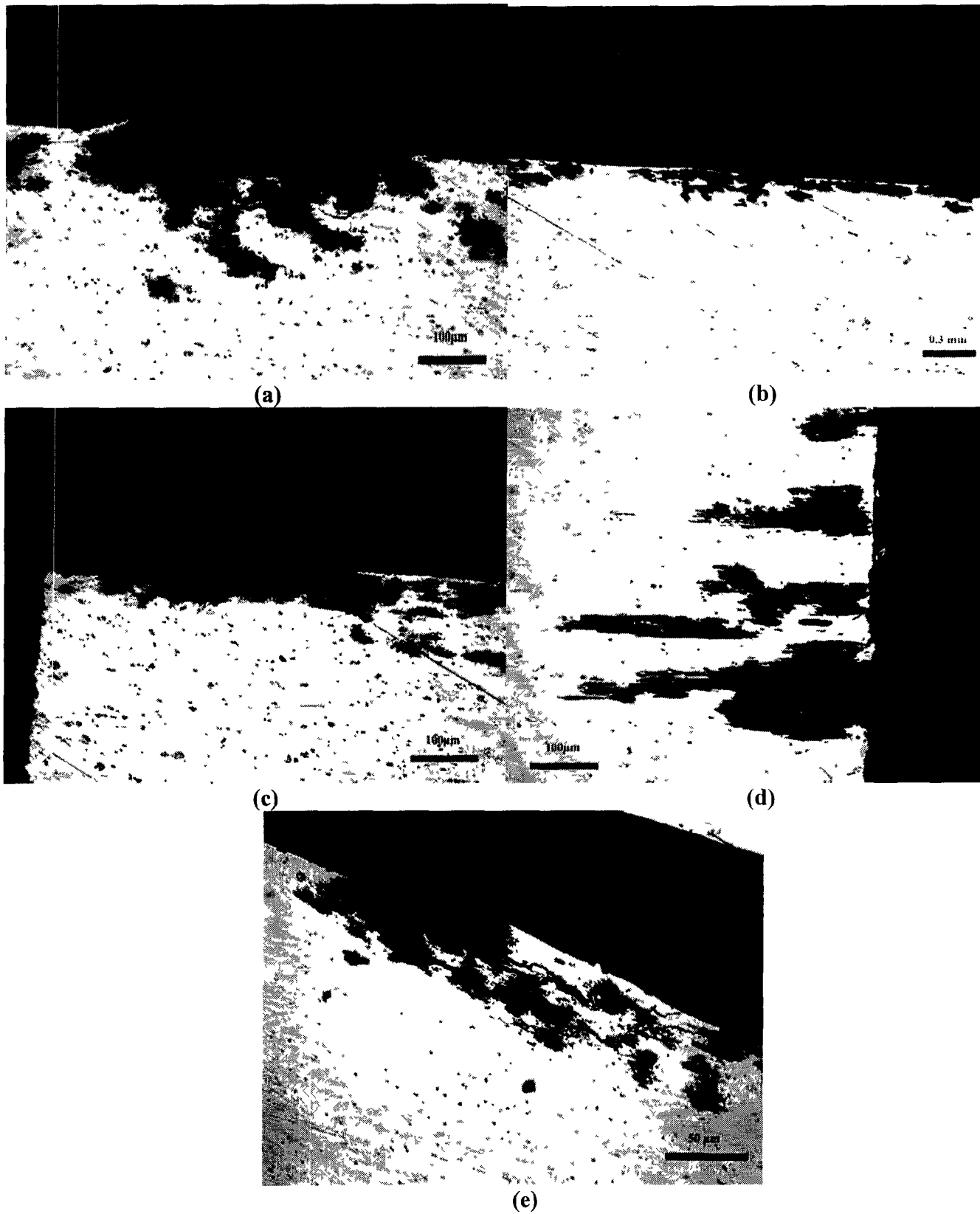


Fig. 4. 21: Alloy 2024, 72 hours EXCO exposure. Spreading of intergranular corrosion and exfoliation.

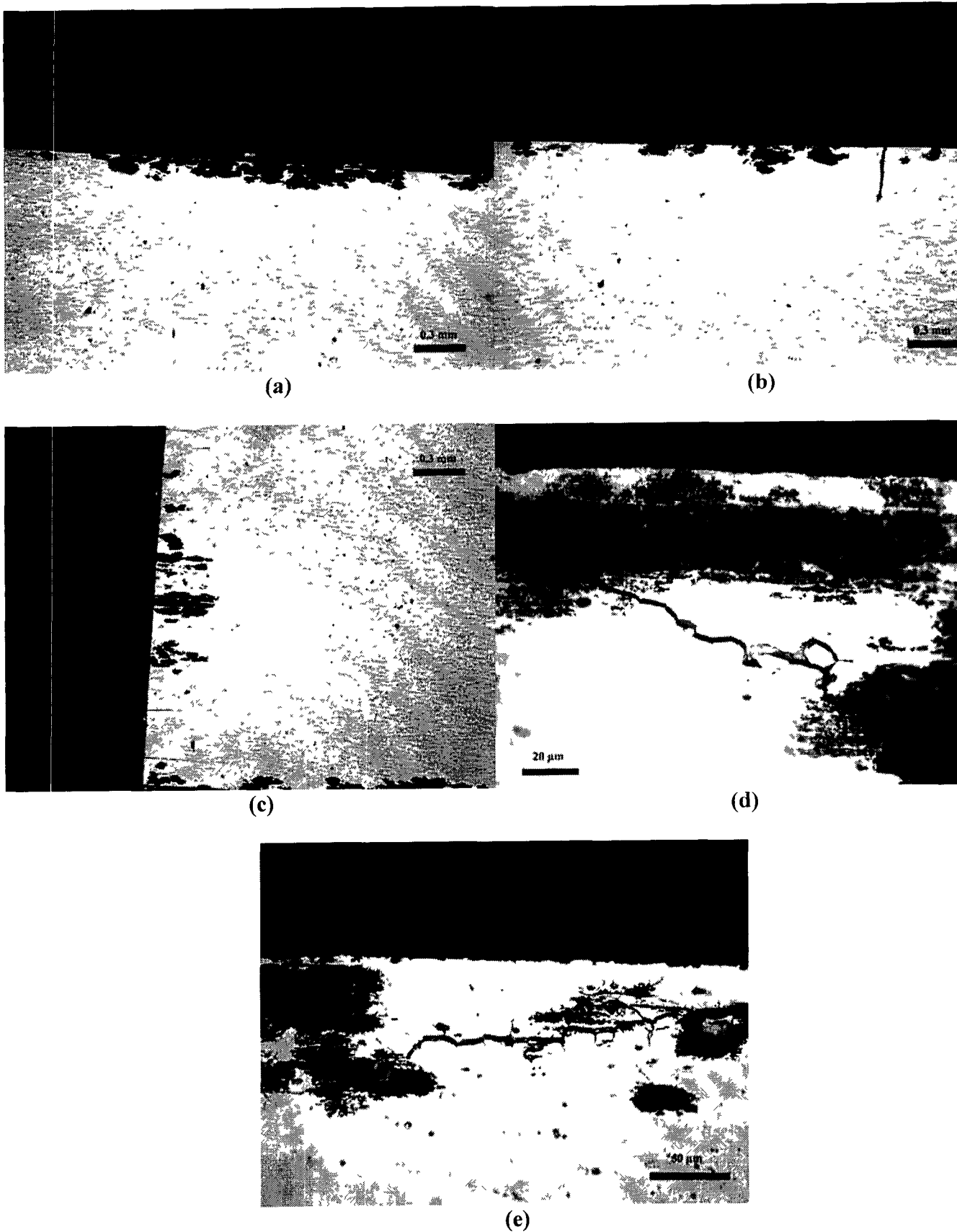


Fig. 4. 22: Alloy 2024, 96 hours EXCO exposure. Spreading of corrosion .Beneath the surface by intergranular corrosion leading to exfoliation.



## 4.2 Hydrogen penetration in 2024

### *Objective*

The objectives of the hydrogen measurement are the following:

- To determine the amount of hydrogen entering the material during corrosion
- To identify different trapping states and infer from their thermal characteristics the microstructural origin
- To measure the depth of hydrogen penetration and relate it to the depth of corrosion attack

The experimental setup for the thermal hydrogen desorption method was described in the previous chapter. Here, the measured hydrogen evolution spectra will be presented and discussed, and some details –pertinent to the reliability of the method– will be noted.

### *Hydrogen evolution spectra*

A plot of hydrogen flow rate in the purge stream versus temperature is shown for some representative cases in Fig. 4. 23. The pattern of hydrogen evolution is a strong function of specimen's temperature. This is an indication of a material with multiple trapping sites with different strengths. The curves in Fig. 4. 23 correspond to specimens with varying exposure time to the exfoliation solution (from 2h up to 96h). It is evident that the quantity of hydrogen increases drastically with the exposure time. Fig. 4. 24 is a magnification of they-axis and indicates that a similar dependence on corrosion exposure time also holds for the low-temperature part of the spectrum.

Multiple peaks are observed, in agreement with the experiments of Charitidou et al [93] and are attributed to different trapping states. The onset of the peaks labeled as T2, T3, and T4 occur at 200, 410, and 500°C, respectively. These represent critical temperatures below which no hydrogen evolution from the respective states is observed, even if the specimen is exposed to a constant, lower temperature for an extensive time period. According to Pressouyre [63], the existence of a critical temperature classifies states T2, T3, and T4 as irreversible. Trapping state T1 is found to release hydrogen continuously at lower temperatures. Thus, T1 is considered a reversible trap. This trap corresponds to the low binding-energy state reported by Haidemenopoulos et al. [89], who observed hydrogen evolution with mild heating of corroded Al 2024.

Total quantity of hydrogen in each trapping state is estimated by integrating the original concentration versus time data to calculate the area under each peak. Results for the four peaks are shown in Fig. 4. 25 (a, b, c, and d), where the amount of hydrogen (expressed in  $\mu\text{g H}$  relative to the specimen weight-) is plotted as a function of exposure time in the exfoliation solution. The three strong traps T2, T3, and T4 share common features. Linear increase of the amount of hydrogen with exposure time is initially observed followed by asymptotic approach to a constant value. This behavior is reminiscent of a saturation process by depletion of available active sites.

State T4 reaches a plateau concentration of 269 $\mu\text{g}$  after -35 h exposure in the exfoliation solution, while states T2 and T3 saturate at concentrations 8 and 76  $\mu\text{g}$ , respectively, after the elapse of -60 h. The fact that hydrogen desorbs from state T4 at the highest temperature of all identified trapping states indicates that T4 is energetically favored. The fact that this is the first state to become saturated further supports the above result.

### ***Microstructural origin of trapping states***

Even though the method of thermal analysis that was used in the present study does not allow direct identification of the trapping states, various conclusions can be reached, by correlating the measured hydrogen evolution temperatures to the structural characteristics of alloy 2024-T3 and to information from the literature.

As far as T1 is concerned it was noticed that whenever, after the exfoliation corrosion, the specimen was kept in a room temperature for several days and then measured for hydrogen, the trapping site T1 had vanished. This means that this state is not temperature sensitive and requires very low activation energy. The amount of hydrogen in the T1 state (increases linearly with exposure time, and no saturation is evidenced up to an exposure of 120 h in the exfoliation solution. Since it is the lowest energy state observed, T1 could in principle be associated with adsorbed hydrogen. However, in aluminum alloys the energy of chemisorption is lower than the migration energy and no peak should appear. Given the fact that T1 is a low-energy state and-when compared to the other states -relatively unsaturable, it would appear that this trapping state is related to hydrogen at interstitial sites. Hydrogen is bonded very near the surface of the material. It is the last hydrogen produced from the chemical reaction of corrosion that did not have enough time to diffuse in the bulk of the material. In this state hydrogen is trapped in microcracks along grain boundaries, resulting from the intergranular corrosion of the material during its stay in the Exco solution, as is described in the model discussed earlier. The continuous increase in the amount of hydrogen with exposure time to the exfoliation solution is attributed to the creation, by the corrosion process, of new penetration paths for hydrogen (intergranular cracks and surfaces), as reported by Haidemenopoulos et al. [89].

On the contrary, traps T2, T3, T4 exhibit higher activation energies for the release of hydrogen. This means that hydrogen has diffused further into the material and has formed powerful bonds that are harder to break. Trapping state T2 is an intermediate energy state that saturates with relatively little hydrogen. A possible physical origin of this trap is the interface between the Mg<sub>2</sub>Si precipitate and the matrix lattice. The Mg<sub>2</sub>Si precipitate is incoherent with the matrix and the interfacial dislocations that exist around it can trap hydrogen. This has been shown by Saitoh et al. [83], using tritium autoradiography.

The critical temperature of 410 °C, below which no hydrogen evolves from state T3, compares favorably with the thermal decomposition temperature of MgH<sub>2</sub> as reported by Tuck [85] (450 °C with a heating rate of 50 °C /min, which should bias the peak to higher temperature). Thus, trapping state T3 could tentatively be associated with Mg hydride. It has been noted by Saitoh et al. [83] that Mg is bonded to Si by a strong ionic bond that precludes formation of MgH<sub>2</sub>. However, Mg content in the 2024 alloy presently tested is in roughly 40% excess over the stoichiometric analogy with Si and-if saturated-results in a 500-μg concentration of hydrogen. This estimate compares favourably with the plateau of 300 μg shown in Fig. 4. 25c

The critical temperature of 500 °C, which marks hydrogen evolution from state T4, coincides with the dissolution temperature of the Al-Cu precipitate, as calculated by the computational alloy thermodynamics software ThermoCalc [94]. Thus, trapping state T4 could be associated with this phase. Indeed, it has been demonstrated by tritium autoradiography [83] that the bulk of the θ precipitate can serve as a hydrogen trap.

### ***Depth of hydrogen penetration***

Experiments were performed in order to estimate the depth of hydrogen entry during corrosion of Al-alloy 2024-T3. This depth defines the “hydrogen affected zone”, whose extent will be set in perspective with the corrosion zone and will later help interpret the fracture behavior of the alloy. Five identical specimens from the 2.4 mm thick plate were exposed to

the EXCO corrosion test for 24 hours. The first specimen was measured for  $H_2$  immediately after cleaning, while the others were ground on all six sides by 50 $\mu\text{m}$ , 100 $\mu\text{m}$ , 200 $\mu\text{m}$  and 350 $\mu\text{m}$  respectively.

Results of  $H_2$  evolution as a function of temperature for the above specimens are depicted in Fig. 4. 26 . Measurement of an uncorroded specimen is included for comparison. The results indicate the expected decrease in hydrogen content with depth. However, it is interesting to note that the amount of  $H_2$  remaining after removal of 350  $\mu\text{m}$  from a corroded specimen is significantly higher than the amount measured in the uncorroded specimen. Thus, we conclude that the hydrogen-affected zone extends beyond a depth of 350 $\mu\text{m}$ .

The total amount of hydrogen evolving from the above specimens is found by integration of the data. The outcome is shown in Fig. 4. 27 and confirms the above conclusion. A reasonable estimate of the depth of hydrogen penetration, based on these data, is 400-500  $\mu\text{m}$ . The resulting diffusion coefficient is  $D=1.2 \times 10^{-13} \text{ m}^2/\text{s}$ , which is in the correct order of magnitude for volume diffusion in Al alloys.

The extent of the hydrogen-affected zone should be compared to the depth of corrosion attack, in order to. To this end, multiple metallographic sections of corroded specimens were taken. Pictures representative of deepest penetration are shown in Fig. 4. 28 for the 2.4 mm plate and in Fig. 4. 29 for the 3.0 mm plate. It is evident that corrosion is not uniform. In particular, both figures indicate that the side-surfaces of the specimens are more prone to attack than the rolling surfaces (In Fig. 4. 29, side surfaces are the top and bottom ones). Deepest penetration occurs at the middle plane (parallel to the rolling surfaces), and may be explained from the fact that the plates are rather thick and quenching of the middle region during production is not as rapid as desired.

However, the most important conclusion from the metallographic sections is that the penetration of the corroded zone is insignificant beyond 350  $\mu\text{m}$ . Thus, the deterioration of mechanical properties and the appearance of hydrogen, in specimens from which 350  $\mu\text{m}$  of material has been removed from all sides, cannot be attributed to the corrosion layer but must be a diffusion effect.

The picture that emerges is that a hydrogen-affected zone is formed below the corrosion zone. During corrosion, there is continuous progression of the zone boundaries: thus hydrogen-affected material becomes corroded (possibly releasing the trapped hydrogen), while new material is affected. We also note that, because of the non-uniform shape of the corrosion zone, hydrogen-rich material is removed, together with corrosion products, during grinding. Thus, the amounts of hydrogen measured stem mostly from the deeper regions of the affected zone.

### ***The role of specimens cleaning in the reliability of hydrogen measurement***

The quantitatively reliable investigation of hydrogen uptake during corrosion demands caution. For example corrosion attack should be done in a temperature regulated environment ( $\pm 0.5^\circ \text{C}$ ). Otherwise, variations in ambient temperature affect the speed of corrosion reactions and lead to poor reproducibility.

An additional concern has to do with the origin of detected hydrogen. More specifically, we need to confirm that the hydrogen measured by heating of the corroded specimen is eluted from the interior of the specimen and not produced by surface reactions. A potential source of surface hydrogen production is the decomposition of water contained in hydrated corrosion products, which have deposited on the specimen. Thus, careful cleaning of the specimens after completion of corrosion and before hydrogen measurement is necessary for complete removal of corrosion products.

After consideration of standard specifications, the following two cleaning methods were selected for testing:

- (a) Soaking for 10 min in concentrated  $\text{HNO}_3$ , rinsing in distilled water and drying in air (method A).
- (b) Soaking for 15 minutes in 30%  $\text{HNO}_3$ , then pickling for 1 minute in 5%  $\text{NaOH}$  at  $80^\circ\text{C}$  and finally washing in acetone and drying (method B, suggested by Airbus).

Both cleaning procedures were tested, but method B appeared to be inappropriate for the present investigation and was abandoned. More specifically, it led to excessive weight loss, which resulted from the removal of relatively large amounts of uncorroded material (observed visually). As a consequence, it gave irreproducible measurements of hydrogen evolution for specimen subjected to the same corrosion history, because part of the trapped hydrogen was contained in the material removed during cleaning.

The remaining candidate cleaning method A was further tested for possible interference with hydrogen uptake. Thus, multiple uncorroded specimens were measured for hydrogen, some of them as received, others just washed with acetone and others cleaned according to method A. The results proved totally insensitive to the treatment, as indicated from the representative data of Fig. 4. 30. Based on the above assessment, method A was used in the rest of the present investigation.

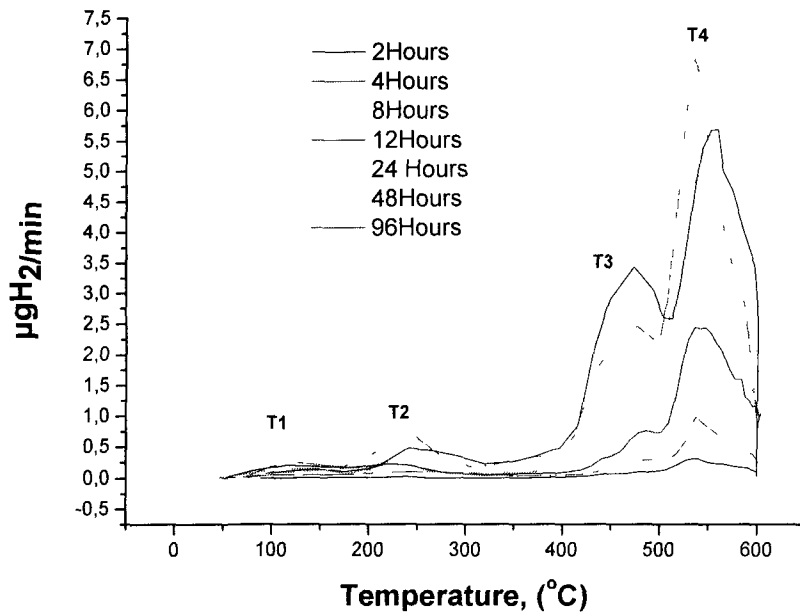


Fig. 4. 23: Desorption of  $\text{H}_2$  in specimens of aluminium alloy 2024-T3 for continuous heating up to 600  $^{\circ}\text{C}$ . Thickness of material 1,8 mm.

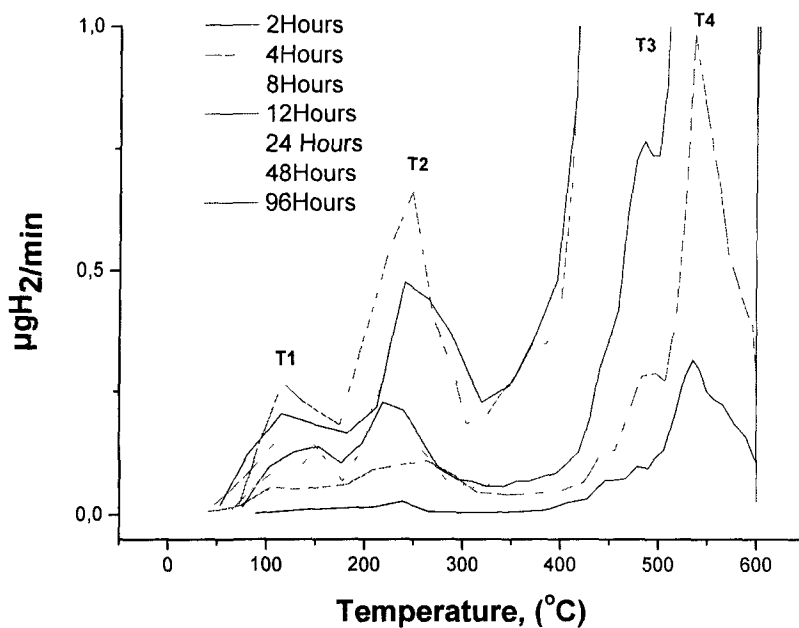


Fig. 4. 24: Magnification of Previous Figure in the region up to 1.0  $\mu\text{gH}_2/\text{min}$ .

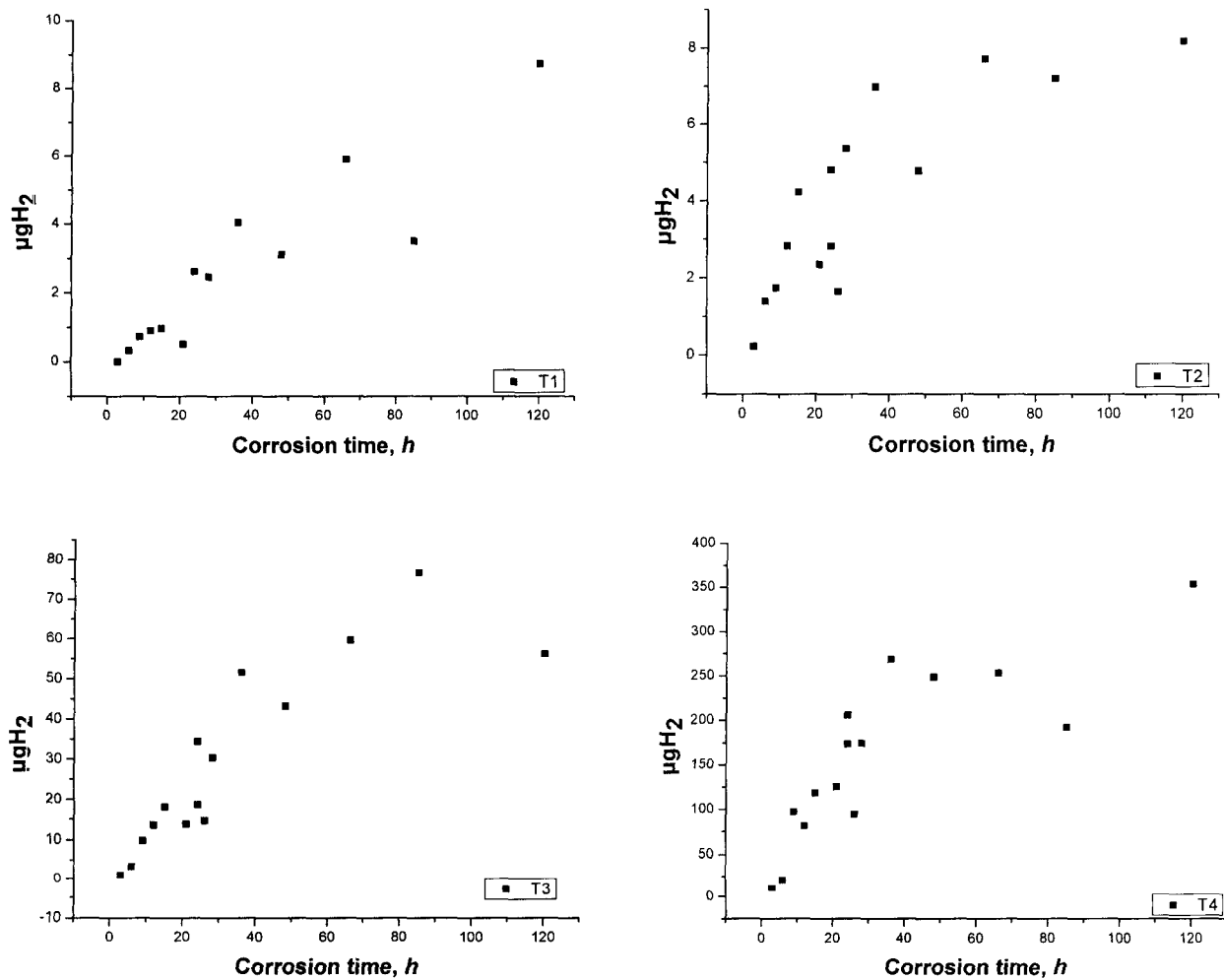


Fig. 4. 25: Amount of hydrogen desorpted from the four trapping states (T1-T4) as a fuction of corrosion exposure time.

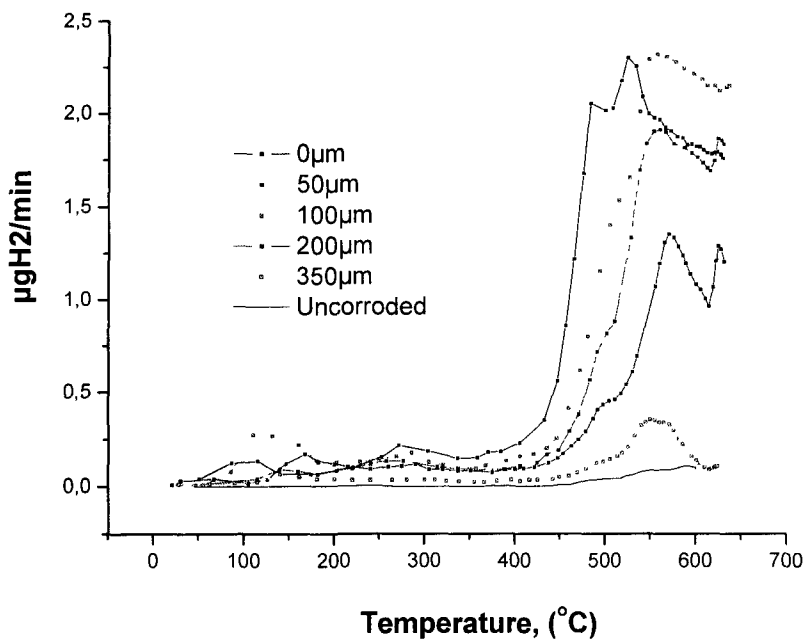


Fig. 4. 26: H<sub>2</sub> evolution as a function of temperature for specimens with varying removal depth.

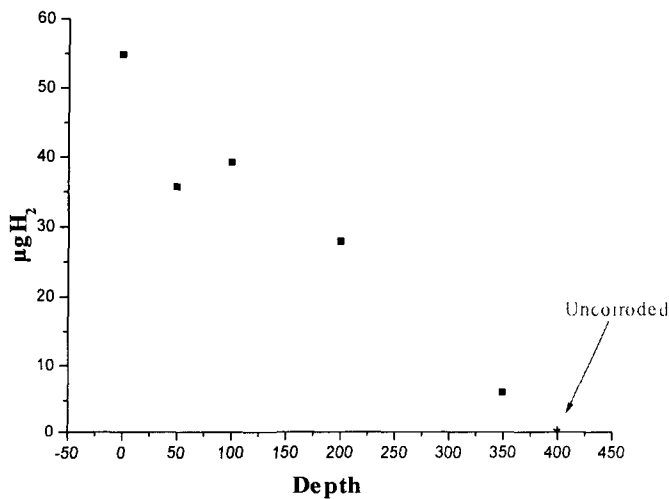


Fig. 4. 27: Total amount of H<sub>2</sub> (µg) for different removal depths. 24h exposure to EXCO solution (2.4 mm).

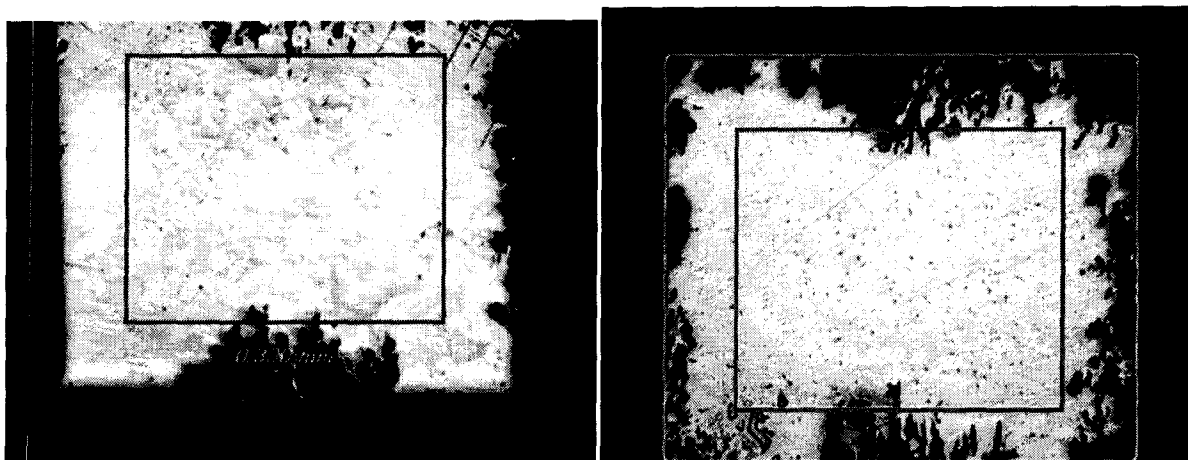


Fig. 4. 28: Depth of Attack 2.4mm

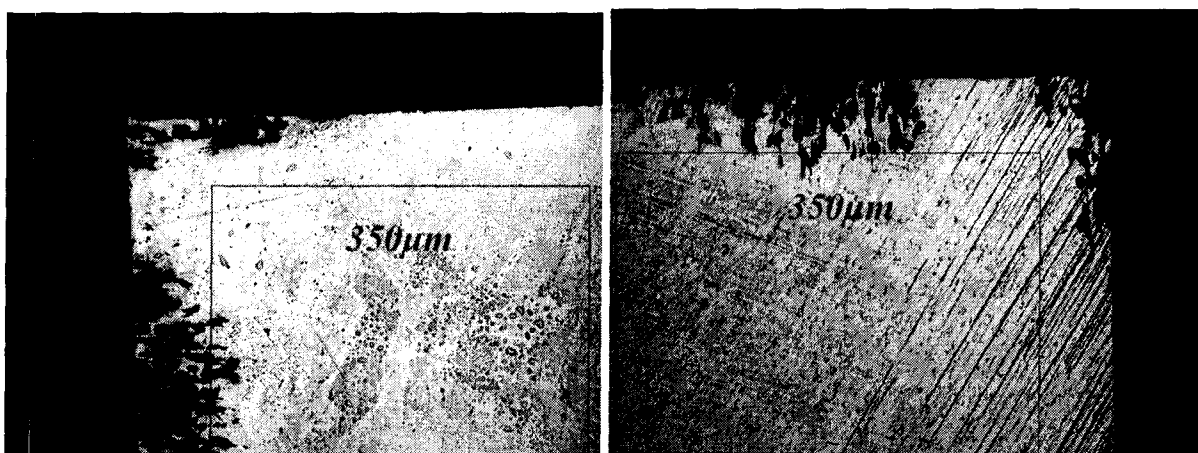


Fig. 4. 29: Depth of Attack 3 mm.

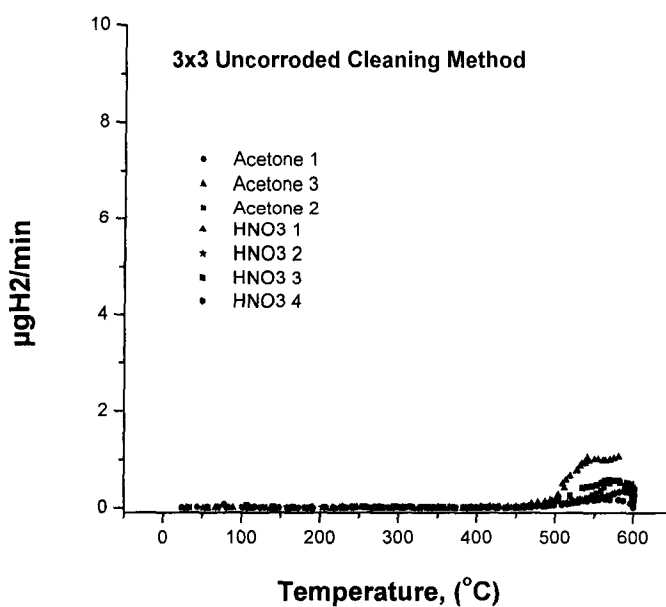


Fig. 4. 30: Hydrogen in Uncorroded Specimen of 3mm (b).



### 4.3 Microhardness measurements

The hydrogen uptake and trapping spectra presented in the previous paragraphs provide some clues about the trapping states based on the temperatures where hydrogen desorption is activated. However during the thermal desorption test, the material undergoes microstructural changes due to heating. These changes can be monitored with hardness measurements and the comparison between corroded and uncorroded material should determine any differences that can be attributed to hydrogen uptake.

As described in Chapter 3 (Experimental Procedures) two sets of specimens (corroded EXCO 24h and uncorroded) were subjected to the thermal desorption cycle (heating up to 500°C with a heating rate of 5°C/min. Every 50°C temperature rise a specimen from each set was removed from the furnace and quenched. In the corroded set of specimens the corrosion layer was mechanically removed before the hardness measurement.

The results of the measurements appear in Fig. 4. 31 together with the corresponding hydrogen spectrum for 24h EXCO. The hardness of the uncorroded (bare) material generally decreases with temperature up to 400°C due to overaging (a slight increase at 250°C is attributed to a secondary ageing peak), while it rises again above 400°C due to dissolution and reprecipitation. The corroded material exhibits a similar behavior in general. However there are two distinct differences in the hardness values. The corroded material appears softer than the uncorroded up to 300°C and harder above 350°C. The first temperature region incorporates states T1 and T2. Hydrogen in the T1 state is trapped in interstitial sites and dislocations while T2 hydrogen is trapped at particle/matrix interfaces. Recent research indicated that hydrogen might aid dislocation motion by altering the binding energy between dislocations and solute atoms [95, 96]. On the other hand hydrogen at matrix/particle interfaces might alter the interaction energy between dislocations and particles for coherency hardening in a way similar to that proposed for lattice dislocation. The result is that hydrogen in T1 and T2 states probably aids dislocation motion in overcoming either the lattice resistance or semicoherent particle resistance and the corroded material appears softer.

The second temperature region (above 300°C) incorporates states T3 and T4. T3 hydrogen is trapped in Mg hydride formation, while T4 hydrogen is trapped in the main hardening phase ( $\theta$  or S). It is apparent from Fig. 4. 31 that hydrogen affects the dissolution and reprecipitation process or even the overaging (coarsening) process in the alloy and the corroded alloy appears harder. However more work is needed to clarify this behavior.

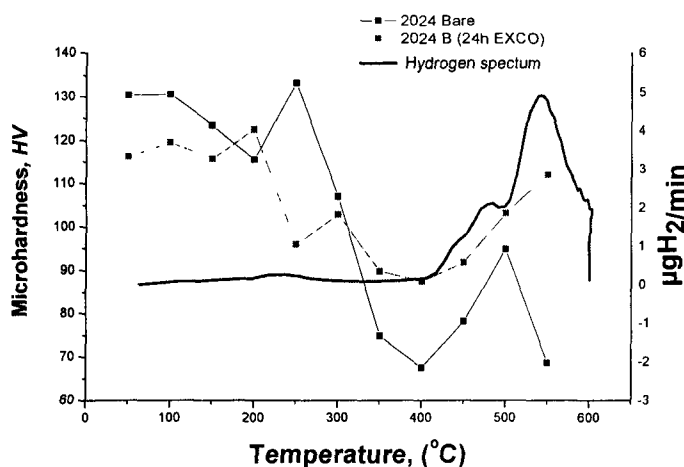


Fig. 4. 31: Microhardness profile versus temperature for alloy 2024.

## 4.4 Fractography of tensile specimens

The experimental measurements presented in the previous paragraphs established the following conditions:

- The depth of corrosion attack for 24h EXCO is of the order of 350 $\mu$ m
- There is a hydrogen profile in the hydrogen-affected zone, which extends beyond 350 $\mu$ m. The amount of hydrogen remaining after removal of the 350 $\mu$ m corrosion layer is significantly higher than the amount of hydrogen in the uncorroded material

The above results indicate that a hydrogen diffusion zone should exist just below the corrosion layer. In case this was true, it should reflect on the mechanical properties. Thus it was decided to carry out tensile tests in order to determine the tensile elongation, as a measure of ductility and to correlate these results with fractographic analysis of the fracture surfaces of the tension specimens. The tensile experiments were conducted by the Laboratory of Technology and Strength of Materials of the University of Patras and are described in [97]. The following conditions were investigated:

U: Uncorroded specimen

UH: Uncorroded + Heat treatment at 495°C

UR: Uncorroded + Removal of 350 $\mu$ m layer

URH: Uncorroded + Removal of 350 $\mu$ m layer + Heat treatment at 495°C

C: Corroded 24hEXCO

CH: Corroded + Heat treatment at 495°C

CR: Corroded + Removal of 350 $\mu$ m layer

CRH: Corroded + Removal of 350 $\mu$ m layer + Heat treatment at 495°C

The results of the tensile tests are given in the following table

Table 8: Results of tensile tests [97].

Condition	Yield strength $S_y$ (MPa)	UTS $R_m$ (MPa)	Elongation $A_{50}$ (%)	Energy Density $W$ (MJ/m <sup>3</sup> )
U	376.12	488.90	15.35	71.90
UH	326.90	495.80	17.45	80.70
UR	358.10	472.00	16.24	74.11
URH	296.44	447.29	14.09	58.64
C	348.88	424.50	5.99	25.04
CH	303.10	433.26	9.83	39.81
CR	363.45	467.72	10.76	48.46
CRH	286.42	438.26	13.92	56.48

The conditions U, UH, UR and URH serve as reference of the conditions C, CH, CR and CRH respectively. The results of Table 8 can then be represented as percentages of the respective reference values. This is shown in Table 9 and in Fig. 4. 32.

The results presented in Table 9 and Fig. 4. 32 depict the following:

Corrosion degrades yield strength and ultimate tensile strength as expected, however the degradation of tensile ductility (elongation and energy density) is more pronounced (Condition C). Examining conditions CH and CR independently we see that the removal of the corrosion layer restores entirely the strength values and enhances the tensile ductility. Heating of the corroded material does not affect the strength values; however it enhances the tensile ductility. Removal of the corrosion layer and then heating the material not only restores the strength values but it also restores ductility as well (condition CRH).

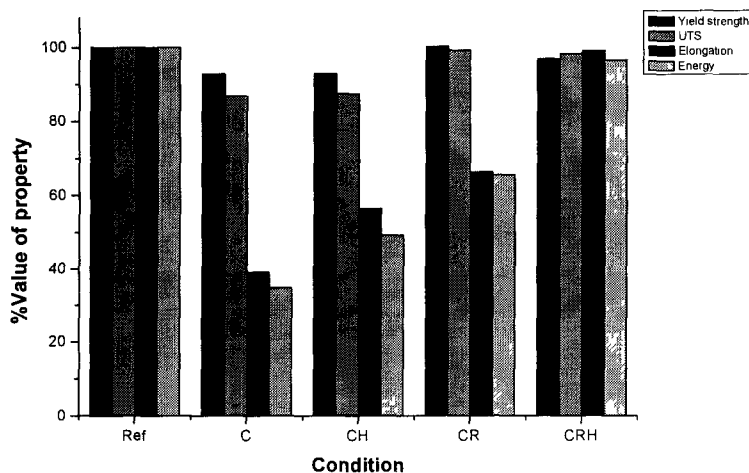


Fig. 4. 32: The results of Table 8 represented as percentages of the respective reference values [97].

Table 9: Tensile properties as %value of reference specimen [97].

Condition	Yield strength	UTS	Elongation	Energy
<b>C</b>	92.7	86.8	39.0	34.8
<b>CH</b>	92.7	87.3	56.3	49.3
<b>CR</b>	100	99.0	66.2	65.4
<b>CRH</b>	96.6	98.0	98.8	96.3

Corrosion (24h EXCO) affects a surface layer (350 $\mu$ m) of the material by introducing defects such as pitting, exfoliation and intergranular attack. These features degrade the strength of the material. Corrosion also degrades the ductility due to the combined effect of the corrosion defects described above and hydrogen embrittlement. The last point is apparent from condition CR, where the removal of the corrosion layer restored the strength values due to the simultaneous removal of the corrosion defects. However ductility was not completely restored, and this calls for a bulk mechanism of embrittlement. The indication that this mechanism is hydrogen embrittlement comes from the following considerations:

1. There is a hydrogen profile in the corrosion layer, but even after removal of that layer the hydrogen remaining is still significant
2. Heating the corroded material (condition CH) does not affect strength. It affects only ductility and actually restores ductility to some extent. Heating is performed at 495°C, at the T4 trapping state, to diffuse all hydrogen out of the material by activating all trapping states.
3. Removal of the corrosion layer (condition CR) removes the corrosion defects and all the hydrogen that is trapped in the corrosion layer. Thus the restoration of ductility here is more pronounced
4. Removal of the corrosion layer and heating the material at 495°C (condition CRH) completely restores ductility due to the combined effect of removal of corrosion defects and hydrogen

To support these considerations, a fractographic analysis of the fracture surfaces of the tension specimens was conducted especially to clarify point No.1 above.

The investigation was carried out for the following conditions

Corroded 24h (condition C)

Corroded 24h + Removal of 350 $\mu$ m (condition CR)

Corroded 24h + Removal of 350 $\mu$ m + Heat treatment 495°C/35min (condition CRH)

Non-Corroded + Removal of 350 $\mu$ m + Heat treatment 495°C/35min (condition URH)

Condition C: Fig. 4. 33 shows a low magnification section of the fracture surface at the top side of the specimen. The fracture surface appearance varies from the specimen surface to the specimen interior. At the specimen surface the fracture is intergranular as shown in Fig. 4. 33a. Immediately below there is a zone of quasicleavage fracture (Fig. 4. 33b) and further below the fracture turns to entirely ductile (dimples), shown in Fig. 4. 33c and d. A similar behaviour exists at the bottom side of the specimen, shown in Fig. 4. 34. There is again an intergranular surface region (Fig. 4. 34a), a quasicleavage zone below (Fig. 4. 34b), a transition from quasicleavage to ductile fracture (Fig. 4. 34c) and completely ductile fracture in the interior (Fig. 4. 34d). It is apparent from these results that the intergranular layer is the corrosion layer. Immediately below the corroded layer there exists an embrittled zone characterized by the quasicleavage fracture appearance. This embrittled zone is followed by the normal ductile fracture mode of the alloy.

Condition CR: Fig. 4. 35 shows a low magnification section of the broken tensile sample. Here the intergranular surface region is absent, since the corrosion layer was removed. However the embrittled region in the form of quasicleavage is still present (Fig. 4. 35a) followed by a transition to ductile fracture (Fig. 4. 35b, c). The same situation holds and in another specimen of the same condition, shown in Fig. 4. 36 which clearly shows the embrittled zone (Fig. 4. 36a), the transition to ductile (Fig. 4. 36b) and the ductile region in the interior of the specimen (Fig. 4. 36c).

Conditions CRH and RH: Both conditions show a completely ductile (dimple) fracture appearance in the interior (Fig. 4. 37 and b). Also both conditions exhibit a surface zone of mixed intergranular/dimple nature (Fig. 4. 38a,b). This surface zone is absent from the previous C and CR conditions and is attributed to the heat treatment applied prior to tensile testing. A more close examination in higher magnifications shows rounded features either in dispersed particles (Fig. 4. 39a) or even at grain boundaries (Fig. 4. 39b). This roundness might be due to the exposure to the relatively high heat treatment temperature of 495°C. The presence of this heat-treatment affected zone in both conditions CRH and RH overlapped any effect of corrosion and to correlate with the tensile results of Fig. 4. 32. Therefore this makes very difficult to determine the effect of corrosion. The above arguments hold for the L-direction specimens. The situation in the LT specimens is similar. However here the intergranular character of the surface zone is more apparent (Fig. 4. 40) due to the orientation of the grains relative to the fracture surface

The fractographic analysis for conditions C and CR presented above correlate with the hydrogen profile in the material (Fig. 4. 27) and the tensile data of Fig. 4. 32. The hydrogen affected zone extends below the corrosion layer. This is the embrittled (quasicleavage) zone between the intergranular corrosion and the ductile uncorroded matrix seen in the above fractographs. Removal of the corrosion layer (CR) removes the effects of corrosion but leaves the hydrogen embrittled zone in place. This is the reason for the incomplete restoration in ductility for condition CR. Only in condition CRH, where all hydrogen has also been removed, there is a complete restoration of ductility.

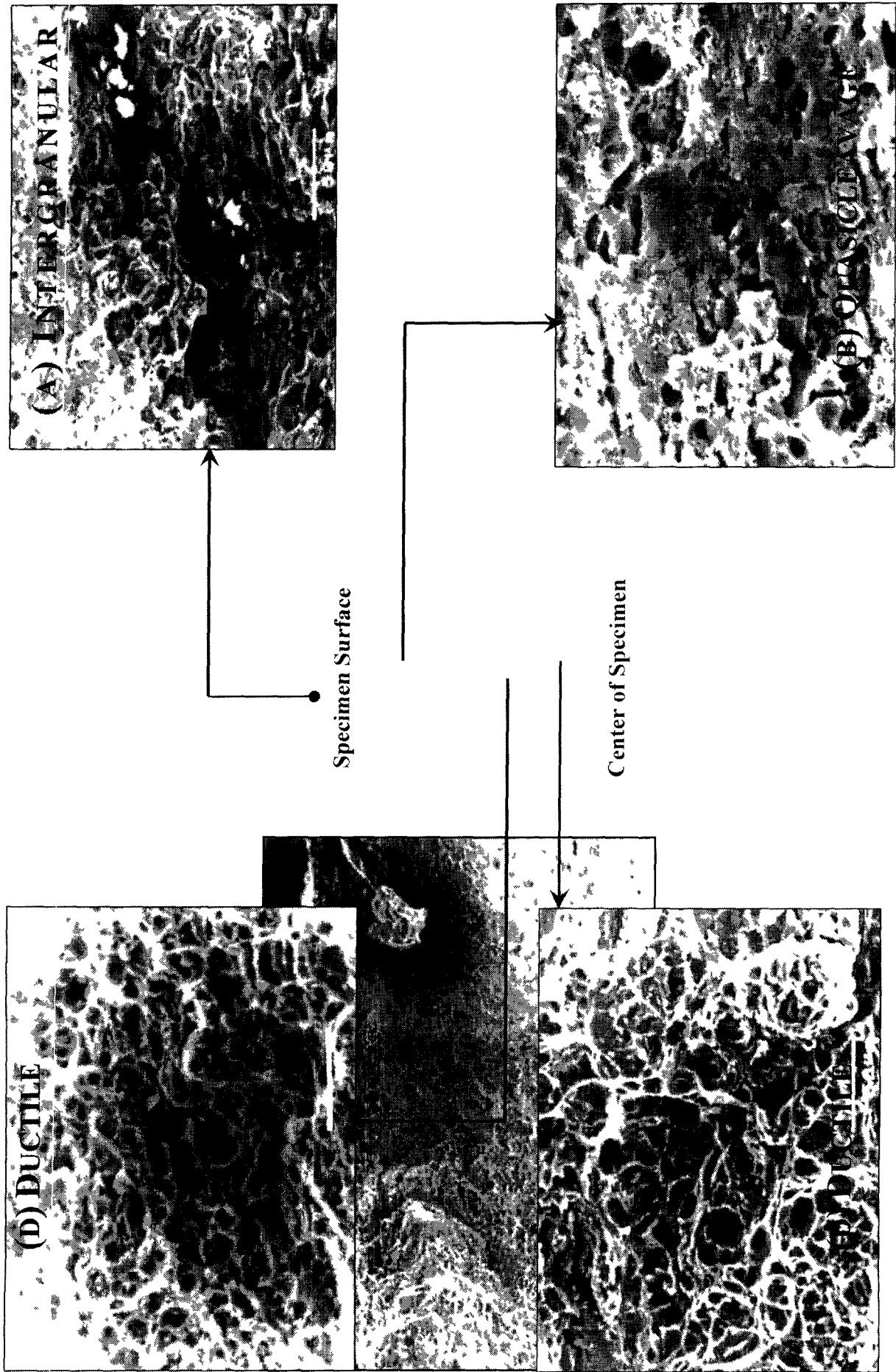


Fig 4 33 Fracture surfaces of condition C (corroded 24h) specimen. Individual photos correspond to different modes of fracture from the specimen surface (on start of corrosion) through the centre of the specimen.

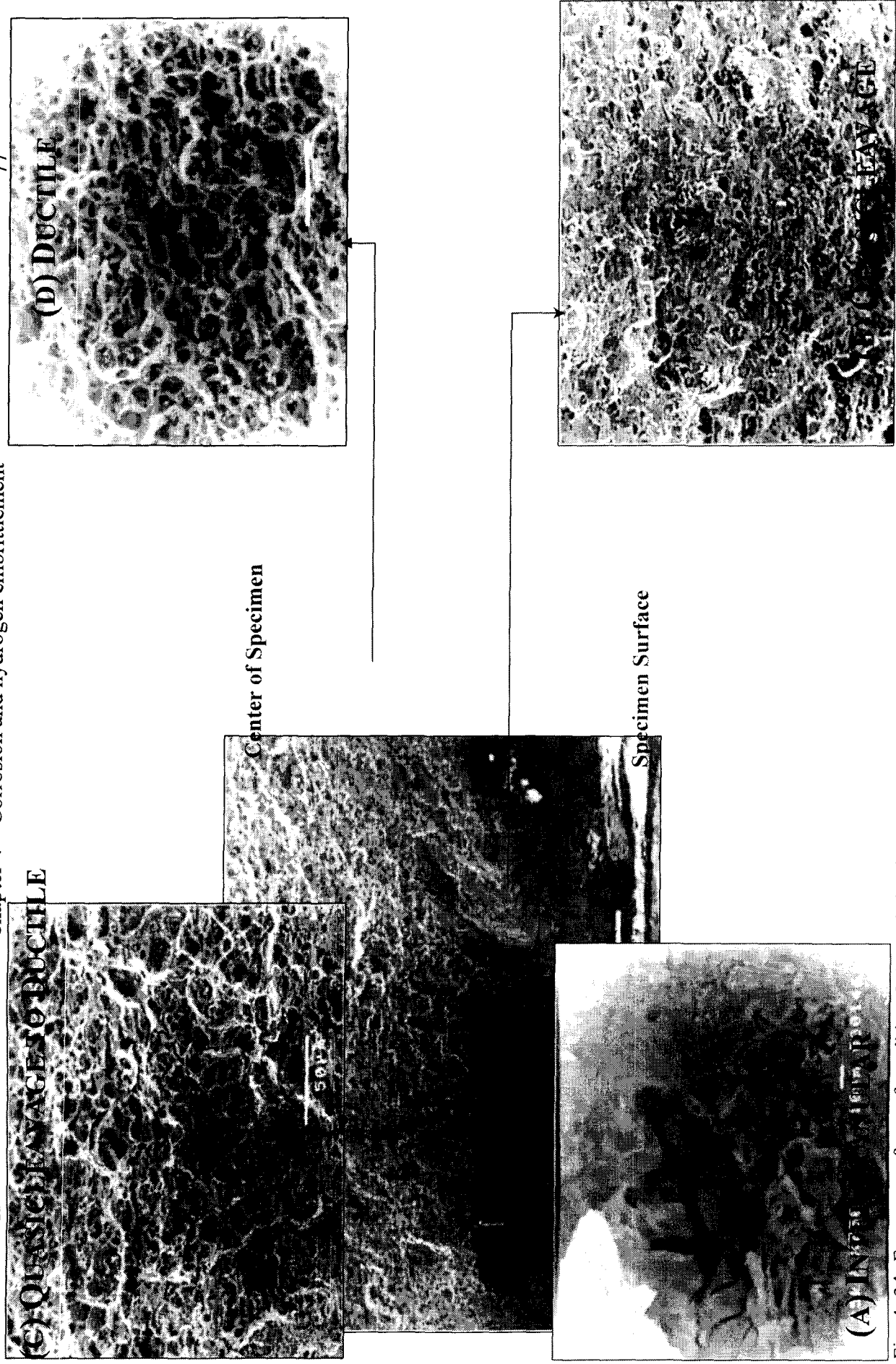


Fig. 4. 34: Fracture surfaces of condition C (corroded 24h) specimen, bottom surface. Individual photos correspond to different modes of fracture from the specimen surface (on start of corrosion) through the center of the specimen.

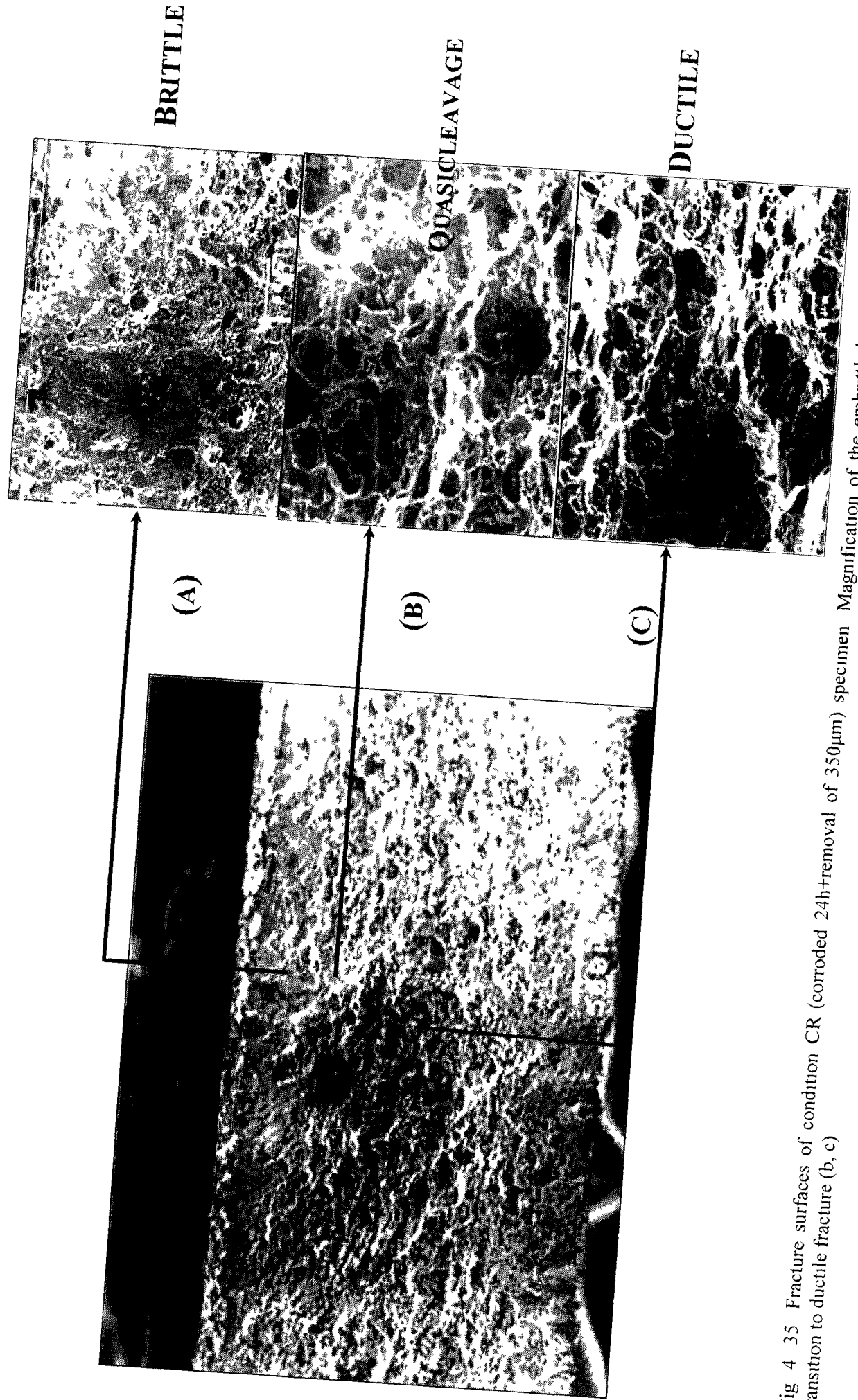


Fig 4 35 Fracture surfaces of condition CR (corroded 24h+removal of 350µm) specimen Magnification of the embrittled region quasicleavage (a), transition to ductile fracture (b, c)

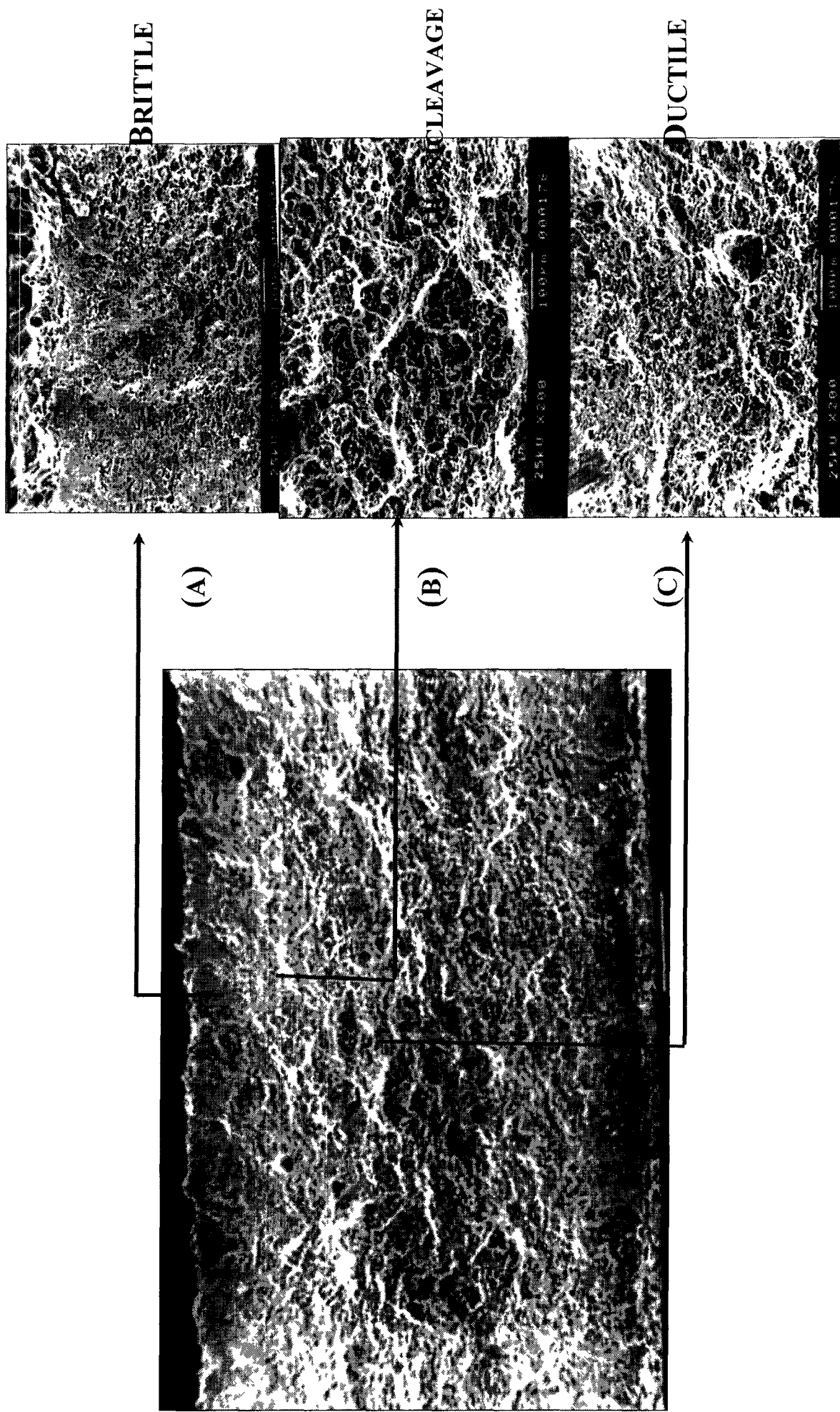
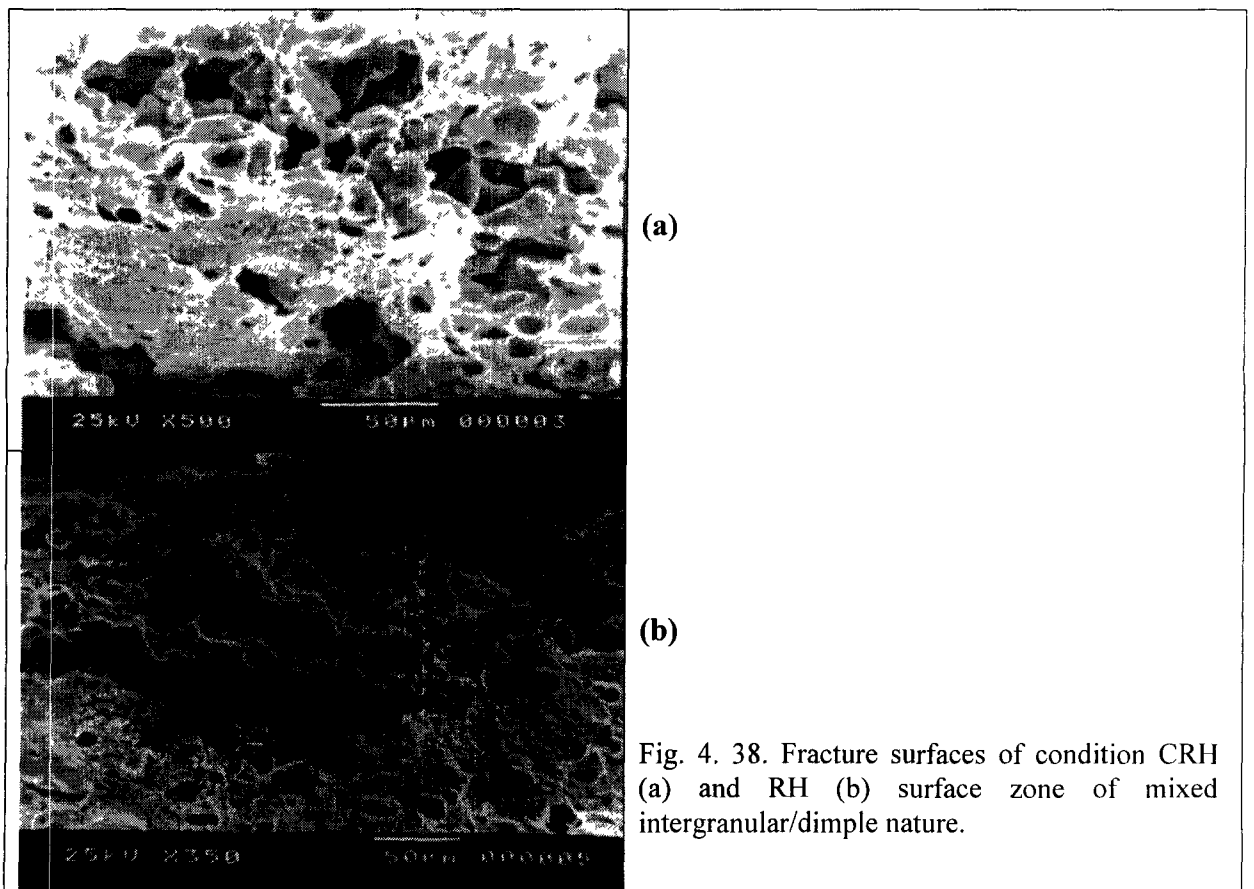
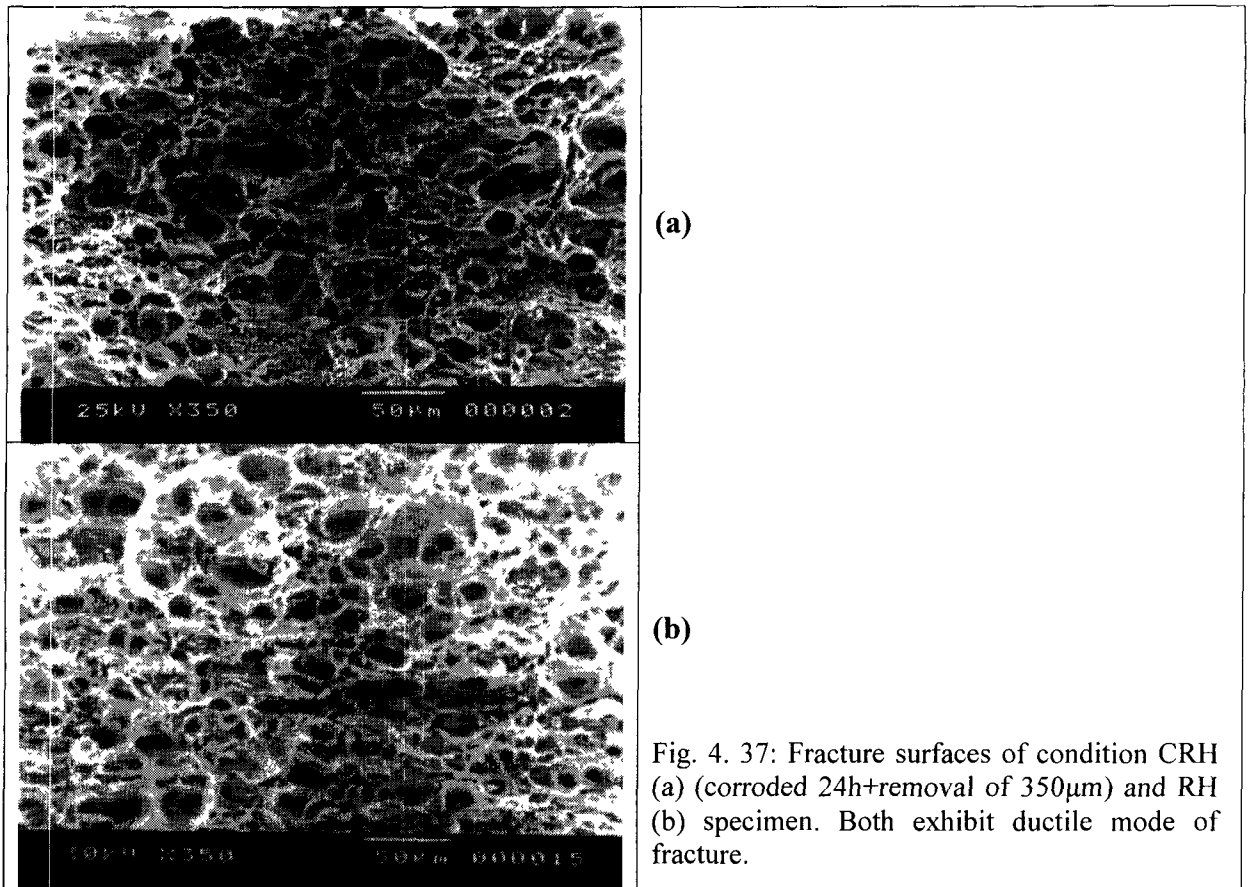


Fig. 4. 36: Fracture surfaces of condition CR (corroded 24h+removal of 350µm). Embrittled zone (a), the transition to ductile (Fig.15b) and the ductile region in the interior of the specimen (Fig.15c).





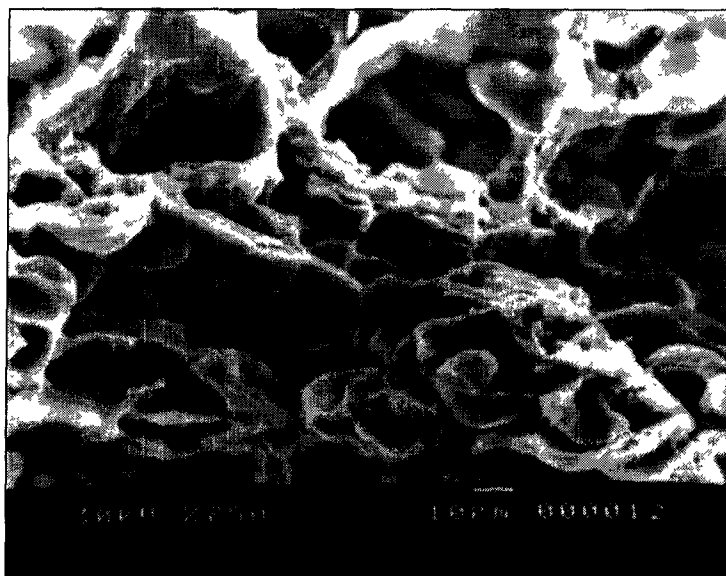
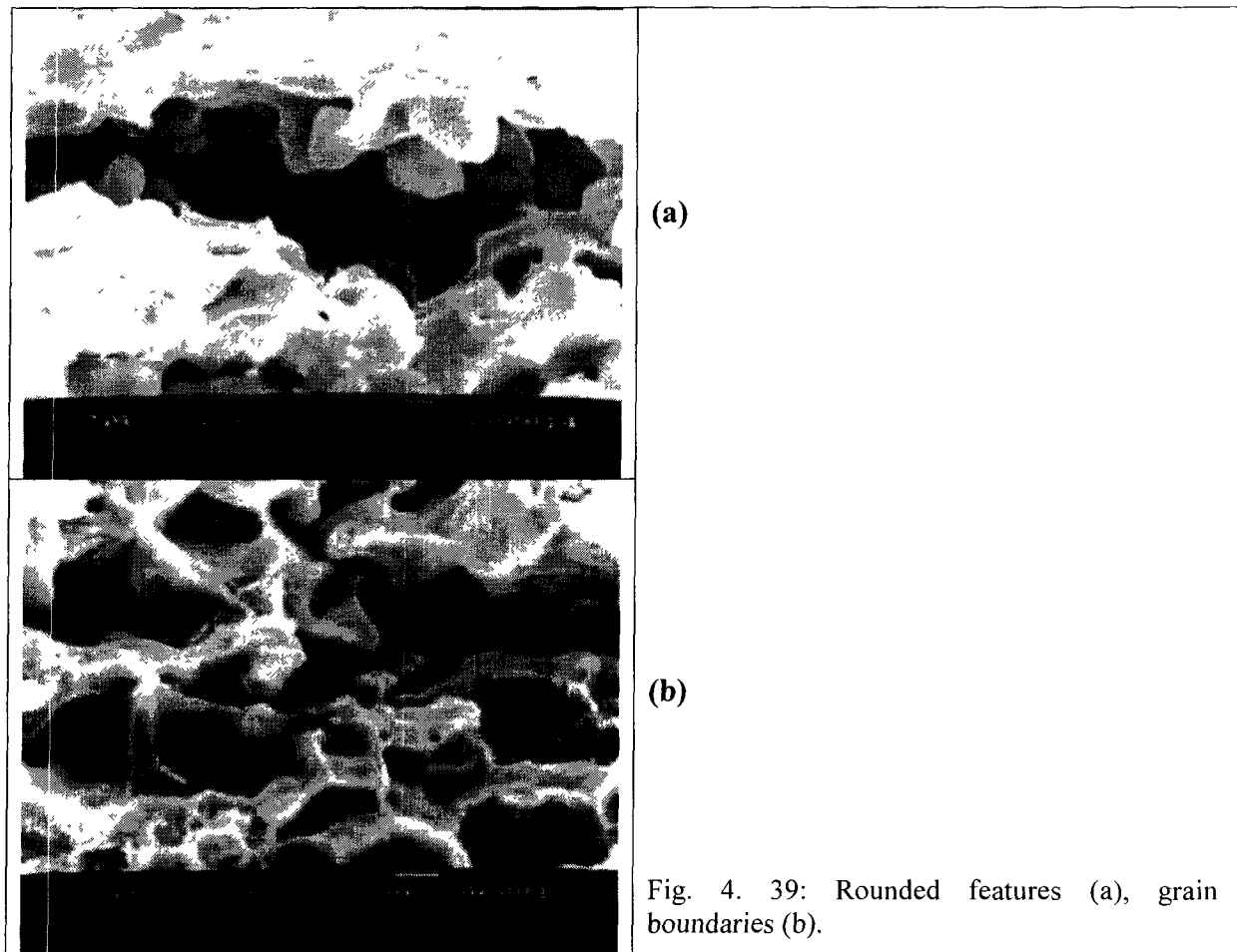


Fig. 4. 40: Fracture surfaces of condition CRH in LT direction intergranular character of the surface zone.

## 4.5 Additional effects in hydrogen uptake

In the following paragraphs the effects of surface area and surface protection on hydrogen uptake is being examined. It should be noted that the results are preliminary in nature and show specific trends, they are by no means conclusive.

### *The relation of specimens surface to hydrogen uptake*

Hydrogen entering the material is produced by the surface reactions of corrosion. Thus, the amount of hydrogen eluting during heating of corroded specimen is expected to correlate better with the surface exposed to corrosive attack rather than with the weight of the specimen. This expectation is confirmed by the data, as in the representative hydrogen evolution spectra of Fig. 4. 41a and b, corresponding to specimens exposed to the EXCO solution for 24 hours. Fig. 4. 41a compares two specimen of the same weight but different surface areas, and demonstrates that larger surface leads to larger amount of trapped hydrogen. Fig. 4. 41b shows that specimens with similar surface areas but very different weights produce similar spectra.

A more extensive compilation of data, which confirms the good correlation between specimens area and hydrogen trapped during corrosion, is shown in Fig. 4. 42. Here, the total quantity of released hydrogen is plotted as a function of the exposed surface area, and a systematic dependence is observed.

A comparative assessment of the above data provided evidence that the side surface (LS) is more active than the flat surface (LT) in promoting corrosion and hydrogen uptake. In order to substantiate this tentative conclusion, a series of specimens were corroded only after their side surface was isolated from the corrosive solution. In this way, the amount of hydrogen measured was associated exclusively with the rolling surface. The material used to seal the side surface was a special resin, which solidifies under vacuum and does not react with the corrosive solution.

A comparison of hydrogen evolution spectra from a specimen with sealed side and a specimen with the entire surface exposed is shown in Fig. 4. 43. It indicates that the side surface is more active than the flat surface as a gate of hydrogen entrance into the material. When the respective areas are taken into account, the relative activities are estimated in the order of 2:1.

The above result is in qualitative agreement with the consideration of grain boundaries as preferential corrosion sites. More specifically, it is well-known that the rolling process produces material grains of relatively uniform dimensions in the LT plane but strongly elongated in the LS plane. Metallographies, of the side and the rolling surface, presented in Fig. 4. 44 indicate that the ratio 2:1 is in reasonable agreement with the grain boundary densities in the two planes.

### *The effect of surface protection*

Two different surface protections were tested for susceptibility to hydrogen uptake, Al cladding and anodizing. Cladding is based on high purity Al (1230) and proved a very efficient means of protection. Fig. 4. 45 shows the difference in hydrogen evolution spectra of two 1.8 thick specimens (one bare the other cladded), subjected to 48 hour exposure to the corrosive solution.

It is very interesting to note that the drastic reduction in hydrogen uptake with cladding, shown in Fig. 4. 45, is demonstrated by specimen with covered rolling surface but bare side surface. The inactive behavior of the side surface is attributed to the creation of an

electrochemical cell between pure Al and the alloy, resulting in the cathodic protection of the specimen. Such behavior is expected to occur whenever bare and Alclad surfaces are electrically connected by the solution, Fig. 4. 46. However, very small amounts of corrosive solution (for example droplets) in contact only with bare material may lead to strong localized corrosion. The protective effect of cladding on hydrogen uptake and embrittlement is further exploited in [98].

Hydrogen measurements in partly anodized specimens showed that hydrogen uptake decreases with respect to non-anodized material. In particular, Fig. 4. 47 compares hydrogen evolution spectra from three specimens, one of which is bare, the other has anodized rolling surfaces and the last has anodized rolling surfaces plus 50% of the side surface. The gradual reduction of measured hydrogen with the percent of surface covered indicates that anodizing is not as efficient as Al-cladding in the protection of partly bare specimens. However, the reduction of measured hydrogen in the specimen with covered rolling surfaces is larger than expected from the relative contributions of rolling and side surfaces of bare material (as discussed in the previous paragraph). Thus, anodizing also appears to offer some synergistic effect, possibly of electrochemical nature.

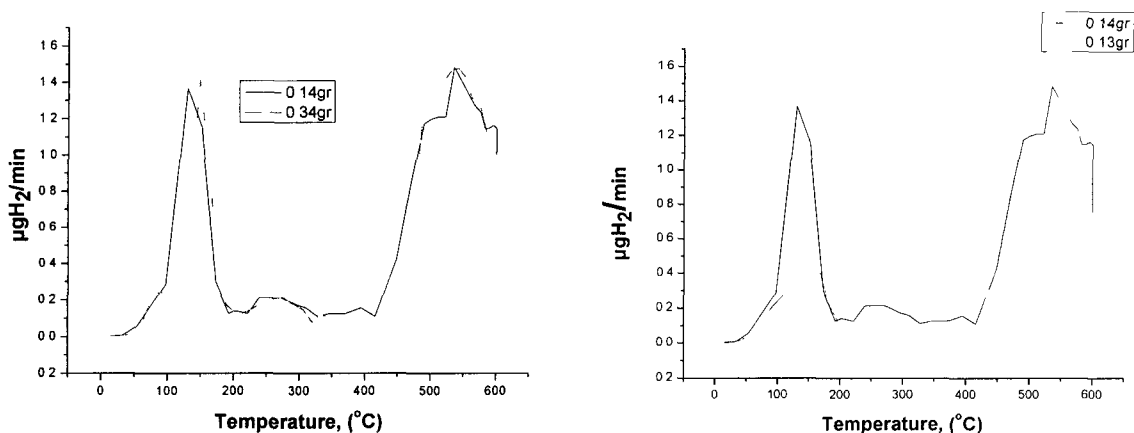


Fig. 4. 41: Specimen with similar total side area (0.34-0.14gr) but different weight (106 versus 116  $\text{mm}^2$ ) Results of hydrogen desorption versus temperature (a). Specimen with similar weight (0.13-0.14gr) but different total side area (106 versus 58 $\text{mm}^2$ ) Results of hydrogen desorption versus temperature (b).

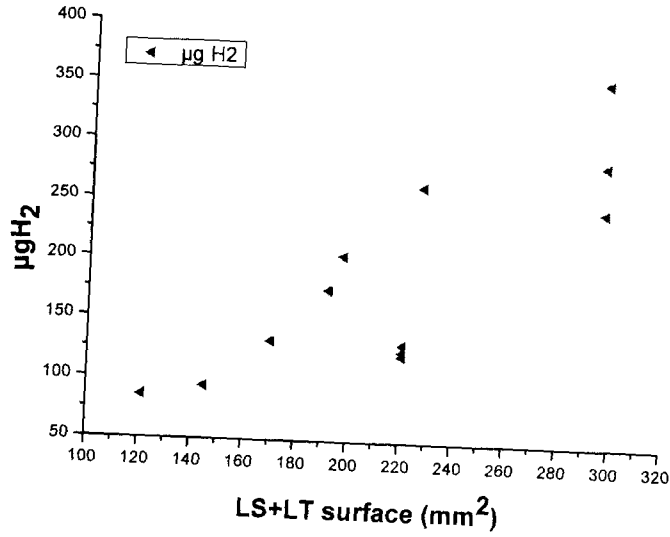


Fig. 4. 42: The results of hydrogen desorption versus the side surface.

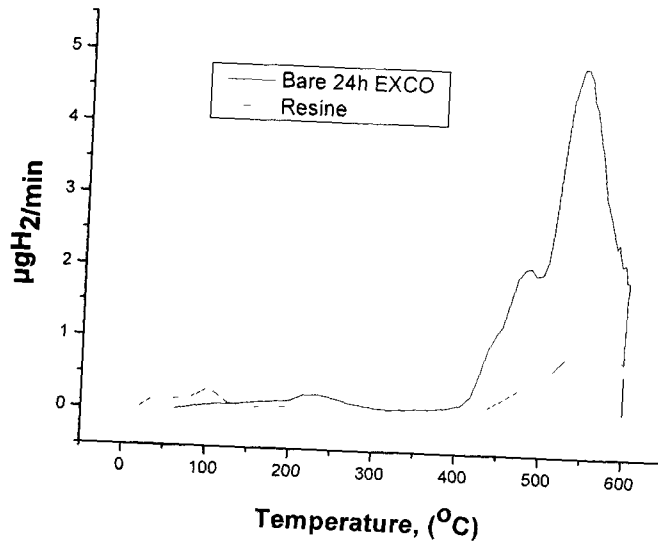


Fig. 4. 43: Comparative diagram with and without resin on the side surface.

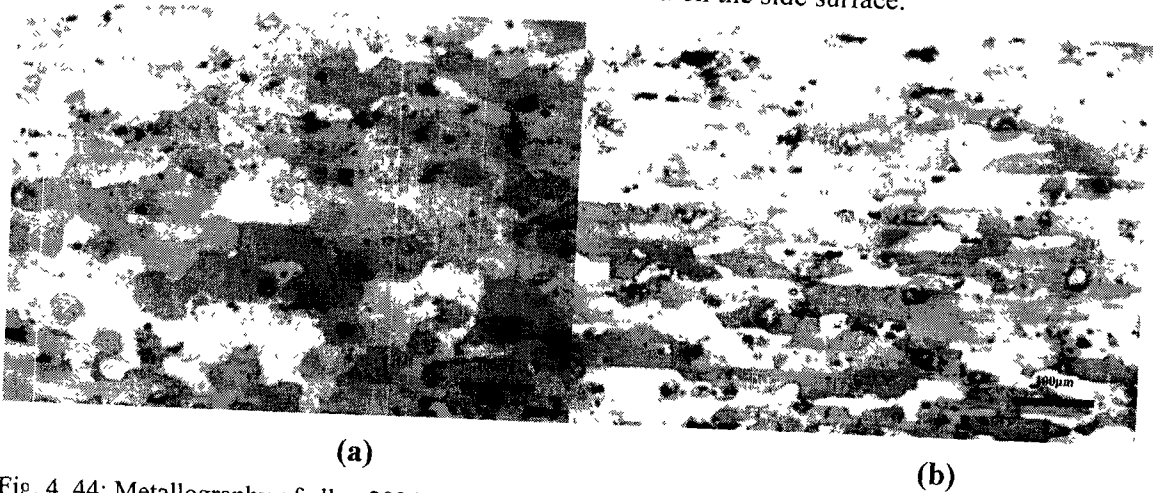


Fig. 4. 44: Metallography of alloy 2024-T3 Bare with thickness of 1,8 mm. (a) Surface of rolling (LT plane). (b) Section vertical to the rolling direction of Fig. 4. 44 (a), (LS plane).

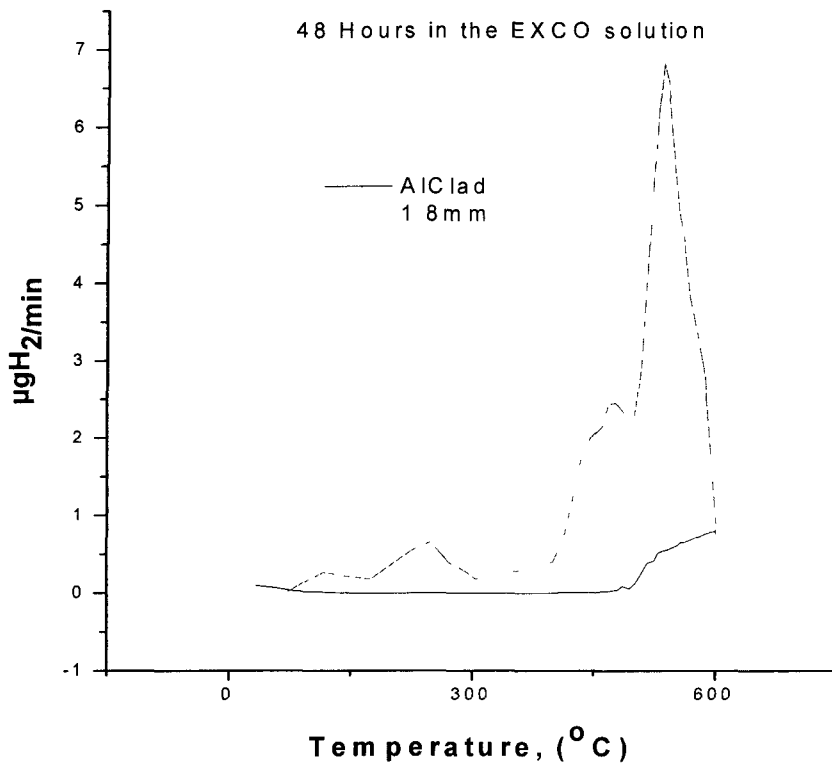


Fig. 4. 45:  $\text{H}_2$  desorption spectra of 2024-T3 Al Clad specimens.

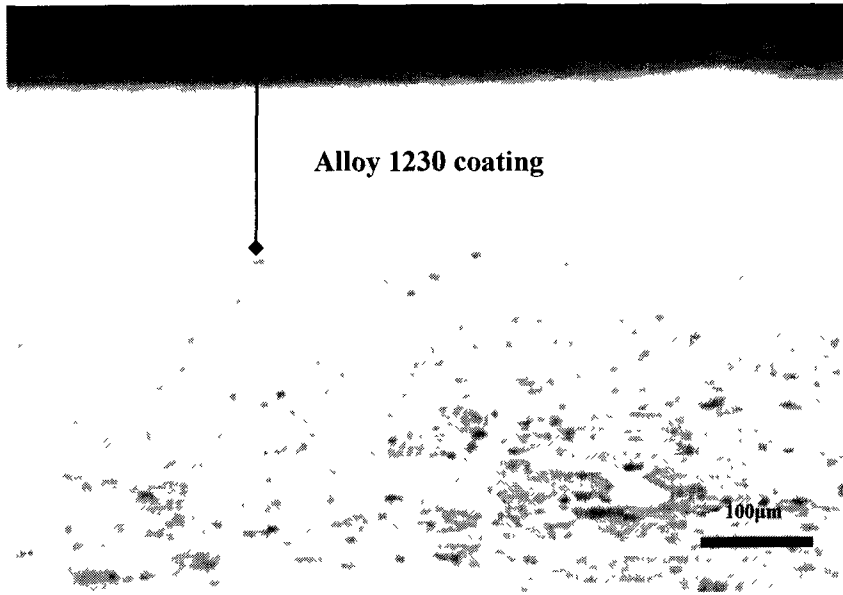


Fig. 4. 46: Metallography of alloy 2024-T3 Al clad (side surface).

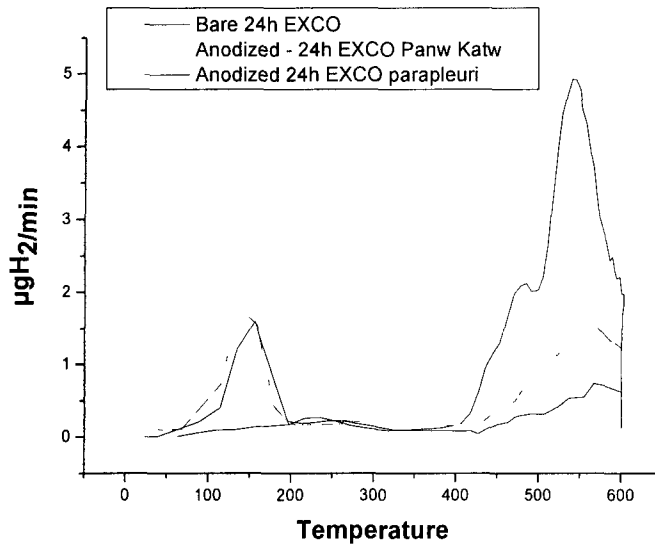


Fig. 4. 47: Effect of anodizing in the side surface of specimen that have suffered corrosion for 24 hours.

## 4.6 Corrosion and Hydrogen uptake of aluminium alloy 6013.

In the framework of the present thesis, in addition to alloy 2024, a preliminary study of alloy 6013 regarding its corrosion and hydrogen uptake behavior was undertaken. The main objective of this work was to see whether 6013 follows similar patterns of behavior, i.e. hydrogen uptake and trapping during corrosion.

Specimens of the alloy were subjected in EXCO accelerated corrosion testing, according to the methodology already described in Chapter 3. The corroded specimens were studied in the AFM in order to determine the evolution of corrosion damage. Finally hydrogen measurements were performed using the thermal desorption – gas chromatography method also employed in the study of 2024 alloy.

### *Evolution of Corrosion Damage*

In comparison to the 2024 alloy, the surface of 6013 corroded for short times (up to 4 hours) exhibits a higher degree of non-uniformity, which is evident even from the uncorroded (as receiver) material Fig. 4. 48, the rolling marks are more intense than in the case of alloy 2024. Pitting, oxide film cracking and rolling marks are present from the beginning of corrosion attack. Fig. 4. 49 shows oxide film cracking for different exposure times. Fig. 4. 50 shows characteristic rolling marks at different exposure times. These marks are more intense than in the case of alloy 2024. Finally Fig. 4. 51 shows pitting corrosion at different exposure times. Pit depth increases with exposure time. Also pit-to-pit interactions and pit clustering are mechanisms that aid the evolution of corrosion damage also in alloy 6013.

For longer exposure times, alloy 6013 shows a higher rate of corrosion attack. Exfoliation of the material is much more rapid compared to alloy 2024.

### *Hydrogen uptake*

Measurements of trapped hydrogen were also undertaken for the aluminum alloy 6013. The main goals in the frame of the present thesis were (1) to confirm the general applicability of the measurement method and (2) to set in perspective the characteristics of alloys 2024 and 6013. The data are presented and discussed in terms of hydrogen evolution spectra. The depth of penetration is also investigated. It is noted however that the results for alloy 6013 are very preliminary and further investigation is needed.

Hydrogen evolution spectra for specimens exposed to the corrosive solution for different times are shown in Fig. 4. 52 a, b. Fig. 4. 52a contains small exposure times and indicates that the onset of hydrogen accumulation is after 4 hours in the exco solution. The behavior for longer exposure times is shown in Fig. 4. 52b and demonstrates a faster buildup of hydrogen in comparison with alloy 2024. These findings are in agreement with the increased severity of corrosion attack, as detected with AFM. They also prove that alloy 6013 permits the entrance into its structure of the hydrogen produced by surface corrosion reactions. The total amount of hydrogen as a function of exposure time is shown in Fig. 4. 52. For exposure beyond 24 hours, the amount decreases and reaches a plateau. This behavior is attributed to the extensive removal of material during corrosion (~30% weight loss) and is an indication of saturation.

The depth of hydrogen penetration was determined as before, by exposing multiple specimens to the same corrosive conditions (4 hours in exco) and removing from each one a different depth of surface material. The respective hydrogen spectra are shown in Fig. 4. 54.



Measurement of an uncorroded specimen is included for comparison. The results demonstrate the expected decrease in hydrogen content with depth and indicate a penetration depth around 250  $\mu\text{m}$ . Considering that diffusion depth is proportional to the square root of time, this number compares favorably to the estimated penetration depth in alloy 2024 ( $\sim 500 \mu\text{m}$ ), which resulted from a 24 hour exposure.

A tentative conclusion from a comparison of the behavior of alloys 2024 and 6013, concerning hydrogen penetration, is the following: the significance of hydrogen embrittlement in relation to the direct corrosion damage may depend inversely on the corrosion resistance of the alloy. Thus, a weaker alloy (like 6013 in the specific exco environment) corrodes faster and shows direct evidence of extensive damage before the surface hydrogen has enough time to penetrate deeply into the material. On the contrary, a more resistant alloy (like 2024) still produces enough high-fugacity surface hydrogen to favor hydrogen charging. When exposed to the corrosive environment for a long time, the direct corrosion damage is not detrimental but hydrogen has enough time to penetrate deeper into the material and cause extensive embrittlement.

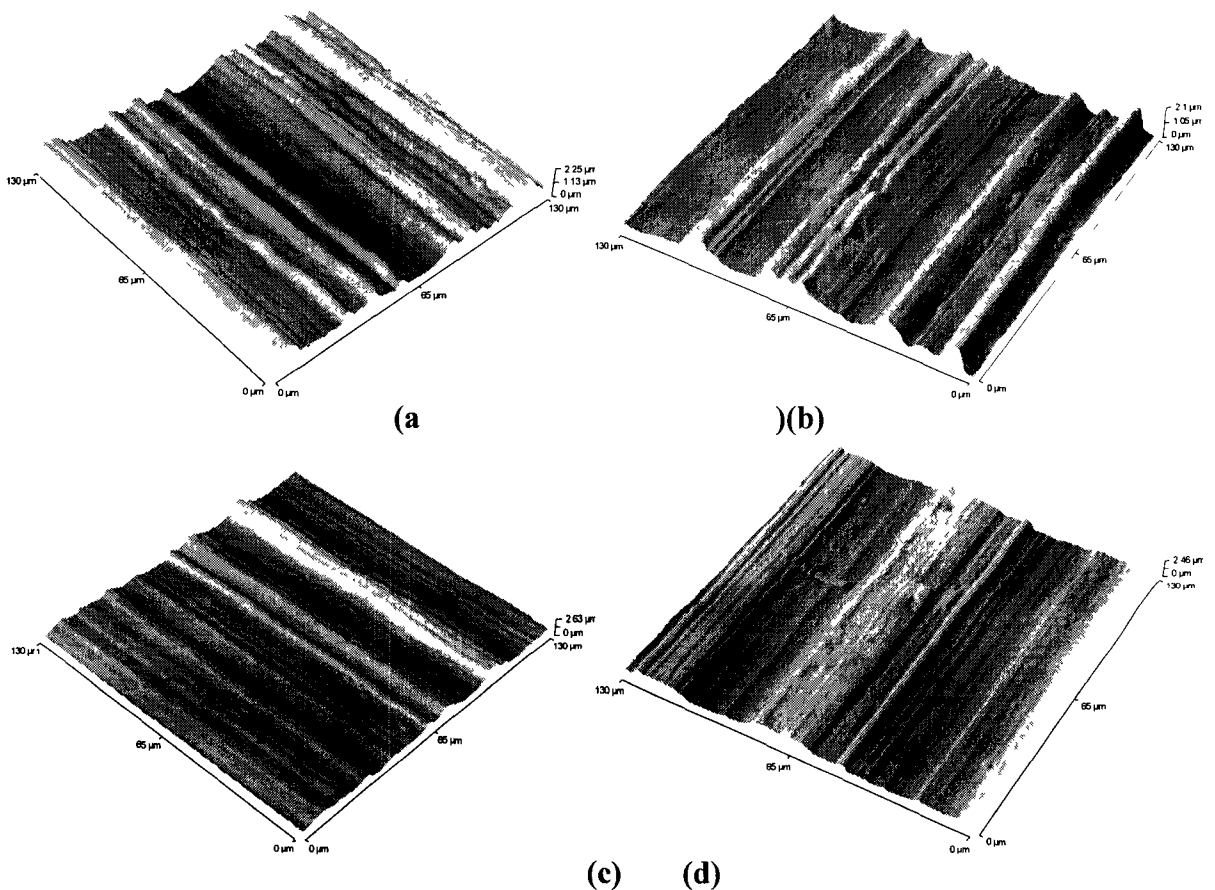


Fig. 4. 48: AFM topographies for the as received aluminum alloy 6013, LT plane. (a) through (d).

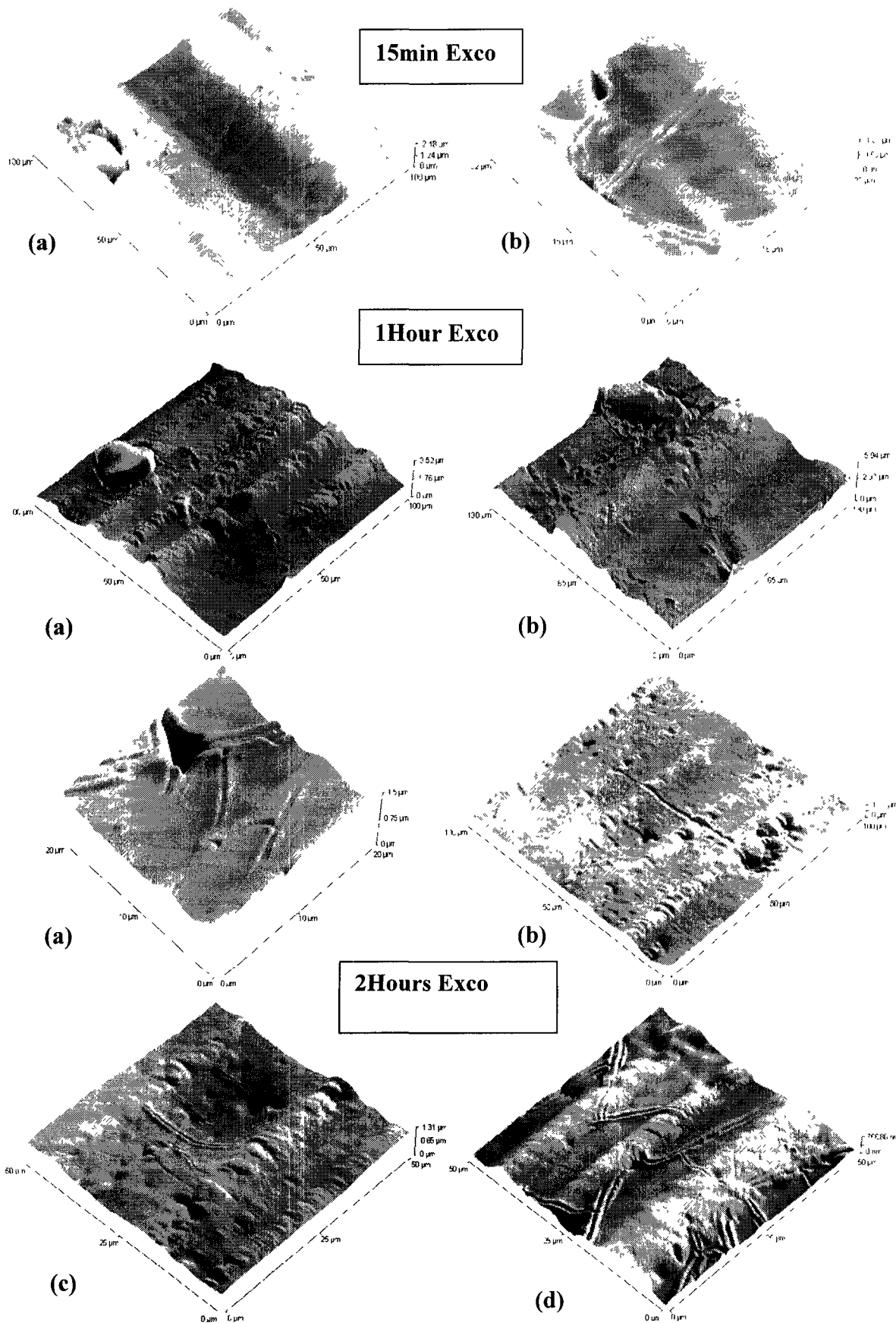


Fig. 4. 49: Alloy 6013-T6 (LT plane), for different exposure times in the corrosive solution EXCO. Fragmentation and spaling of surface oxide.

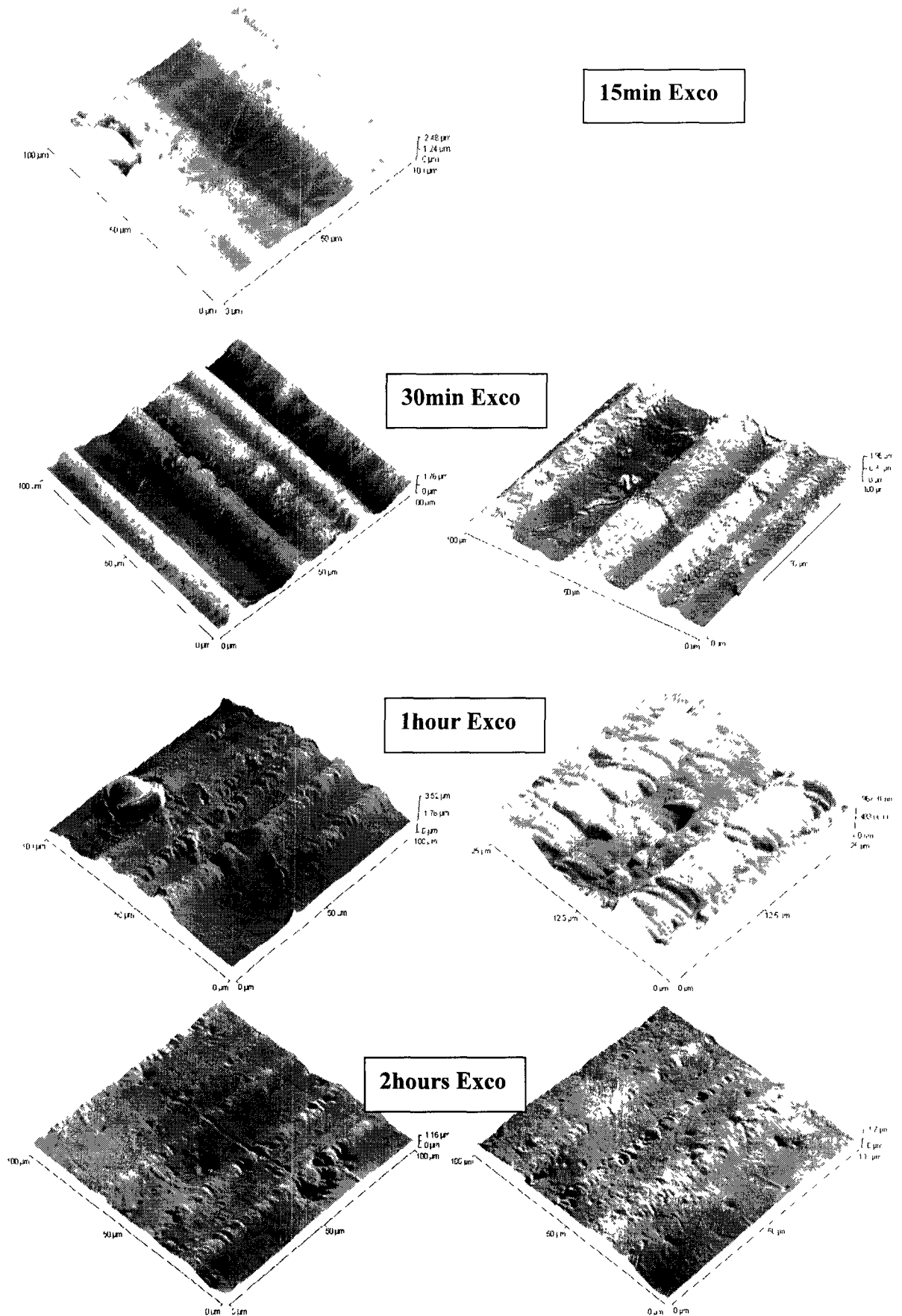


Fig. 4. 50: Alloy 6013-T6 (LT plane), for different exposure times in the corrosive solution EXCO. Characteristic rolling marks at different exposure times.

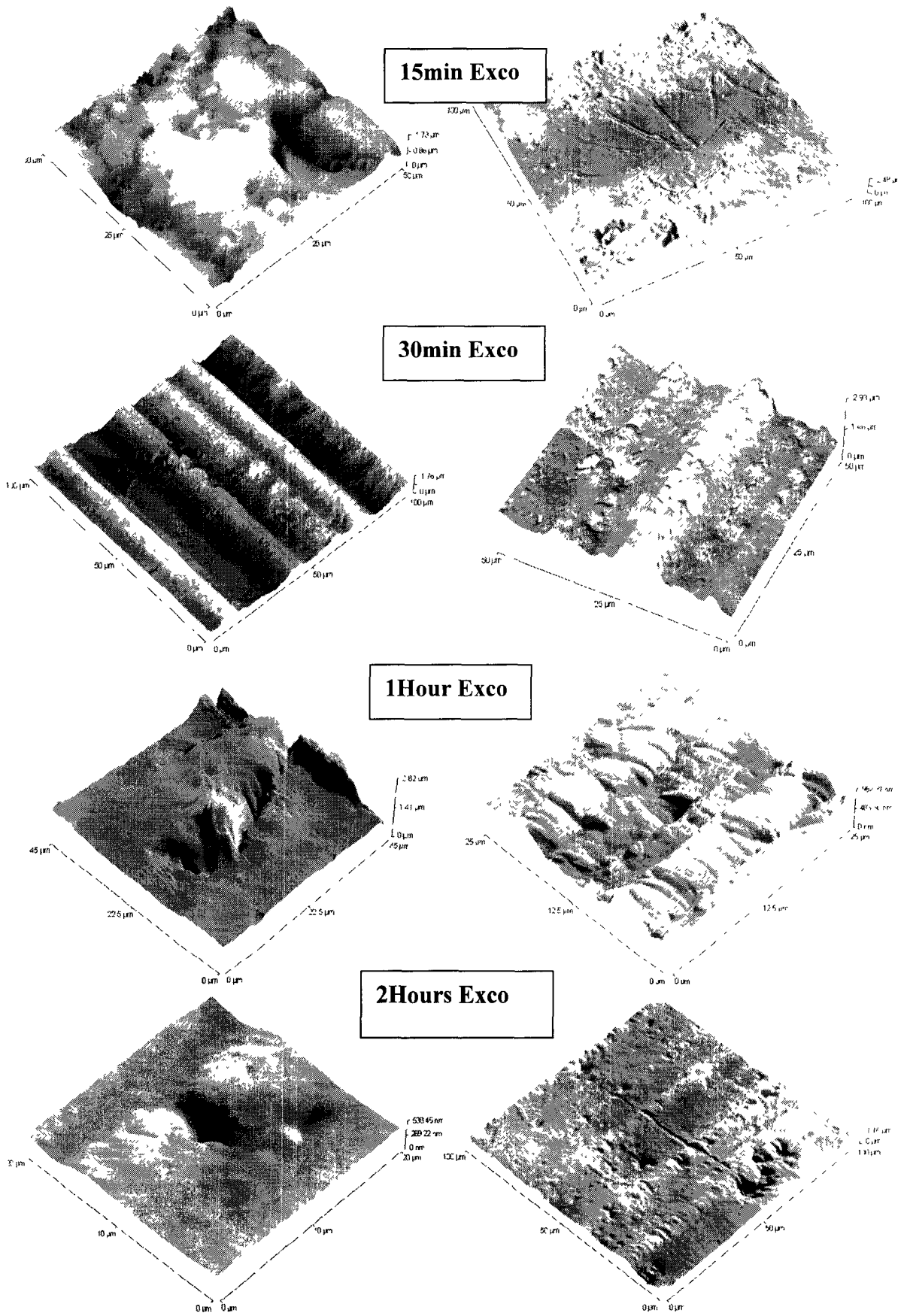
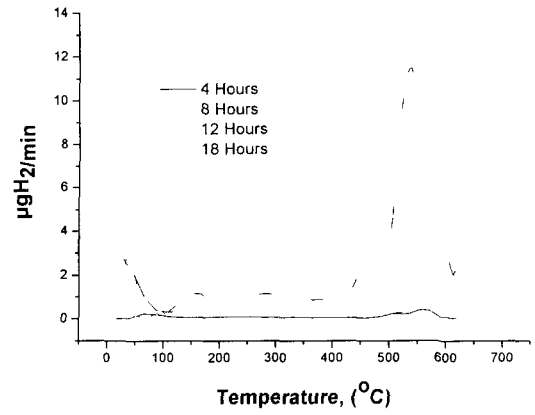
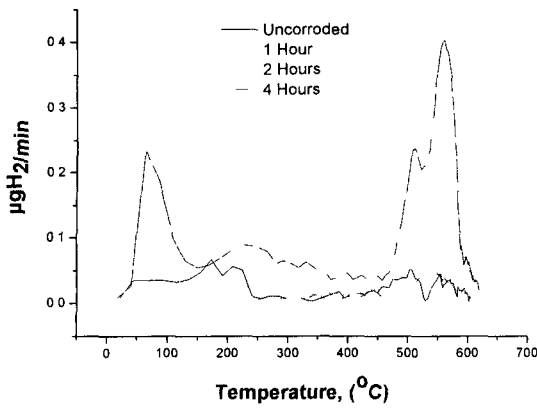


Fig. 4. 51: Alloy 6013-T6 (LT plane), for different exposure times in the corrosive solution EXCO, pitting corrosion.



(a)

(b)

Fig. 4. 52: (a) Hydrogen desorption spectra for specimen of alloy 6013 for exposure to exco 0 to 4 hours (b) Hydrogen desorption spectra for specimen of alloy 6013 for exposure to exco 4 to 18 hours

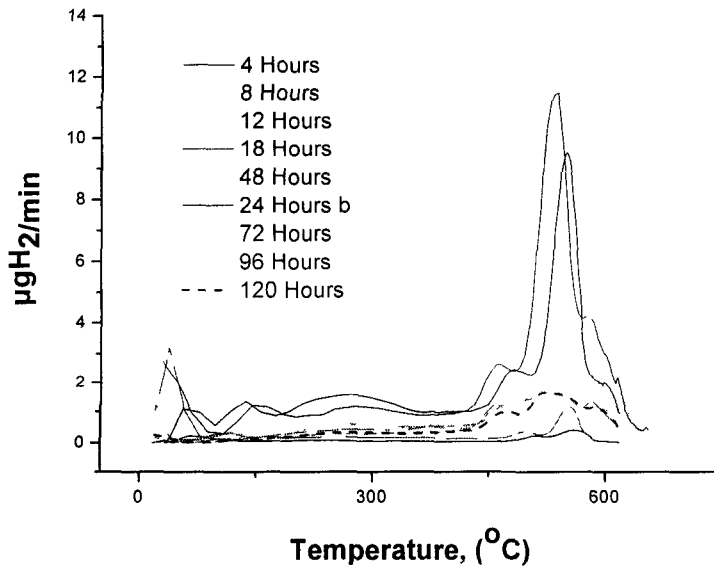


Fig. 4. 53: Hydrogen desorption spectra for specimen of alloy 6013 for exposure to exco 4 to 120 hours.

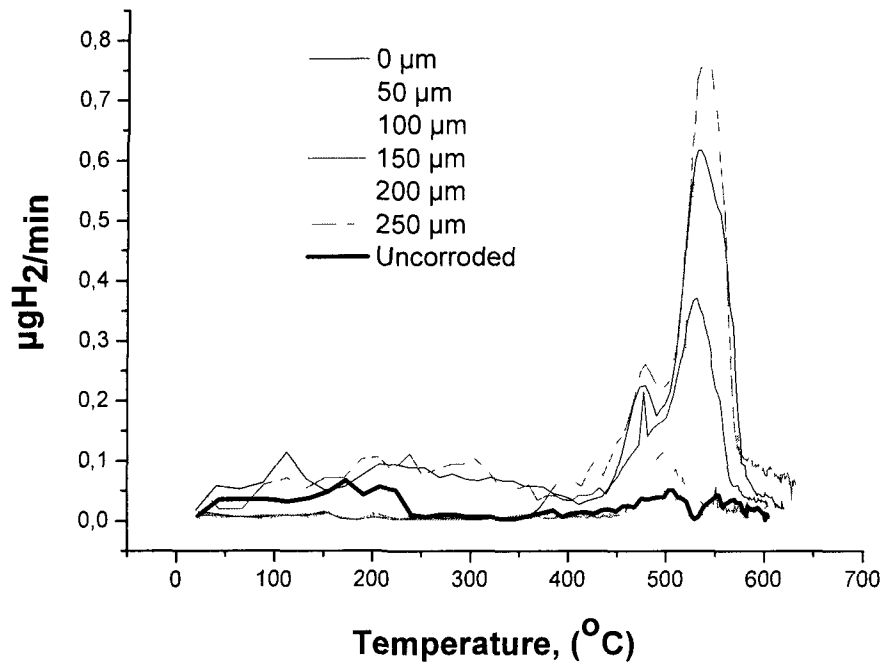


Fig. 4. 54: H<sub>2</sub> evolution as a function of temperature for specimens with varying removal depth

# Chapter 5 – Concluding Discussion

The objectives of this thesis as stated in the beginning were the following:

- To establish a link between corrosion and hydrogen trapping
- To provide an understanding of the observed embrittlement

It should be stated that the starting point was the fact that the alloy is being embrittled when subjected to accelerated corrosion testing. Furthermore, a significant part of ductility was restored after removal of the surface corrosion layer. It was apparent from the start that the main point would be to clarify whether the observed embrittlement is actually related to hydrogen or is the result of other corrosion-induced processes. The experimental procedure applied so far generated a series of data that provide evidence of hydrogen embrittlement in the aircraft aluminium alloy 2024. In this section, an effort is being made to link the main results together, in order to reach to the conclusions of this thesis and to discuss the major implications of these conclusions in aircraft design and maintenance.

The main results of this thesis are the following:

## *Corrosion*

Alloy 2024-T3 was subjected to accelerated corrosion testing. The EXCO test, used extensively by the aeronautical industry, was selected. Exposure times in the EXCO solution ranged from 15min to 96 hours. The early stages of corrosion (up to 4 hours) were studied by AFM, while the later stages by SEM and metallographic sectioning. Corrosion in this alloy starts in the form of pitting. With exposure time pits become deeper and pit clustering takes place. At 2-4 hours a type of pit-to-pit interaction initiates the process of intergranular corrosion. This type of corrosion has two major consequences. The first is the exfoliation of grains from the surface of the alloy. The second is the opening of paths for the corrosion solution to penetrate in the material interior. It appears that this is the way for hydrogen to reach deep in the material. Hydrogen is generated during corrosion. Then it diffuses in the alloy. It creates a diffusion zone adjacent to the corrosion zone.

## *Hydrogen uptake and trapping*

An in-house thermal desorption – gas chromatography system was employed in order to measure hydrogen being trapped in the alloy during corrosion. A constant heating rate was applied to the corroded alloy and the amount of hydrogen evolved was measured as a function of temperature. It was found that hydrogen is being trapped in distinct energy states, which correspond to different microstructural traps that are being activated at different temperatures. The higher the temperature the stronger the trap. In 2024 alloy, four traps T1 to T4 were identified. The low temperature trap T1 is the weaker reversible trap and corresponds to

hydrogen being trapped in interstitial sites and dislocations. Microhardness measurements performed after subjecting the material to the same thermal cycle used for the hydrogen measurements showed that the corroded material becomes softer in accordance to theories of hydrogen-induced softening stemming from interaction of hydrogen and dislocations. Evolution of hydrogen from the high temperature trap T4 coincides with dissolution of the strengthening phase, indicating that T4 hydrogen is trapped in the strengthening phase.

Another key question answered by these experiments was how deep in the material is hydrogen introduced. Sequential sectioning provided the hydrogen profile and showed that the hydrogen zone extends below the corrosion zone. This means that since hydrogen is generated during corrosion, it reaches to the same depth with corrosion plus a further depth due to diffusion. Actually fractographic analysis of tensile specimens (to be discussed below) showed the existence of quasicleavage (embrittled) zones just below the intergranular fracture zones (corrosion) in the otherwise dimple fractured (ductile) alloy.

### ***Mechanical testing and fractography***

In order to link corrosion and hydrogen trapping to strength and ductility, results from tensile testing of corroded samples and corresponding fractographic analysis took place. Corroded material (24h EXCO) has a yield strength 92% and an elongation 39% that of the uncorroded material. Removal of the corrosion layer restores the yield strength to 100% , while ductility is only partially restored to 66% that of the reference value. This means that an embrittling mechanism still remains in the material even after all surface damage due to corrosion has been removed. Removal of the corrosion layer followed by heating at 495°C restores both the yield strength and elongation to almost 99% of the reference value. The complete restoration of ductility is attributed to hydrogen desorption by the activation of all hydrogen traps in the alloy. These conditions are shown schematically in Fig. 4. 55.

The 24 hours EXCO corrosion creates damage which penetrates in a nonuniform way from the surface to the interior of the material. The depth of attack is 350µm. Below the corrosion layer, a hydrogen zone is established due to the diffusion of hydrogen created by the corrosion process. Removal of the corrosion layer (equal to the depth of attack), removes all the corrosion damage and all hydrogen trapped in the 350µm surface layer in the alloy. The result is an elongation increase to 66% of the reference value. However, part of the hydrogen zone still remains. The heating of the alloy to 495°C (at the T4 state) removes all hydrogen from that zone by desorption and restores all ductility back to the original value. Fractography of the tensile samples showed that below the intergranular fracture zone at the surface, which is due to corrosion, there is a quasicleavage transition zone before the fracture mode turns to the ordinary dimple ductile fracture of the unaffected material. This quasicleavage zone has been embrittled by hydrogen diffusion and trapping. Removal of that hydrogen by heating restores all ductility. These results provide the first evidence of hydrogen embrittlement in 2024 alloy.



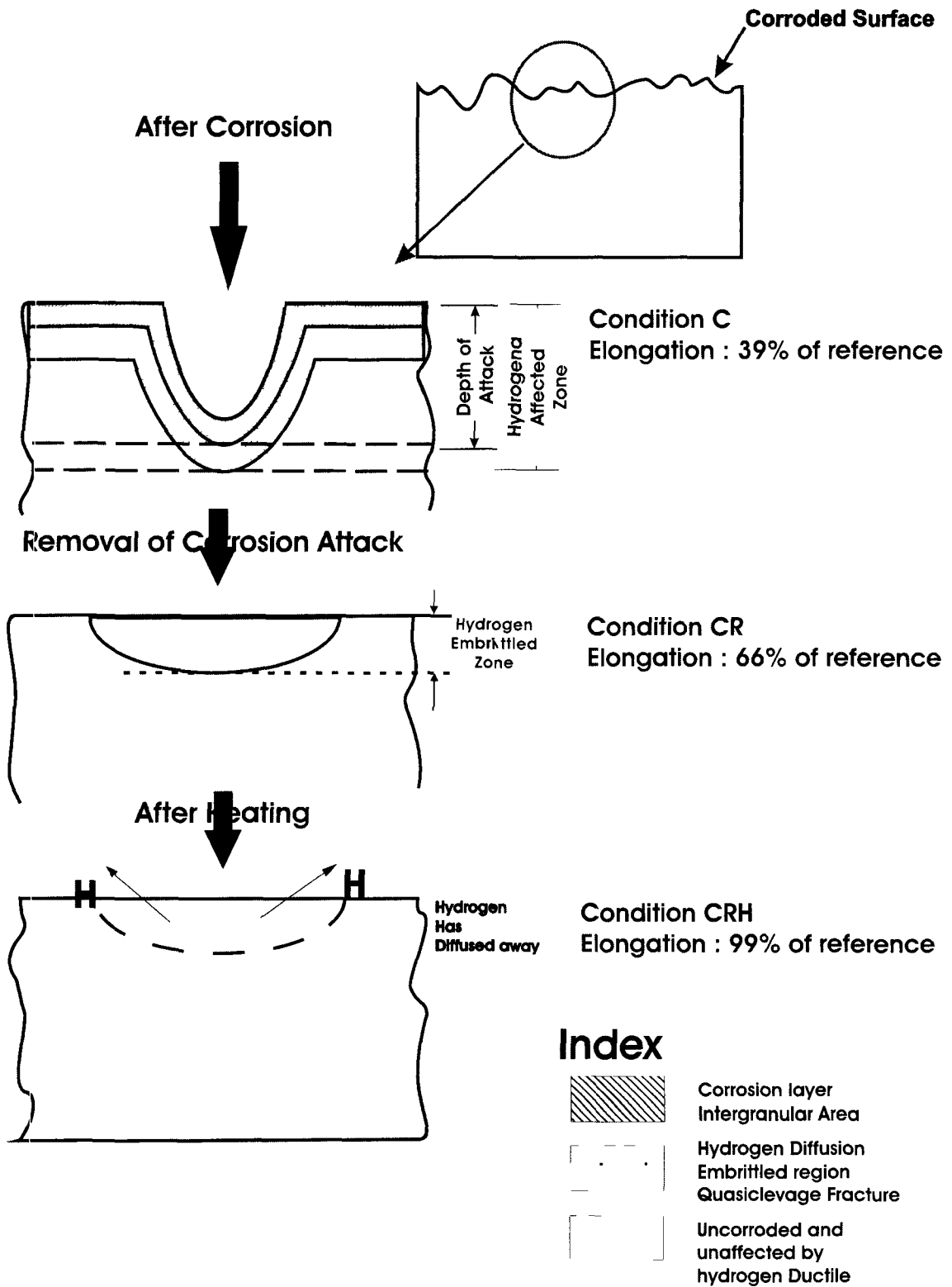


Fig. 4. 55: Schematic representation of the corrosion layer and the hydrogen affected area beneath it. After removal of the corroded layer, a hydrogen affected zone (free of corrosion) remains and affects the mechanical properties of the material (elongation 66% of reference). Heating releases trapped hydrogen and restores elongation to 99% of reference.

### ***Effect of side surface (LS) relative to the flat surface (LT)***

Hydrogen measurements performed in specimens of the same weight but different surface area of the side surface (LS side) showed that hydrogen uptake during corrosion increases with the surface area of the LS side. Actually more hydrogen enters the material through the LS side than from the LT side. This is attributed to the higher density of grain boundaries in the LS side, which comes from the rolling of the material.

### ***Effect of cladding***

Hydrogen measurements in Alclad material (2024 alloy claded with 1230 alloy) which has also been exposed in EXCO solution showed that hydrogen uptake in Alclad is negligible compared to the bare (unprotected) material. This is probably due to the cathodic protection offered by the cladding. Corrosion inhibition also prevents hydrogen uptake. The effect of cladding on hydrogen embrittlement is exploited further in [98].

### ***Effect of anodizing***

Hydrogen measurements in anodized specimens showed that hydrogen uptake decreases with respect to non-anodized material. The reduction is higher if the side surface (LS) is also anodized.

The above results on the effect of cladding and anodizing indicate that these two forms of corrosion protection also lead to a reduction of hydrogen uptake and trapping in alloy 2024.

### ***Implications in design and maintenance***

Today's aircraft design and maintenance follows the damage tolerance philosophy. According to this practice, flaws or cracks are allowed in the structure once they are tolerated by the material. Tolerance depends on the fracture toughness of the alloy. The cracks grow by fatigue. The life of the structure depends (i) on the prescribed damage tolerance and (ii) on the fatigue crack growth rate. Both of these factors are influenced by corrosion and hydrogen embrittlement. The present thesis sheds light at the degradation of ductility and hence fracture toughness, due to the corrosion-induced hydrogen embrittlement, which reduces the damage tolerance of the structure. These arguments are particularly important for the so-called "aged aircraft", which has exceeded or is near the operational lifetime, but it is still operated by the airlines. These aircrafts have accumulated damage and corrosion. The damage tolerance of the material has decreased due to hydrogen embrittlement, at least locally in critical areas such as rivet holes, in accordance with the 'local fracture toughness' concept proposed in [13]. This condition is shown in Fig. 4. 56, where the situation around rivet holes is considered to be analogous to that of Fig. 4. 55. the critical situation will appear if crack extension occurs in the hydrogen embrittled region, where, locally, damage tolerance has been reduced. These conditions call for a re-determination of lifetime, if the decision is to extend the operational lifetime of such aircrafts.

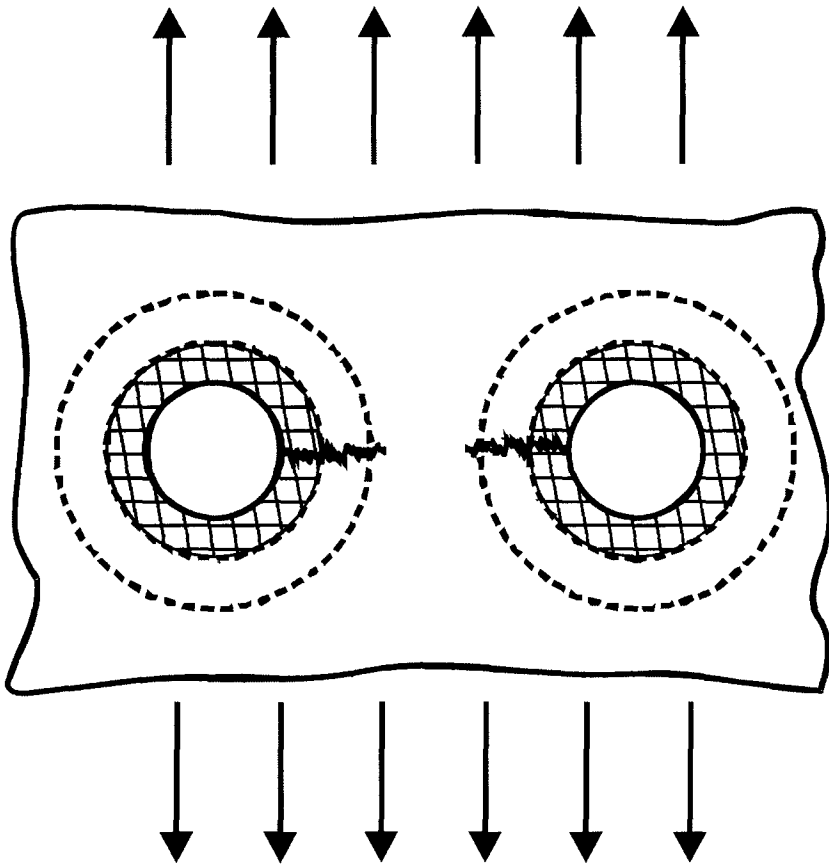


Fig. 4. 56: The situation around two adjacent rivet holes. The concentric cycles around the hole represent the corroded area around the hole and the hydrogen affected zone.

# Chapter 6 – Conclusions

The experiments performed in this thesis, the analysis of results and the discussion in the previous chapter led to the following conclusions regarding corrosion-induced hydrogen embrittlement in aircraft Al-alloys:

1. The alloy has been subjected to the EXCO accelerated corrosion test. Corrosion damage in the alloy starts with pitting and develops to a network of intergranular corrosion leading to exfoliation of material. Pit-to-pit interaction and pit clustering are mechanisms aiding the development of corrosion damage. The depth of attack increases with exposure time. Typical value for depth of attack is 350 $\mu$ m for 24h of exposure time.
2. Hydrogen is produced during the corrosion process and is being trapped in distinct energy states, which correspond to different microstructural traps. These traps are activated and liberate hydrogen at different temperatures. In alloy 2024, four traps T1 to T4 were identified. Trap T1 is considered to be a reversible trap, which liberates hydrogen continuously at low temperatures. Traps T2, T3 and T4 saturate with exposure time and are considered to be irreversible.
3. Trapping state T1 corresponds to hydrogen at interstitial sites. The observed material softening at the same temperature range of T1 activation correlates with theories of hydrogen-induced softening stemming from dislocation-hydrogen interactions. Trapping state T4 is the strongest trap and its temperature range corresponds to the dissolution of the strengthening precipitate in alloy 2024.
4. The hydrogen front advances with the corrosion front, so hydrogen penetrates deep in the material through the intergranular paths generated by the corrosion process. Then hydrogen diffuses further in the material establishing a hydrogen-affected zone beneath the corrosion depth of attack.
5. Removal of the corrosion layer (equal to the depth of attack) leads to complete restoration of yield strength and partial restoration of ductility. Removal of the corrosion layer and heating above the T4 activation range (to activate all traps) leads not only to complete restoration of strength but also to complete restoration of ductility.
6. Detailed fractographic analysis showed the existence of a quasicleavage transition zone between the intergranular corrosion zone and the ductile corrosion-unaffected material. This quasicleavage zone has been embrittled by hydrogen diffusion and trapping. Removal of hydrogen by heating restores all ductility. These results constitute evidence of hydrogen embrittlement in Al-alloy 2024.

7. Additional effects investigated included the effect of side surface, cladding and anodizing ad also alloy 6013. Preliminary results indicated that more hydrogen enters the material from the LS side (side surface) than the LT side (rolling plane), probably due to the higher density of grain boundaries in the LS side. Both forms of corrosion protection, cladding and anodizing reduced considerably hydrogen uptake and trapping. Regarding the behavior of alloy 6013, the evolution of corrosion damage follows a similar pattern as for alloy 2024. However corrosion in 6013 is more intense and intergranular corrosion and exfoliation appear in shorter exposure times. Hydrogen is also produced during corrosion and is being trapped in the alloy at distinct energy states.

# Chapter 8 – Proposed Future Work

Taking into consideration the conclusions reached with this thesis the following items are proposed for further investigation:

1. Corrosion-induced hydrogen embrittlement study of other heat-treatable Al-alloys of the 6xxx and 7xxx series
2. Corrosion-induced hydrogen embrittlement study using a more mild accelerated corrosion test procedure, such as salt spray or artificial seawater test.
3. Detailed microstructural investigation in order to determine the nature of hydrogen traps and their relation with the dislocation structure in the material

# Chapter 7 – References

1. AGARD Workshop. Fatigue in the Presence of Corrosion. 1998, 5-9 October. Corfu, Greece.
2. BRITE / EURAM No. 1053. Structural Integrity for the Next Millennium in ICAF '99 Conference. 1999. Bellevue, WA.
3. FAA-NASA. Symposium on the Continued Airworthiness of Aircraft Structures. 1996. Atlanta, Georgia: National Technical Information Service, Springfield.
4. Chang, J. B., M. Szamossi, and K. W. Lin, Methods and Models for Predicting Fatigue Crack Growth under Random Loading, in ASTM STP 748, ASTM, Editor. 1981: Philadelphia. p. 115.
5. Zhang, X., A. S. L. Chan, and G. A. O. Davis, Eng. Mech., 1992. 42: p. 305.
6. Sih, G. C. and D. Y. Jeong, Fatigue load sequence effect ranked by critical available energy density. J. Theor. Appl. Fract. Mech, 1990. 14: p. 141-151.
7. Pantelakis, S. G., A. T. Kermanidis, and P. G. Daglaras, Crack-growth analysis code for assessing fatigue life of 2219-T851 aluminum specimens under aircraft structure service spectra. J. Theor. Appl. Fract. Mech., 1997. 28: p. 1-12.
8. Speidel, M. O., Hydrogen embrittlement and stress corrosion cracking of aluminum alloys, in Hydrogen Embrittlement and Stress Corrosion Cracking, R. Gibala and R.F. Heheman, Editors. 1992, ASM: Materials Park, OH., p. 271-296.
9. de Jong, H. F., Influence of environmental and temperature on the stress corrosion crack growth rate of aluminum 7075. Aluminum, 1982. 58: p. 526-531.
10. Inman, M. E., R. G. Kelly, S. A. Willard, and R. S. Piascik. Coordinated metallographic, chemical and electrochemical analyses of fuselage lap splice corrosion in FAA-NASA Symposium on the Continued Airworthiness of Aircraft Structures. 1996. Atlanta, Georgia: National Technical Information Service, Springfield, Virginia.
11. Pantelakis, S. G., N. I. Vassilas, and P. G. Daglaras, Effect of corrosive environment on the mechanical behavior of the advanced Al-Li alloys 2091 and 8090 and the conventional aerospace alloy 2024. METAL, 1993. 47: p. 135-141.
12. Pantelakis, S. G., P. G. Daglaras, and C. A. Apostolopoulos, Tensile and energy density properties of 2024, 6013, 8090 and 2091 aircraft aluminum alloy after corrosion exposure. J. Theor. Appl. Mech., 2000. 33: p. 117-134.
13. Kermanidis, A. T., Phd Thesis, Department of Mechanical Engineering and Aeronautics. 2003, University of Patras, Greece.
14. Shih, H.-C., N.-J. Ho, and J. C. Huang, Precipitation behaviors in Al-Cu-Mg and 2024 aluminum alloys. Metallurgical and Materials Transactions A, 1996. 27A: p. 2479-2494.
15. Bigot, A., F. Danoix, P. Auger, D. Blavette, and A. Menand, 3D reconstruction and analysis of GP zones in Al-1.7Cu (at%): A tomographic atom probe investigation. Applied Surface Science, 1996. 94/95: p. 261-266.
16. Karlik, M. and B. Jouffrey, High resolution electron microscopy study of Guinier-Preston (GP1) zones in Al-Cu based alloys. Acta Materialia, 1997. 45(8): p. 3251-3263.
17. Karlik, M., B. Jouffrey, and S. Belliot, The copper content of Guinier-Preston (GP1) zones in Al-1.84 at.% Cu alloy. Acta Materialia, 1998. 46(5): p. 1817-1825.

- 18 Charai, A., T. Walther, C. Alfonso, A.-M. Zahra, and C. Y. Zahra, Coexistence of clusters, GPB zones, S''-, S'- and S-phases in an Al-0.9% Cu-1.4% Mg alloy. *Acta Materialia*, 2000. 48(10): p. 2751-2764.
- 19 Radmilovic, V., R. Kilaas, U. Dahmen, and G. J. Shiflet, Structure and morphology of S-phase precipitates in aluminum. *Acta Materialia*, 1999. 47(15-16): p. 3987-3997.
- 20 Ringer, S. P. and K. Hono, Microstructural evolution and age hardening in Aluminium Alloys; Atom Probe Field-Ion Microscopy and Transmission Electron Microscopy Studies. *Materials Characterization*, 2000. 44(1-2): p. 101-131.
- 21 Ringer, S. P., B. C. Muddle, and I. J. Polmear, Effects of cold work on precipitation in Al-Cu-Mg-(Ag) and Al-Cu-Li-(Mg-Ag) alloys. *Metallurgical and Materials Transactions A*, 1995. 26A: p. 1659-1671.
- 22 Skrotzki, B., G. J. Shiflet, and E. A. Starke, JR., On the effect of stress on nucleation and growth of precipitates in an Al-Cu-Mg-Ag alloy. *Metallurgical and Materials Transactions A*, 1996. 27A: p. 3431-3444.
- 23 Ringer, S. P., K. Hono, I. J. Polmear, and T. Sakurai, Precipitation processes during the early stages of ageing in Al-Cu-Mg alloys. *Applied Surface Science*, 1996. 94(95): p. 253-260.
- 24 Ringer, S. P., I. J. Polmear, and T. Sakurai, Effect of additions of Si and Ag to ternary Al-Cu-Mg alloys in the  $\alpha$ +S phase field. *Materials Science & Engineering A*, 1996. 217/218: p. 273-276.
- 25 Ringer, S. P., T. Sakurai, and I. J. Polmear, Origins of Hardening in Aged Al-Cu-Mg-(Ag) Alloys. *Acta Materialia*, 1997. 45(9): p. 3731-3744.
- 26 Ringer, S. P., G. C. Quan, and T. Sakurai, Solute clustering, segregation and microstructure in high strength low alloy Al-Cu-Mg alloys. *Materials Science & Engineering A*, 1998. A250: p. 120-126.
- 27 Hamana, D., M. Boucheur, M. Betrouche, A. Derafa, and N. Y. Rokhmanov, Comparative study of formation and transformation of transition phases in Al-12wt%Mg alloy. *Journal of Alloys and Compounds*, 2001. 320: p. 93-102.
- 28 Chen, S. P., M. S. Vossenbergh, F. J. Vermolen, J. Van de Langkruis, and S. Van de Zwaag, Dissolution of b particles in an Al Mg Si alloy during DSC runs. *Materials Science and Engineering*, 1999. A272: p. 250–256.
- 29 Zhen, L. and S. B. Kang, DSC analyses of the precipitation behavior of two Al-Mg-Si alloys naturally aged for different times. *Materials Letters*, 1998. 37(6): p. 349-353.
- 30 Hamana, D., M. Boucheur, and A. Derafa, Effect of plastic deformation on the formation and dissolution of transition phases in Al-12 wt.% Mg alloy. *Materials Chemistry and Physics*, 1998. 57: p. 99-110.
- 31 Gupta, A. K., D. J. Lloyd, and S. A. Court, Precipitation hardening in Al-Mg-Si alloys with and without excess Si. *Materials Science and Engineering A*, 2001. 316(1-2): p. 11-17.
- 32 Edwards, G. A., K. Stiller, G. L. Dunlop, and M. J. Couper, The precipitation sequence in Al-Mg-Si alloys. *Acta Materialia*, 1998. 46(11): p. 3893-3904.
- 33 Cayron, C. and P. A. Buffat, Transmission electron microscopy study of the [beta]' phase (Al-Mg-Si alloys) and QC phase (Al-Cu-Mg-Si alloys): ordering mechanism and crystallographic structure. *Acta Materialia*, 2000. 48(10): p. 2639-2653.
- 34 Polmear, I. J., *Light Alloys*. Third ed. *Metallurgy and Materials Science Series*, ed. R. Honeycombe and P. Hancock. 1995, London: Arnold. 362.
- 35 Suresh, S., *Fatigue of Materials*. Second ed. 2001: Cambridge University Press. 679.
- 36 Blanc, C., B. Lavelle, and G. Mankowski, The role of precipitates enriched with copper on the susceptibility to pitting corrosion of the 2024 aluminium alloy. *Corrosion Science*, 1997. 39(3): p. 495-510.



37. Guillaumin, V. and G. Mankowski, Localized corrosion of 2024 T351 aluminium alloy in chloride media. *Corrosion Science*, 1999. 41: p. 421-438.
38. Liao, C.-M., J. M. Olive, M. Gao, and R. P. Wei, In-situ monitoring of pitting corrosion in aluminum alloy 2024. *Corrosion*, 1998. 54(6): p. 451-458.
39. ASM, *Corrosion of Aluminum and Aluminum Alloys*, ed. J.R. Davis. 1999.
40. Tanguy, D., B. Bayle, R. Dif, and T. Magnin, Hydrogen effects during IGSCC of pure Al-5Mg alloy in NaCl media. *Corrosion Science*, 2002. 44: p. 1163-1175.
41. Delafosse, D. and T. Magnin, Hydrogen induced plasticity in stress corrosion cracking of engineering systems. *Eng. Fract. Mech*, 2001. 68: p. 693-729.
42. Braun, R., Comparison of accelerated SCC tests performed on the aluminium alloy 2014-T651. *Werkstoffe und Korrosion*, 1992. 43: p. 453-458.
43. Braun, R., Investigation of the SCC Behaviour of alloy 2024 using the slow strain rate technique. *Werkstoffe und Korrosion*, 1993. 44: p. 73-82.
44. Braun, R., Slow strain rate testing of high-strength aluminium alloy plate in an aqueous solution of 3% NaCl +0.3% H<sub>2</sub> O<sub>2</sub>. *Werkstoffe und Korrosion*, 1994. 45: p. 369-377.
45. Braun, R. *Stress corrosion cracking behaviour of Al-Li Aluminium alloys in Aluminium Alloys- Their physical and mechanical properties*. 1994. Atlanta.
46. Braun, R., Slow strain rate testing of aluminum alloy 7050 in different tempers using various synthetic environments. *Corrosion*, 1997. 53(6): p. 467-474.
47. Braun, R., Exfoliation corrosion testing of aluminium alloys. *British Corrosion Journal*, 1995. 30(3).
48. Braun, R. *Exfoliation corrosion and stress corrosion cracking behaviour of Al-Li alloys*. 1994. Seville, Spain.
49. ASTM G34-90, in *Annual Book of ASTM Standards*, ASTM, Editor. 1994. p. 129.
50. Revie, R. W., V. S. Sastri, G. R. Hoey, R. R. Ramsingh, D. K. Mak, and M. T. Shehata, Hydrogen-induced cracking of linepipe steels Part 1-threshold hydrogen concentration and pH. *Corrosion*, 1993. 49(1): p. 17-23.
51. Chu, W. Y., C. H. Huang, Y. B. Wang, and L. J. Qiao, Hydrogen embrittlement of rail steels. *Corrosion*, 1999. 55(9): p. 892-897.
52. Symons, D. M., The effect of hydrogen on the fracture toughness of alloy X-750 at elevated temperatures. *Journal of Nuclear Materials*, 1999. 265: p. 225-231.
53. Cantwell, J. E., High-Temperature hydrogen attack. *Materials Performance*, 1994: p. 58-61.
54. Nakamura, M. and K. W. Gao, Hydrogen embrittlement of Ti-49Al at various strain rates. *Intermetallics*, 2002. 10: p. 233-238.
55. Al-Anezi, M. A., G. S. Frankel, and A. K. Agrawal, Susceptibility of conventional pressure vessel steel to hydrogen-induced cracking and stress oriented hydrogen-induced cracking in hydrogen sulfide-containing diglycolamine solutions. *Corrosion*, 1999. 55(11): p. 1101-1109.
56. Sofronis, P. and I. M. Robertson, Atomistic scale experimental observations and micromechanical/continuum models for the effect of hydrogen on the mechanical behavior of metals. 2001.
57. Robertson, I. M., The effect of hydrogen on dislocation dynamics. *Eng. Fract. Mech*, 2001. 68: p. 671-692.
58. Sofronis, P., I. M. Robertson, Y. Liang, D. F. Teter, and N. Aravas, *Recent Advances in the study of hydrogen embrittlement at the University of Illinois*. 2001.
59. Luu, W. C. and J. K. Wu, Hydrogen transport and environmental embrittlement effects in iron aluminides. *Journal of Materials Science*, 2000. 35: p. 4121-4127.

60. Luu, W. C., H. S. Kuo, and J. K. Wu, Hydrogen permeation through nickel-plated steels. *Corrosion Science*, 1997. 39(6): p. 1051-1059.
61. Young, G. A. and J. R. Scully, Evidence that carbide precipitation produces hydrogen traps in Ni-17Cr-8Fe alloys. *Scripta Materialia*, 1997. 36(6): p. 713-719.
62. Au, M. U., A visible technology for display of hydrogen distribution in metals. *Journal of Alloys and Compounds*, 1999. 293-295: p. 317-323.
63. Pressouyre, G. M., A classification of hydrogen traps in steel. *Materials transactions A*, 1979. 10A: p. 1571-1573.
64. Pressouyre, G. M., Trap theory of hydrogen embrittlement. *Acta Metallurgica*, 1979. 28: p. 895-911.
65. Lee, S.-M. and J.-Y. Lee, The trapping and transport phenomena of hydrogen in nickel. *Metallurgical Transactions A*, 1986. 17A: p. 181-187.
66. Pound, B. G., The effect of ageing on hydrogen trapping in precipitation- hardened alloys. *Corrosion Science*, 2000. 42: p. 1941-1956.
67. Thomas, R. L. S., D. Li, R. P. Gangloff, and J. R. Scully, Trap-governed hydrogen diffusivity and uptake capacity in ultrahigh-strength AERMET 100 steel. *Metallurgical and Materials Transactions A*, 2002. 33A: p. 1991-2004.
68. Enos, D. G. and J. R. Scully, A critical-strain criterion for hydrogen embrittlement of cold-drawn, ultrafine pearlitic steel. *Metallurgical and Materials Transactions A*, 2002. 33A: p. 1151-1165.
69. Katano, G., H. Ueyama, and M. Mori, Observation of hydrogen distribution in high-strength steel. *Journal of Materials Science*, 2001. 36: p. 2277-2286.
70. Eliaz, N., A. Shachar, B. Tal, and D. Eliezer, Characteristics of hydrogen embrittlement, stress corrosion cracking and tempered martensite embrittlement in high-strength steels. *Engineering Failure Analysis*, 2002. 9: p. 167-184.
71. Marrow, T. J., M. Aindow, P. Prangnell, M. Strangwood, and J. F. Knott, Hydrogen-assisted stable crack growth in iron-3wt% silicon steel. *Acta Materialia*, 1996. 44(8): p. 3125-3140.
72. Chiang, W. C., Hydrogen susceptibility of 17-4 Ph stainless steel. *Materials Letters*, 2002(4186): p. 1-4.
73. ASM, ed. *Corrosion*. Ninth ed. ASM Handbook, ed. A.I.H. Committee. Vol. 13. 1987: USA.
74. Nagumo, M., H. Uyama, and M. U. Yoshizawa, Accelerated failure in high strength steel by alternating hydrogen-charging potential. *Scripta Materialia*, 2001. 44(6): p. 947-952.
75. McMahan Jr., C. J., Hydrogen -induced intergranular fracture of steels. *Eng. Fract. Mech*, 2001. 68: p. 773-788.
76. Birnbaum, H. K., C. Buckley, F. Zeides, E. Sirois, P. Rozenak, S. Spooner, and J. S. Lin, Hydrogen in aluminum. *Journal of Alloys and Compounds*, 1997. 253-254: p. 260-264.
77. Christodoulou, L. and H. M. Flower, Hydrogen embrittlement and trapping in Al-6%-Zn-3%-Mg. *Acta Metallurgica*, 1980. 28: p. 481-487.
78. Pantelakis, S. G., A. T. Kermanidis, P. G. Daglaras, and C. A. Apostolopoulos, The Effect of Existing Corrosion on the Structural Integrity of Aging Aircraft. *The Effect of Existing Corrosion on the Structural Integrity of Aging Aircraft in Fatigue in the Presence of Corrosion*. 1998. Corfu, Greece: AGARD Workshop.
79. Scamans, G. M., R. Alani, and P. R. Swann, Pre-exposure embrittlement and stress failure in Al-Zn-Mg alloys. *Corrosion Science*, 1976. 16: p. 443-459.

80. Scamans, G. M. and C. D. S. Tuck. Embrittlement of aluminium alloys exposed to water vapour in Environment- sensitive fracture of engineering materials. 1979. New York, NY: Metallurgical Society AIME.
81. Speidel, M. O., Hydrogen embrittlement and stress corrosion cracking of aluminum alloys. 1974.
82. Itoh, G., K. Koyama, and M. Kanno, Evidence for the transport of impurity hydrogen with gliding dislocation in aluminum. *Scripta Materialia*, 1996. 35(6): p. 695-698.
83. Saitoh, H., Y. Iijima, and K. Hirano, Behaviour of hydrogen in pure aluminium Al-4 mass% Cu and Al-1 mass% Mg<sub>2</sub>Si alloys studied by tritium electron microautoradiography. *Journal of Materials Science*, 1994. 29: p. 5739-5744.
84. Young, G. A. and J. R. Scully, The diffusion and trapping of hydrogen in high purity aluminium. *Acta Materialia*, 1998. 46(18): p. 6337-6349.
85. Tuck, C. D. S. Evidence for the formation of magnesium hydride on the grain boundaries of Al-Mg and Al-Zn-Mg alloys during their exposure to water vapour in On the effects of hydrogen on the behaviour of materials. 1980. Wyoming.
86. Song, R. G., M. K. Tseng, B. J. Zhang, J. Liu, Z. H. Jin, and K. S. Shin, Grain boundary segregation and hydrogen-induced fracture in 7050 aluminium alloy. *Acta mater.*, 1995. 44(8): p. 3241-3248.
87. Jang, W., S. Kim, and K. Shin, Hydrogen-assisted deformation and fracture behaviors of Al 8090. *Metallurgical and Materials Transactions A*, 2002. 33A: p. 1755-1763.
88. Jang, W. and S. Kim, Hydrogen-assisted fracture of Al 8090. *Journal of Materials Science Letters*, 2000. 19: p. 447-450.
89. Haidemenopoulos, G. N., N. Hassiotis, G. Papapolymerou, and V. Bontozoglou, Hydrogen absorption into aluminium alloy 2024-T3 during exfoliation and alternate immersion testing. *Corrosion*, 1998. 54(1): p. 73-78.
90. EPETII/30, Damage tolerance behavior of corroded aluminum structures. 1999, General Secretariat for Research and Technology: Greece.
91. Scherer, J., O. M. Mangnussen, T. Ebel, and R. J. Behm, Initial stages of the anodic etching of aluminium foils studied by atomic force microscopy. *Corrosion Science*, 1999. 41: p. 35-55.
92. ASTM E8M-94a, in *Annual Book of ASTM Standards*, ASTM, Editor. 1994: West Conshohoken, PA. p. 129.
93. Charitidou, E., G. Papapolymerou, G. N. Haidemenopoulos, N. Hasiotis, and V. Bontozoglou, Characterization of trapped hydrogen in exfoliation corroded aluminium alloy 2024. *Scripta Materialia*, 1999. 41(12): p. 1327-1332.
94. Sundman, B., B. Jansson, and J. O. Anderson, *Calphad*, 1985(9): p. 153.
95. Sofronis, P., Y. Liang, and N. Aravas, Hydrogen induced shear localization of the plastic flow in metals and alloys. *European Journal of Mechanics - A/Solids*, 2001. 20(6): p. 857-872.
96. Liang, Y., P. Sofronis, and J. Dodds, R.H., Interaction of hydrogen with crack-tip plasticity: effects of constrain on void growth. 2004.
97. Pantelakis, S. G., P. V. Petroyiannis, H. Kamoutsi, G. N. Haidemenopoulos, and V. Bontozoglou. Evidence on the corrosion-induced hydrogen embrittlement of the 2024 aluminum alloy in International conference on influence of traditional mathematics and mechanics on modern science and technology. 2004. Messini, Greece.
98. Petroyiannis, P. V., Department of Mechanical Engineering and Aeronautics. In progress, University of Patras, Greece.

# Curriculum Vitae

## Helen M. Kamoutsi

### Personal Information

- Date of Birth 29 March, 1974
- Nationality Hellenic/EU
- Marital Status Single

### Academic Education

1992–1998

**University of Thessaly, Dept. Of Mechanical & Industrial Engineering, Volos, Greece**

Dipl Mechanical Engineer

Graduation Thesis “Application Systems of Color Metallography”

1999–Present

**University of Thessaly, Dept. Of Mechanical & Industrial Engineering, Volos, Greece**

Candidate for Phd in Mechanical Engineering

Subject of Doctoral Thesis “Corrosion-induced Hydrogen Embrittlement in High-Strength Al-Alloys”

### Professional Activities

10/1999 – Present

**University of Thessaly, Dept. Of Mechanical & Industrial Engineering, Volos, Greece**

### Involved in the research activities listed below:

- **ECSC 7210-PR-161: "Optimization of Microstructure in Multi-Phase Steels containing Retained Austenite"** In collaboration with RWTH-Aachen, SOLAC, Thyssen-Krupp Stahl
- **ECSC 7210-PR-370: "Control and Exploitation of the Bake-Hardening Effect in Multi-Phase High-Strength Steels"** In collaboration with RWTH-Aachen, University Ghent, Thyssen-Krupp Stahl, Voest-Alpine Stahl, ARCELOR
- **P.E.N.E.D. 99ED649 "Corrosion and Hydrogen Embrittlement of Aircraft Aluminum Alloys".** In collaboration with the University of Patras.
- **Airbus: "Evaluation of Hydrogen Embrittlement on Aluminum Alloy 2024".** In collaboration with the University of Patras.
- **EPEAEK program: "Postgraduate Study Programme in the Department of Mechanical & Industrial Engineering in the University of Thessaly".**

### Scholarships

1992

And

10/2001 – Present

Financial Support (Scholarship) from the National Scholarship Foundation (IKY)

### Publications

- H Kamoutsi, G Kakoudakis, M Vlachogiannis, D Orphanidis, G Haidemenopoulos and V Bontozoglou "Characterization of hydrogen trapped during corrosion of aluminum alloy 2024, 3<sup>rd</sup> PanHellenic Scientific

- Conference of Chemical Mechanics. 2001. Athens, Greece.
- H. Kamoutsi and G. Haidemenopoulos "Characterization of hydrogen trapped during corrosion of aircraft aluminum alloys. 1<sup>st</sup> PanHellenic Conference on Metallic Materials. 2001. Volos, Greece.
  - H. Kamoutsi, A. Katsamas, A. Avgelis, G. Haidemenopoulos and V. Bontozoglou "Characterization of natural corrosion of aluminium alloy 2024 with Atomic Force Microscopy (AFM), 3<sup>rd</sup> PanHellenic Scientific Conference of Chemical Mechanics. 2001. Athens, Greece.
  - Kamoutsi H., Haidemenopoulos G. and Bontozoglou V. "Hydrogen Uptake During Exfoliation Corrosion of Al-alloys: The Extent of Hydrogen Affected Zone:, 11<sup>th</sup> International Conference on Computational & Experimental Engineering and Sciences of ICES. 2003. Corfu, Greece.
  - Pantelakis, S. G., P. V. Petroyiannis, H. Kamoutsi, G. N. Haidemenopoulos, and V. Bontozoglou. Evidence on the corrosion-induced hydrogen embrittlement of the 2024 aluminum alloy, to be presented in International conference on influence of traditional mathematics and mechanics on modern science and technology. 2004. Messini, Greece.
  - H. Kamoutsi, G. N. Haidemenopoulos, V. Bontozoglou and S .Pantelakis. Corrosion –induced hydrogen embrittlement in aluminium alloy 2024, to be presented in 11<sup>th</sup> International conference on fracture. 2005. Turin, Italy.
  - P.V. Petroyiannis, E. Kamoutsi, Sp.G. Pantelakis, V. Bontozoglou and G.N. Haidemenopoulos, " Evidence on the corrosion-induced hydrogen embrittlement of the 2024 aluminum alloy ", submission for publication in journal of Fatigue & Fracture of Engineering Materials & Structures.

